THEORETICAL METHODS FOR NON-RELATIVISTIC QUANTUM AND CLASSICAL SCATTERING PROCESSES

by

Akilesh Venkatesh

A Dissertation

Submitted to the Faculty of Purdue University

In Partial Fulfillment of the Requirements for the degree of

Doctor of Philosophy

Department of Physics and Astronomy

West Lafayette, Indiana

December 2022

THE PURDUE UNIVERSITY GRADUATE SCHOOL
STATEMENT OF COMMITTEE APPROVAL

Dr. Francis Robicheaux, Chair

Department of Physics and Astronomy

Dr. Chris Greene

Department of Physics and Astronomy

Dr. Niranjan Shivaram

Department of Physics and Astronomy

Dr. Rafael Lang

Department of Physics and Astronomy

Approved by:

Dr. Gabor Csathy

To my parents who encouraged me to pursue physics despite how far it took me from home.

ACKNOWLEDGMENTS

I am extremely grateful to my advisor Prof. Francis Robicheaux for his patient mentoring and enormous persistent encouragement. His attention to detail and the value of his feedback cannot be overstated.

I would like to thank Prof. Chris Greene for nurturing interesting discussions during our many lunch meetings. He always helped me see and fill gaps in my understanding.

I am grateful to Prof. Niranjan Shivaram for discussions on x-ray scattering and the experimental challenges involved. He was always generous to me with his time and wisdom whenever I knocked at his office door.

Further, I would like to thank Prof. Rafael Lang for taking the time to serve on my committee and guide my doctoral studies. I thank my fellow graduate students over the years for their support especially those from Prof. Robicheaux's group and Prof. Greene's group. Finally, I am grateful to my friend and fellow graduate student Sachin Vaidya for our innumerable discussions on a multitude of physics and math topics.

The work on nonlinear Compton scattering was possible through fruitful discussions with D.A. Reis and P.H. Bucksbaum. This material is based upon work supported by the U.S. Department of Energy, Office of Science, Basic Energy Sciences, under Grant No. DE-SC0012193

TABLE OF CONTENTS

LIST OF FIGURES

ABSTRACT

This dissertation discusses the theoretical methods for quantum scattering in the context of x-ray scattering from electrons and classical scattering in the context of collisions between Rydberg atoms.

A method for describing non-relativistic x-ray scattering from bound electrons is presented. The approach described incorporates the full spatial dependence of the incident x-ray field and is non-perturbative in the incident x-ray field. The x-ray scattering probability obtained by numerical solution for the case of free-electrons is bench-marked with well known analytical free-electron results.

A recent investigation by Fuchs *et al.* [Nat. Phys. 11, 964 (2015)] revealed an anomalous frequency shift of at least 800 eV in non-linear Compton scattering of high-intensity x-rays by electrons in solid beryllium. The x-ray scattering approach described is used to explore the role of binding energy, band structure, electron-electron correlation and a semi-Compton channel in the frequency shift of scattered x-rays for different scattered angles. The results of the calculation do not exhibit an additional redshift for the scattered x-rays beyond the non-linear Compton shift predicted by the free-electron model.

The interference between Compton scattering and nonlinear Compton scattering from a two-color field in the x-ray regime is theoretically analyzed for bound electrons. A discussion of the underlying phase shifts and the dependence of the interference effect on the polarizations of the incident and outgoing fields are presented.

The problem of using x-ray scattering to image the dynamics of an electron in a bound system is examined. Previous work on imaging electronic wave-packet dynamics with x-ray scattering revealed that the scattering patterns deviate substantially from the notion of instantaneous momentum density of the wave packet. Here we show that the scattering patterns can provide clear insights into the electronic wave packet dynamics if the final state of the scattered electron and the scattered photon momentum are determined simultaneously. The scattering probability is shown to be proportional to the modulus square of the Fourier transform of the instantaneous electronic spatial wave function weighted by the final state of the electron.

Collisional ionization between Rydberg atoms is examined. The dependence of the ionization cross section on the magnitude and the direction of orbital angular momentum of the electrons and the direction of the Laplace-Runge-Lenz vector of the electrons is studied. The case of exchange ionization is examined and its dependence on the magnitude of angular momentum of the electrons is discussed.

1. INTRODUCTION

The chapters are based on work that has been published. This chapter is designed to give a brief overview of the problems discussed in this thesis. Chapter 2 contains a discussion of some of the essential concepts implicitly used in the following chapters. The chapters 3, 4, 5 and 6 are self-contained with sections of introduction and conclusion. In Chapter 7, a summary is presented.

1.1 X-ray scattering

X-rays, since their discovery in 1895, have played an important role in the development of modern quantum theory of matter and radiation. Lawrence Bragg's investigation (1913) of x-ray diffraction from solids [1] led to the discovery of crystal structure and revealed that x-rays are a useful probe at the atomic scale. This was followed by the discovery of Compton scattering (1923) using x-rays by Arthur Compton [2] which for the first time clearly demonstrated the quantum nature of light. The low interaction cross section of x-rays with matter means that as x-rays travel through a sample, the likelihood of rescattering after the first scattering event is minimal. This makes them an excellent probe. Their short wavelength which is comparable to the size of the atoms means that they can be valuable tools to study electronic structure. These properties have continued to make x-rays a source and probe of interesting physics. In general when x-rays interact with matter, a wide variety of x-ray scattering processes are possible including resonant x-ray scattering processes such as x-ray photo-ionization, resonant excitation, etc and non-resonant x-ray scattering processes such as Compton scattering, Bragg scattering, etc. This thesis primarily focuses on non-resonant x-ray scattering effects.

In Compton scattering, a single incoming photon inelastically scatters off an electron leading to one outgoing photon. The frequency of the scattered photon can be obtained by solving the equations of conservation of momentum and energy for the electron-photon interaction. The probability for an electron to Compton scatter a photon scales linearly with the intensity of the incoming electromagnetic field. Klein and Nishina [3] derived the angular dependence of the differential cross section; many advanced quantum mechanics textbooks [4]

give their analytic differential cross section. Over the years, the study of Compton scattering has yielded many applications. By examining the Compton scattered photon, it is possible to obtain the momentum distribution of the electron before the photon scattered off the electron. This is known as the Compton profile. Compton profiles can shed light into the nature of the electronic states [5, 6]. Compton profiles can also be used as an experimental check on the theoretically calculated wave function for the electron.

While the arrival of the laser in the 1960s made it possible to probe light-matter interaction at high intensities, the advent of x-ray free electron lasers (XFELs) has brought intensities of $\sim 10^{20}$ W/cm^2 within reach of experiments [7–10]. These ultrafast high intensity sources allow for the study of several nonlinear phenomenon such as high harmonic generation [11], multi-photon ionization [12], Breit-Wheeler processes [13], and nonlinear Compton scattering. The term nonlinear Compton scattering has been used to describe a variety of multi-photon processes [14, 15]. In this work, nonlinear Compton scattering refers to a process where two incoming photons inelastically scatter off an electron to give one outgoing photon. The scattering probability for nonlinear Compton scattering scales with the square of the incoming field intensity.

Nonlinear Compton scattering was first described for a free electron by Brown and Kibble [16] in 1964. They showed that, the scattered photon frequency for the non-relativistic case can be obtained from the Compton expression provided one replaces the frequency of the incoming photon with twice its value. Their derivation included shifts due to the intensity of the x-rays which arise due to ponderomotive energy shifts; the usual Compton shift only depends on the wavelength of the photon and has no intensity dependence because of a low-intensity approximation. They also derived an analytic expression for the differential cross section for a more general case of the nonlinear Compton scattering where n incoming photons scatter off a free electron leading to one outgoing photon. It should be noted that the differential cross section for Compton scattering which is given by the Klein-Nishina formula [3] has notable differences with the differential cross section derived by Brown and Kibble [16] for nonlinear Compton scattering. Nonlinear Compton scattering was first experimentally confirmed for the case of free electrons in 1996 [17].

Chapter 3 details a non-relativistic theoretical approach to x-ray nonlinear Compton scattering from bound electrons. A recent experiment [18] involving nonlinear Compton scattering from a bound electron revealed an anomalous frequency shift of at least 800 eV in the scattered photon frequency from a bound electron. The bound nature of the electron was hypothesized in Ref. [18] as a possible source for the anomalous frequency shift. While the results of Brown and Kibble [16] pertain to nonlinear Compton scattering from a free electron, this chapter analyzes different aspects of nonlinear Compton scattering from a bound electron. Before applying the method to bound electrons, the theoretical method described is benchmarked against the free electron results of Klein-Nishina for Compton scattering and Brown and Kibble for nonlinear Compton scattering. Then, the scattering profile and the differential cross section for a bound electron is calculated and their dependence on the binding energy of the bound electron is examined.

In Chapter 4, the toolkit developed in Chapter 3 is expanded to study interference between the scattered photons from nonlinear Compton and Compton scattering when a two-color field is used. The two colour field consists of an ω_{in} field and a $2\omega_{in}$ field with an external phase shift being imposed on the $2\omega_{in}$ field. For a given scattering angle, the Compton scattered photons from the $2\omega_{in}$ field are of the same frequency ($\sim 2\omega_{in}$) as the nonlinear Compton scattered photons from the ω_{in} field. These two processes can give rise to scattered photons with the same momentum and polarization, thus making interference possible. Two aspects of the interference are discussed in detail: first, the intrinsic phase difference between Compton scattered waves and nonlinear Compton scattered waves; second, the dependence of the interference on different cases of polarization of the incoming fields.

Let the intensities of the ω_{in} and the $2\omega_{in}$ fields be denoted by $I_{\omega_{in}}$ and $I_{2\omega_{in}}$ respectively. Within the perturbative limits (see Sec. 4.3.1), the Compton scattering signal scales $\propto I_{2\omega_{in}}$, the nonlinear Compton scattering signal scales $\propto I^2_{\omega_{in}}$, and the interference term scales $\propto I_{\omega_{in}} \sqrt{I_{2\omega_{in}}}$.

There are a couple of motivations to study this interference. Even with XFELs offering incoming fields of high intensities ($\sim 10^{20}$ W/cm^2), the nonlinear Compton scattering signal in experiments can still be quite small relative to the Compton scattering signal from the same incoming field. The calculations in Chapter 3, reveal that the nonlinear Compton signal

can be about six orders of magnitude less than the Compton signal for an incoming x-ray field of intensity $\sim 10^{20}$ W/cm^2 and incoming photon energy ~ 9.25 keV. This makes it difficult to study nonlinear Compton scattering experimentally. Using XFELs poses another challenge, the field provided by the XFEL does not strictly contain just the fundamental harmonic ω_{in} but also tends to have a small amount of the second harmonic ($2\omega_{in}$) associated with the field. The second harmonic noise from the XFEL ($2\omega_{in}$) can undergo Compton scattering and can interfere with the nonlinear Compton scattering signal from the fundamental (ω_{in}) of the XFEL.

The study of interference between Compton scattering from the $2\omega_{in}$ field and nonlinear Compton scattering from the ω_{in} field is thus not only relevant but can also provide some insight into addressing these challenges. By measuring the difference in intensity between the constructively and the destructively interfered scattered waves along with pure Compton scattering measurements, one can estimate the amount of nonlinear Compton scattering without having to measure the small signal directly. For example, if the nonlinear Compton scattering is six orders of magnitude smaller than the Compton scattering signal, then the interference term would be 3 orders of magnitude smaller than Compton scattering. When the noise from the second harmonic of XFEL is an issue, the study offers some insight to minimize or eliminate the interference from the second harmonic of the XFEL.

In Chapter 5, x-ray scattering is used to image the dynamics of an electronic wave packet. X-rays have been historically used to successfully image the momentum density of an electron in a stationary state [5]. For an electron in a stationary state, the spatial probability density does not vary with time. However for an electron that is in a superposition of states of different energies (a wave-packet state), the spatial probability density oscillates with time. Imaging the time-dependent dynamics of the electronic charge density in a system can provide valuable information about bond-formation, bond-breaking, etc and allow the construction of molecular movies [19–23]. This has widespread implications in helping understand chemical reaction mechanisms. It should be noted that to image the dynamics at the electronic time-scale which is typically of the order of femtoseconds, one needs a probe pulse whose pulse duration is smaller. The currently available XFELs can generate ultrafast pulses in this desired parameter range.

The problem of imaging the dynamics of an electronic wave packet using x-ray scattering has been examined for at least two decades. It was assumed that the time-dependent x-ray scattering pattern reflects the instantaneous momentum density of the electron. In a seminal work by Dixit et al. [24] in 2012, it was shown that the dependence of the x-ray scattering pattern on the instantaneous spatial electronic wave function was non-trivial. Since the probe pulse has a pulse duration that is shorter than the oscillation time-period of the electronic wave packet, Fourier reasons dictate that it have a larger energy bandwidth than the electronic wave packet. This can cause the x-ray pulse to drive transitions from the wave packet states to states energetically outside the wave packet. Therefore the scattering probability involves a summation over all possible final states. Dixit et al. showed that this summation over final states causes the x-ray scattering pattern to look substantially different from the modulus square of Fourier transform of the instantaneous charge density. This makes any meaningful interpretation of the x-ray scattering profile difficult. In Chapter 5, it is shown that if the final state(s) after the x-ray scattering from the wave-packet is known, then the differential scattering probability reflects the modulus square of transition charge density of the electronic wave packet. Two approaches are discussed for determining the final state(s) after scattering. First, the case of a direct coincidental measurement of the final state(s) along with the scattered photon momentum and polarization is presented. This approach while experimentally difficult can be used to understand the physics of the scattering profile. Then an alternative approach to coincidental measurement is presented. This involves using a precise measurement of the scattered photon energy to indirectly determine the final state(s) of the electron. This is possible because the scattered photon and the scattering electron are quantum mechanically entangled. The approach is illustrated through several simple examples using electronic wave packets in a hydrogen atom. However, it should be noted that the x-ray imaging approach presented in this work is quite general and not specific to an atom or molecule.

1.2 Rydberg-Rydberg scattering

A Rydberg atom is an atom with a valence electron in a highly excited state characterized by a large principal quantum number n. Rydberg atoms have long been a source of study for their interesting properties [25]. These properties include strong interaction with electric and magnetic fields, long range interaction between Rydberg atoms, and classical behavior of the valence electrons [26]. Given these properties, Rydberg atoms have recently even become a candidate as neutral qubits for quantum computing [27].

The size of Rydberg atoms scale $\propto n^2$, the time scales involving Rydberg states scale $\propto n^3$ and the average velocities of the valence electron in these states scale $\propto 1/n$. The large n of these electrons means that the states in the neighbourhood of n form a near continuum. A quantum treatment of Rydberg states in Rydberg-Rydberg interactions may require calculations on a very large Hilbert space and can be difficult. In particular, it should be noted that a quantum treatment of the problem discussed in Chapter 6 would require calculations on a Hilbert space that is beyond the presently available computing power. However, many problems involving Rydberg atoms including the one presented in Chapter 6 consist of classically allowed transformations and substantial averaging over final states and, therefore, a classical approach usually leads to accurate values for measurable quantities like ionization cross sections (see Sec. 6.2).

The highly excited nature of the valence electron in these atoms makes them susceptible to ionization due to either blackbody radiation [28] or Penning ionization as a result of collisions between them. Penning ionization refers to a process in which two highly excited atoms collide to yield an ion, an electron, and the other atom ending up with lower energy. If both the atoms are initially in a state with principal quantum number n for the valence electrons and there is no energy transferred to the electrons from the translational energy of the atoms, then it can be shown that the non-ionized atom should end up with a principal quantum number $n' < n/\sqrt{2}$.

Penning ionization can occur even when Rydberg atoms are at rest due to their strong interaction [29]. These interactions can be due to van der Waals forces, dipole-dipole interaction or other higher-order multipole moments depending on the distance of separation

and the nature of their electronic states [30]. The thermal energies of Rydberg atoms can also lead to collisional ionization [31]. Effectively, collisional ionizations can lead to loss of prepared Rydberg atoms and can be a cause for concern in experiments.

In Chapter 6, the collisional ionization between Rydberg atoms in relative motion is examined using a classical approach. The classical approach is justified because of reasons stated in Sec. 6.2 and the experimental evidence [31–34]. The dependence of the ionization cross section on the orientation of Rydberg atoms is examined. The angular momentum vector $\boldsymbol{L}$ and the Laplace-Runge-Lenz vector $\boldsymbol{A}$ are used to characterize the orientation of each Rydberg atom. The magnitude and the direction of the angular momentum and the direction of the Laplace-Runge-Lenz vector are varied in a systematic way for a few orientations to study their impact on the ionization cross section. Only symmetric collisions i.e. collisions in which both the colliding atoms have the same $\boldsymbol{L}$ and $\boldsymbol{A}$ are studied. This was done to resemble the experimental arrangement from a recent experiment on collisional ionization of Rydberg atoms [31]. The aim of this investigation is to understand the role of orientation in the collisional ionization and, if possible, to arrive at ways to minimize the collisional ionization.

2. SOME ESSENTIAL CONCEPTS

In this chapter, a brief discussion of some of the essential concepts that feature in the subsequent chapters is provided. Only those concepts which are not directly discussed in the other chapters are presented here. The sections presented here will not be explicitly referenced later.

2.1 Atomic units

In Atomic units (sometimes called Hartree atomic units), the fundamental constants in physics can be summarised as follows.

$$\hbar = \mathrm{e} = m_{\mathrm{e}} = 1;\ \epsilon_0 = \frac{1}{4\pi} \tag{2.1}$$

where $\hbar$, e, m_{e}, and ϵ_0 refer to reduced Planck constant, elementary charge, rest mass of the electron, and the permittivity of vacuum, respectively. Some other constants are summarized below,

$$a_0 = 1;\ c = \frac{1}{\alpha} \tag{2.2}$$

where a_0, α, and c refer to Bohr radius, fine structure constant, and the speed of light in vacuum respectively. To provide an idea of the atomic scale, approximately 1 a.u. of energy corresponds to 27.2 eV and 1 a.u. of time corresponds to 24.2 attoseconds.

2.2 Derivation of x-ray scattering probability amplitude

A description of x-ray scattering from bound electrons and the derivation of the scattering probability amplitude is contained in Chapter. 3. However, in this section, the derivation is presented with some additional detail. Some of this derivation has appeared in Ref. [35].

The total vector potential of the x-ray field $\hat{\boldsymbol{A}}$ is modeled by treating the incoming electromagnetic (EM) wave $\boldsymbol{A}_C$ classically and quantizing the scattered wave $\hat{\boldsymbol{A}}_Q$ [36]:

$$\hat{\boldsymbol{A}} = \boldsymbol{A}_C + \hat{\boldsymbol{A}}_Q. \tag{2.3}$$

This can be understood with the following reasoning: in the strong field x-ray regime examined in this work, there is an enormous amount of incident photons on a given atom (or molecule). This makes keeping track of the state of the incident photons less useful. Also if the incident field is an ideal laser field then the incident photons are in a coherent state. In the Fock basis, this means that there is a significant population in several Fock states. Therefore, it is reasonable to treat the incident field as a classical field. In an actual experiment, the x-ray pulse is provided by an XFEL. These XFEL pulses can have a lot of noise and exhibit high shot-to-shot variation. This experimental aspect provides another justification for treating the incident field classically. However, such a treatment is not reasonable for the outgoing x-ray as the scattering cross sections are extremely low which results in a tiny number of scattered photons. Also, the states of these scattered photons are entangled with the scattering electron which allows for experimental measurement. For instance in the case of Compton scattering from a free electron, the scattered photon momentum can be determined from the final momentum of the scattered electron given their initial momenta. Therefore, to capture the physics of the x-ray scattered photons, the scattered field has to be quantized.

The explicit space and time dependence of the incoming classical field $\boldsymbol{A_C}$ is given below,

$$\boldsymbol{A}_C = \frac{E}{\omega_{in}} \cos(\omega_{in} t - \boldsymbol{k_{in}} \cdot \boldsymbol{r}) \ \exp\left[\frac{-(2\ln 2)(t - \frac{\hat{\boldsymbol{k}}_{in}\cdot \boldsymbol{r}}{c})^2}{t_{wid}^2}\right] \boldsymbol{\epsilon_{in}}, \tag{2.4}$$

where the quantities E, ω_{in}, $\boldsymbol{k_{in}}$, t_{wid}, and $\boldsymbol{\epsilon_{in}}$ refer to the incoming electric field amplitude, angular frequency, momentum, the full width at half maximum (FWHM) of the pulse intensity, and polarization direction respectively. Note that the quantity $\hat{\boldsymbol{k}}_{in}$ refers to a unit vector in the direction of $\boldsymbol{k_{in}}$.

The quantized vector potential $\hat{\boldsymbol{A}}_Q$ is given by [36]

$$\hat{\boldsymbol{A}}_Q = \sqrt{\frac{2\pi}{V}} \sum_{\boldsymbol{k},\boldsymbol{\epsilon}} \frac{1}{\sqrt{\omega_k}} \left[\boldsymbol{\epsilon} \mathrm{e}^{\mathrm{i}\boldsymbol{k}\cdot\boldsymbol{r}} \hat{a}_{\boldsymbol{k},\boldsymbol{\epsilon}} + \boldsymbol{\epsilon}^* \mathrm{e}^{-\mathrm{i}\boldsymbol{k}\cdot\boldsymbol{r}} \hat{a}^\dagger_{\boldsymbol{k},\boldsymbol{\epsilon}}\right]. \tag{2.5}$$

The symbols $\boldsymbol{\epsilon}$ and $\boldsymbol{k}$ refer to the unit polarization vector and wave vector of the photon, respectively, with $\boldsymbol{k} \cdot \boldsymbol{\epsilon} = 0$. Here, $\omega_k = |\boldsymbol{k}|$ c. The operators $\hat{a}^\dagger_{\boldsymbol{k},\boldsymbol{\epsilon}}$ and $\hat{a}_{\boldsymbol{k},\boldsymbol{\epsilon}}$ can create or

annihilate a photon in mode $(\boldsymbol{k}, \boldsymbol{\epsilon})$, respectively. The V in the pre-factor refers to the volume of the region used to quantize the electromagnetic field modes. The quantity $\boldsymbol{r}$ is the position vector and c is the speed of light in vacuum, which is approximately 137.036 a.u. While the modes inside the sum [Eq. (2.5)] depend on the quantization volume V, the final results are independent of the quantization volume. The reason here is that a limit of an infinite volume is considered.

For the light-matter interaction, the Hamiltonian [37] is

$$\hat{H} = \frac{(\hat{\boldsymbol{P}} + \hat{\boldsymbol{A}})^2}{2} + V(\hat{\boldsymbol{x}}) + \sum_{\boldsymbol{k},\boldsymbol{\epsilon}} \omega_k \hat{a}^\dagger_{\boldsymbol{k},\boldsymbol{\epsilon}} \hat{a}_{\boldsymbol{k},\boldsymbol{\epsilon}}. \tag{2.6}$$

The wave function is expanded in the Fock basis based on the number of *scattered* photons. Therefore, our wave function ansatz is as follows,

$$|\psi_{total}\rangle = \psi^{(0)}(\boldsymbol{r}, t)\,|0\rangle + \sum_{\boldsymbol{k},\boldsymbol{\epsilon}} \psi^{(1)}_{\boldsymbol{k},\boldsymbol{\epsilon}}(\boldsymbol{r}, t) \mathrm{e}^{-\mathrm{i}\omega_k t} \hat{a}^\dagger_{\boldsymbol{k},\boldsymbol{\epsilon}}\,|0\rangle \tag{2.7}$$

where $|0\rangle$ refers to the vacuum state of the photon in Fock space. The ansatz is adequate because the first term describes an electron interacting with a classical EM field without any scattered photons. The wave function of this electron is given by $\psi^{(0)}(\boldsymbol{r}, t)$. The second term describes the presence of a scattered photon. The quantity $\psi^{(1)}_{\boldsymbol{k},\boldsymbol{\epsilon}}(\boldsymbol{r}, t)$ is the probability amplitude at time t, for a photon to scatter into momentum $\boldsymbol{k}$ and polarization $\boldsymbol{\epsilon}$ *and* the electron to be found at position $\boldsymbol{r}$.

Using Eqs. (2.3) and (2.6) the total Hamiltonian takes the form,

$$\hat{H} = \frac{(\hat{\boldsymbol{P}} + \boldsymbol{A_C})^2}{2} + (\hat{\boldsymbol{P}} + \boldsymbol{A}_C) \cdot \hat{\boldsymbol{A}}_Q + \frac{\hat{\boldsymbol{A}}^2_Q}{2} + V(\hat{\boldsymbol{x}}) + \sum_{\boldsymbol{k},\boldsymbol{\epsilon}} \omega_k \hat{a}^\dagger_{\boldsymbol{k},\boldsymbol{\epsilon}} \hat{a}_{\boldsymbol{k},\boldsymbol{\epsilon}}. \tag{2.8}$$

In the chapters that follow, we only retain the terms of first order in $\hat{\boldsymbol{A}}_Q$. At first glance, in the interested parameter regime we expect the quantity $\hat{\boldsymbol{A}}^2_Q$ to be smaller than $\hat{\boldsymbol{A}}_Q$. Upon inspection, it can be seen that the quantity $\hat{\boldsymbol{A}}^2_Q$ contains two kinds of terms which introduce two different types of processes. The terms such as $\hat{a}^\dagger_{\boldsymbol{k_1},\boldsymbol{\epsilon_1}} \hat{a}^\dagger_{\boldsymbol{k_2},\boldsymbol{\epsilon_2}}$ give rise to two scattered photons. Since in the following chapters we are concerned with x-ray scattering processes

that results in only one outgoing photon, neglecting these is justified. The terms such as $\hat{a}_{\boldsymbol{k_1},\epsilon_1}\hat{a}^{\dagger}_{\boldsymbol{k_2},\epsilon_2}$ give rise to the Lamb shift which diverges if renormalization is not taken into account which is beyond the scope of this thesis.

In the above Hamiltonian [Eq. (2.8)], we can separate out the terms with and without $\hat{\boldsymbol{A}}_Q$. The terms with $\hat{\boldsymbol{A}}_Q$ can be treated as a perturbative correction. The unperturbed Hamiltonian is

$$\hat{H}^{(0)} = \frac{(\hat{\boldsymbol{P}} + \boldsymbol{A}_C)^2}{2} + V(\hat{\boldsymbol{x}}) + \sum_{\boldsymbol{k},\boldsymbol{\epsilon}} \omega_k \hat{a}^{\dagger}_{\boldsymbol{k},\boldsymbol{\epsilon}} \hat{a}_{\boldsymbol{k},\boldsymbol{\epsilon}}. \tag{2.9}$$

The perturbation term is

$$\hat{H}^{(1)} = (\hat{\boldsymbol{P}} + \boldsymbol{A}_C) \cdot \hat{\boldsymbol{A}}_Q. \tag{2.10}$$

Given the total Hamiltonian $(\hat{H}^{(0)} + \hat{H}^{(1)})$ and the wave function ansatz [Eq. (2.7)], the time-dependent Schrödinger equation for the x-ray scattering problem is

$$\mathrm{i}\frac{\partial \left|\psi_{total}\right\rangle}{\partial t} = (\hat{H}^{(0)} + \hat{H}^{(1)}) \left|\psi_{total}\right\rangle. \tag{2.11}$$

The left hand side is

$$\mathrm{i}\frac{\partial \left|\psi_{total}\right\rangle}{\partial t} = \mathrm{i}\frac{\partial \psi^{(0)}}{\partial t}\left|0\right\rangle + \mathrm{i}\sum_{\boldsymbol{k},\boldsymbol{\epsilon}} \frac{\partial \psi^{(1)}_{\boldsymbol{k},\boldsymbol{\epsilon}}(\boldsymbol{r},t)}{\partial t} \mathrm{e}^{-\mathrm{i}\omega_k t}\left|1_{\boldsymbol{k},\boldsymbol{\epsilon}}\right\rangle + \sum_{\boldsymbol{k},\boldsymbol{\epsilon}} \psi^{(1)}_{\boldsymbol{k},\boldsymbol{\epsilon}}(\boldsymbol{r},t)\omega_k \mathrm{e}^{-\mathrm{i}\omega_k t}\left|1_{\boldsymbol{k},\boldsymbol{\epsilon}}\right\rangle. \tag{2.12}$$

The right-hand side is

$$\begin{aligned}
\hat{H}\left|\psi_{total}\right\rangle =& (\hat{H}^{(0)} + \hat{H}^{(1)})\Big[\psi^{(0)}\left|0\right\rangle + \sum_{\boldsymbol{k},\boldsymbol{\epsilon}} \psi^{(1)}_{\boldsymbol{k},\boldsymbol{\epsilon}} \mathrm{e}^{-\mathrm{i}\omega_k t}\hat{a}^{\dagger}_{\boldsymbol{k},\boldsymbol{\epsilon}}\left|0\right\rangle\Big] \\
=& \hat{H}^{(0)}\psi^{(0)}\left|0\right\rangle + \sum_{\boldsymbol{k},\boldsymbol{\epsilon}} \left[\frac{(\hat{\boldsymbol{P}} + \boldsymbol{A}_C)^2}{2} + V(\boldsymbol{r}) + \omega_k\right] \psi^{(1)}_{\boldsymbol{k},\boldsymbol{\epsilon}} \mathrm{e}^{-\mathrm{i}\omega_k t}\left|1_{\boldsymbol{k},\boldsymbol{\epsilon}}\right\rangle \\
&+ (\hat{\boldsymbol{P}} + \boldsymbol{A}_C) \cdot \sqrt{\frac{2\pi}{V}} \sum_{\boldsymbol{k},\boldsymbol{\epsilon}} \frac{1}{\sqrt{\omega_k}} \boldsymbol{\epsilon}^* \mathrm{e}^{-\mathrm{i}\boldsymbol{k}\cdot\boldsymbol{r}} \psi^{(0)}\left|1_{\boldsymbol{k},\boldsymbol{\epsilon}}\right\rangle.
\end{aligned} \tag{2.13}$$

Note that only first order terms in the scattered field is retained in the above perturbative expansion. Equating the two sides [Eqs. (2.12) and (2.13)] and comparing the terms that correspond to the same Fock state. For no scattered photons,

$$\mathrm{i}\frac{\partial\psi^{(0)}}{\partial t} - \hat{H}_C\psi^{(0)} = 0 \tag{2.14}$$

where

$$\hat{H}_C = \hat{H}^{(0)} - \sum_{\boldsymbol{k},\boldsymbol{\epsilon}} \omega_k \hat{a}^\dagger_{\boldsymbol{k},\boldsymbol{\epsilon}} \hat{a}_{\boldsymbol{k},\boldsymbol{\epsilon}}. \tag{2.15}$$

Note that the appearance of $\hat{H}_C$ in Eq. (2.14) is consistent with the our initial definition of $\psi^{(0)}$. Remember that $\psi^{(0)}$ is defined as the wave function of an electron interacting with a classical EM field. For 1 scattered photon we get,

$$\begin{aligned}\mathrm{i}\frac{\partial\psi^{(1)}_{\boldsymbol{k},\boldsymbol{\epsilon}}}{\partial t} - \hat{H}_C\psi^{(1)}_{\boldsymbol{k},\boldsymbol{\epsilon}} =& \sqrt{\frac{2\pi}{V\omega_k}}\mathrm{e}^{-\mathrm{i}\boldsymbol{k}\cdot\boldsymbol{r}}\mathrm{e}^{\mathrm{i}\omega_k t} \\ & \times \boldsymbol{\epsilon}^*\cdot(\hat{\boldsymbol{P}} + \boldsymbol{A}_C)W(t)\psi^{(0)}\end{aligned} \tag{2.16}$$

where

$$W(t) = \mathrm{e}^{-(\frac{t}{\tau})^8} \tag{2.17}$$

is a windowing function, introduced as a numerical device to speed convergence by restricting the range of times for which the wave function needs to be solved. Note that the choice of τ in Eq. (2.17) is determined by the duration of the pulse. The x-ray scattering probability amplitude can be obtained by solving the two-coupled differential equations [Eqs. (2.14) and (2.16)].

The windowing function, $W(t)$, assumes a value of 1 when the pulse is turned on and is zero when the pulse is turned off. A windowing function is required in Eq. (2.16) for several reasons. First, it is used to turn on the in-homogeneous term in Eq. (2.16) only for the duration of the incident laser pulse. In the absence of a windowing function, the $\hat{\boldsymbol{P}}\psi^{(0)}$ source term gives rise to non-zero scattering probability amplitudes even when there is no incident pulse. This results in unphysical scattering cross sections. Introducing a windowing function that adiabatically turns on the source terms solves this problem and also helps in calculating

the ground state of the electron-photon coupled system. The windowing function needs to be smooth to avoid encountering the Gibbs phenomenon [38]. Given these conditions for the windowing function, the results for the scattering probability amplitude are independent of the choice of the windowing function. Note that this is only true if Eq. (2.16) is used to obtain the scattering probability amplitudes after the pulse is turned off. For intermediate times when the incident pulse is active, Eq. (2.16) can give scattering probability amplitudes which may depend on the choice of windowing function.

2.3 Second-order central difference and its effects

Since the numerical calculations are carried out in a grid of points, the effect of grid-spacing needs to be carefully understood. Consider a free-electron, its Hamiltonian in position space is given by

$$\hat{H} = -\frac{1}{2}\nabla^2. \tag{2.18}$$

For example, for a one-dimensional grid, the Hamiltonian can be approximated by a finite-difference scheme. Here a second-order central difference scheme is used as it preserves the Hermiticity of the Hamiltonian. The grid points are described by positions x_1,x_2,... x_N and the grid-spacing is Δx. Then,

$$\hat{H}\psi_{\mathrm{j}} = -\frac{1}{2}\frac{\left[\psi_{\mathrm{j}+1} - 2\psi_{\mathrm{j}} + \psi_{\mathrm{j}-1}\right]}{\Delta x^2}. \tag{2.19}$$

Because of the finite grid, there exists a maximum energy for the electron. The maximum energy of an electron in this grid can be calculated by assuming a plane wave solution $\psi = A\mathrm{e}^{\mathrm{i}kx}$ with some normalization constant A in the finite grid.

$$\begin{aligned}\hat{H}\psi_{\mathrm{j}} &= -\frac{A}{2}\frac{\left[\mathrm{e}^{\mathrm{i}k(x_{\mathrm{j}}+\Delta x)} - 2\mathrm{e}^{\mathrm{i}kx_{\mathrm{j}}} + \mathrm{e}^{\mathrm{i}k(x_{\mathrm{j}}-\Delta x)}\right]}{\Delta x^2} \\ &= -\frac{A}{2\Delta x^2}\mathrm{e}^{\mathrm{i}kx_{\mathrm{j}}}\Big[2\ (\cos k\Delta x - 1)\Big].\end{aligned} \tag{2.20}$$

Using the time-independent Schrödinger equation,

$$E = \frac{1}{2}\left(\frac{2}{\Delta x^2}\right)\Big[(1-\cos k\Delta x)\Big]. \tag{2.21}$$

The maximum energy is achieved when $k\Delta x = \pi$. This corresponds to the case when there exists a maximum difference in the wave function amplitude between points x and $x+\Delta x$. This occurs when the wave function changes sign between the two grid points. Hence, the maximum energy E_{max} possible for the grid is

$$E_{max} = \frac{2}{\Delta x^2}\ . \tag{2.22}$$

The error dependence from the central difference on the grid spacing can be understood by Taylor expansion in Eq. (2.21),

$$\begin{aligned} E &= \frac{1}{2}\left(\frac{2}{\Delta x^2}\right)\left[(1-\left(1-\frac{k^2\Delta x^2}{2!}+\frac{k^4\Delta x^4}{4!}-\ ...\right)\right] \\ &= \frac{k^2}{2}\left[1+2\left(-\frac{k^2\Delta x^2}{4!}+\frac{k^4\Delta x^4}{6!}\right)\right]. \end{aligned} \tag{2.23}$$

The energy of the free electron in a grid deviates quadratically with the grid-spacing from the analytical free electron expression in the lowest order approximation. Therefore, the grid spacing should be chosen such that $k\Delta x \ll 1$. Note that this is much lower than the k that corresponds to the maximum energy in the grid E_{max}. In order for the grid to describe a physically realistic electron, $k\Delta x \ll 1$. For the calculations in this thesis, the grid-spacing is chosen such that this condition is satisfied. It is worth mentioning here that for Compton and nonlinear Compton scattering scenarios discussed in this thesis, k imparted to the electron is small compared to say photoionization. This implies that for studying Compton and nonlinear Compton scattering one does not need as small a grid-spacing (Δx) as that which is needed for studying photoionization.

2.4 Overview of leap-frog method

The leap-frog method is used to solve the time-dependent Schrödinger equation (TDSE) in Chapters 3, 4, and 5. In this section, a brief overview of the leap-frog method is provided. Let the initial state be described by $|\psi(0)\rangle$. Given the state at time t, the leap frog method involves using the time-derivative at time $t + \Delta t$ to calculate the state at $|\psi(t + 2\Delta t)\rangle$.

$$|\psi(t + 2\Delta t)\rangle = |\psi(t)\rangle + 2\Delta t\, |\dot{\psi}(t + \Delta t)\rangle \tag{2.24}$$

where

$$|\dot{\psi}(t)\rangle = -\mathrm{i}\hat{H}\, |\psi(t)\rangle\,. \tag{2.25}$$

The slope at mid-time is required by leap-frog to propagate the state. However, the initial condition only provides the state at the initial time $t = 0$. To resolve this issue, first Euler method is used with half the time-step. That is,

$$|\psi\big(\frac{\Delta t}{2}\big)\rangle = |\psi(0)\rangle + \frac{\Delta t}{2}\, |\dot{\psi}(0)\rangle\,. \tag{2.26}$$

Then leap-frog is used to obtain $|\psi(\Delta t)\rangle$.

$$|\psi(\Delta t)\rangle = |\psi(0)\rangle + \Delta t\, |\dot{\psi}\big(\frac{\Delta t}{2}\big)\rangle\,. \tag{2.27}$$

Now that the state is known at times t and $t + \Delta t$, leap-frog can be used to obtain the wave function at all time-steps up to some desired final time t_{final}. Note that instead of Eqs. (2.26) and (2.27), one could directly use the second-order Runge-Kutta method to obtain $|\psi(\Delta t)\rangle$. Both approaches result in identical final expressions for $|\psi(\Delta t)\rangle$.

For the unitarity of the state vector to be preserved during the propagation of the TDSE using leap-frog, the time-step should satisfy $\Delta t E_{max} < 1$. Here E_{max} is the maximum energy of the energy eigenstates that constitute the state $|\psi(t)\rangle$. The local truncation error in a leap-frog step scales with Δt^3. Therefore, error can accumulate during propagation with each time-step. For a given t_{final}, the global truncation error can be estimated by multiplying the local truncation error with the total number of time-steps involved. Hence,

the global truncation error scales with Δt^2. The time-step error is usually quite small because $\Delta t < 1/E_{max}$ and the E_{max} is usually much larger than the energy scale (E_{scale}) of the wave function. Thus, the global truncation error is usually of the order $(E_{scale}/E_{max})^2$. For example, in the calculations in Sec. 3.3.2, the expected maximum energy for a nonlinear Compton scattered photoelectron would be roughly 74 a.u. (2 keV). For the chosen 3D grid of grid-spacing 0.07 a.u., $E_{max} \sim 1225$ a.u. Therefore the size of the error would be $(74/1225)^2 \sim 3.6 \times 10^{-3}$

2.5 Richardson extrapolation

In numerical calculations, the accuracy of an evaluated quantity is often constrained by the grid-spacing of the numerical grid and it may be computationally difficult to do the same calculations in a finer grid. In these scenarios, Richardson extrapolation can offer a remedy. Richardson extrapolation is a powerful technique which allows one to improve the accuracy of a numerically obtained quantity over what was directly possible given a grid-spacing, provided the quantity is numerically convergent with grid-spacing. This technique is illustrated below with an example.

Let p be a quantity that is evaluated numerically from a grid. Let p scale quadratically with the grid spacing Δx. For a grid with a step-size Δx, p takes the following form:

$$p(\Delta x) = p_0 + C_1 \Delta x^2 + O(\Delta x^4). \tag{2.28}$$

Here C_1 is some constant and p_0 is the true value of p, that is

$$p_0 = \lim_{\Delta x \to 0} p(\Delta x). \tag{2.29}$$

If one evaluates p in a numerical grid of spacing $\Delta x/2$, then

$$p\left(\frac{\Delta x}{2}\right) = p_0 + \frac{C_1}{4}\Delta x^2 + O(\Delta x^4). \tag{2.30}$$

The two simultaneous equations Eqs. (2.28) and (2.30) can be used to estimate p_0 in the lowest order approximation,

$$\frac{1}{3}\left[4\, p\left(\frac{\Delta x}{2}\right) - p(\Delta x)\right] = p_0 + O(\Delta x^4). \tag{2.31}$$

An important observation here is that the above estimate for p_0 is better than $p(\Delta x)$ or $p(\Delta x/2)$. The method can also be used to eliminate the error from higher order terms. For example, one can solve three simultaneous equations obtained from three different grid-spacings instead of the two used here [Eqs. (2.28) and (2.30)]. This helps eliminate the error in p_0 from terms of order Δx^4. In this way, the method allows one to obtain significantly more accurate results than a direct numerical calculation from a computationally feasible grid.

2.6 Calculating non-dipole matrix elements

In Chapter 5, while calculating the weighted Fourier transform of the instantaneous spatial wave function [Eq. (5.13)], one needs to calculate matrix elements of the form $\langle\psi_{n'l'm'}|\, \mathrm{e}^{-\mathrm{i}\boldsymbol{Q}\cdot\boldsymbol{r}}\, |\psi_{nlm}\rangle$. In the x-ray regime, a dipole approximation of the plane wave does not fully capture the x-ray scattering. A full multipole expansion of the exponent is

$$\mathrm{e}^{-\mathrm{i}\boldsymbol{Q}\cdot\boldsymbol{r}} = 4\boldsymbol{\pi}\sum_{l_2=0}^{\infty}\sum_{m_2=-l_2}^{m_2=l_2}(-\mathrm{i})^{l_2}\mathrm{j}_{l_2}(Qr)Y_{l_2}^{m_2*}(\theta_Q,\Phi_Q)Y_{l_2}^{m_2}(\theta,\Phi). \tag{2.32}$$

Here θ_Q and Φ_Q are the polar and azimuthal angles respectively subtended by $\boldsymbol{Q}$ and similarly θ and Φ are the angles subtended by $\boldsymbol{r}$. The matrix element calculated in position space is given by

$$\begin{aligned}\int \psi^*_{n'l'm'}(\boldsymbol{r})\ \mathrm{e}^{-\mathrm{i}\boldsymbol{Q}\cdot\boldsymbol{r}}\psi_{nlm}(\boldsymbol{r})d^3r = 4\boldsymbol{\pi}\int R^*_{n'l'}Y_{l'}^{m'*}\sum_{l_2=0}^{\infty}\sum_{m_2=-l_2}^{m_2=l_2}(-\mathrm{i})^{l_2}\mathrm{j}_{l_2}(Qr)Y_{l_2}^{m_2*}(\theta_Q,\Phi_Q)\\ \times Y_{l_2}^{m_2}R_{nl}Y_l^m r^2 dr d\Omega.\end{aligned} \tag{2.33}$$

Using the properties of spherical harmonics and using the result,

$$\int Y_{l_1}^{m_1} Y_{l_2}^{m_2} Y_{l_3}^{m_3} d\Omega = \sqrt{\frac{(2l_1+1)(2l_2+1)(2l_3+1)}{4\pi}} \times \begin{pmatrix} l_1 & l_2 & l_3 \\ 0 & 0 & 0 \end{pmatrix} \begin{pmatrix} l_1 & l_2 & l_3 \\ m_1 & m_2 & m_3 \end{pmatrix}, \tag{2.34}$$

one can integrate Eq. (2.33) to obtain,

$$\begin{aligned} \int \psi^*_{n'l'm'}(\boldsymbol{r})\ \mathrm{e}^{-\mathrm{i}\boldsymbol{Q}\cdot\boldsymbol{r}} \psi_{nlm}(\boldsymbol{r}) d^3r = & \sum_{l_2=0}^{\infty} \sum_{m_2=-l_2}^{m_2=l_2} (-\mathrm{i})^{l_2} (-1)^{m'} \sqrt{4\pi(2l'+1)(2l_2+1)(2l+1)} \\ & \times Y_{l_2}^{m_2 *}(\theta_Q, \Phi_Q) \begin{pmatrix} l' & l_2 & l \\ 0 & 0 & 0 \end{pmatrix} \begin{pmatrix} l' & l_2 & l \\ -m' & m_2 & m \end{pmatrix} \\ & \times \int r^2 R_{n'l'}(r)\ \mathrm{j}_{l_2}(Qr) R_{nl}(r) dr. \end{aligned} \tag{2.35}$$

Note that quantities of the form $\begin{pmatrix} l' & l_2 & l \\ 0 & 0 & 0 \end{pmatrix}$ refer to 3j symbols. For the calculations in Chapter 5, the radial integral in Eq. (2.35) is evaluated numerically using a radial grid of points.

2.7 Classical trajectory Monte-Carlo approach

Here, some of the additional details that went into the Monte-Carlo approach in Chapter 6 is presented. The Monte-Carlo approach employed in Chapter 6 involves randomization of the initial conditions using a pseudo-random number generator. For the pseudo-random number generator, an implementation of Mersenne Twister engine in C++ is used. For every successful run, there are only two possible outcomes, either ionization exists or it does not. This results in a binomial distribution of outcomes. The number of ionization events recorded in the simulation corresponds to the average in this binomial distribution. If the

number of ionizations recorded is N_{i} and the total number of Monte-Carlo runs is N. Then probability of ionization,

$$p = \frac{N_{\mathrm{i}}}{N}. \tag{2.36}$$

The standard deviation for the binomial distribution is

$$\sigma_N = \sqrt{Np\ (1-p)}. \tag{2.37}$$

This standard deviation serves as a metric of the error in the number of ionization events recorded in the simulation. The standard deviation in the probability of ionization is given by

$$\sigma = \sqrt{\frac{p\ (1-p)}{N}}. \tag{2.38}$$

It should be noted here that the error in the ionization probability and the error in the ionization cross section scales with $1/\sqrt{N}$.

3. NONLINEAR COMPTON SCATTERING FROM BOUND ELECTRONS

The contents of this chapter were published as Venkatesh, A., & Robicheaux, F. (2020). Simulation of nonlinear Compton scattering from bound electrons. Physical Review A, **101**, 013409. The calculations included in Sec. 3.3.5 were performed after the publication of the work.

3.1 Introduction

Since, the discovery of Compton scattering 90 years ago, various measurements have been carried out to confirm the results to a higher accuracy and to probe the finer details of the Compton spectrum [39, 40]. This has given rise to the study of Compton profiles which provide extensive information about the momentum distribution of the electrons involved in the scattering [5, 6]. Compton profiles have also proven useful as an experimental check on the accuracy of the ground state wave function of electrons in momentum space obtained through theoretical methods. A number of applications in areas from material science to astrophysics have been born out of these studies [41, 42].

In this paper, non-linear Compton scattering refers to the process where two incoming photons interact with an electron leading to one outgoing photon. Non-linear Compton scattering was first described by Brown and Kibble [16] in 1964 where they developed an analytical QED framework to model the non-linear scattering [43] of photons by a free electron. In their work, they showed that when non-linear Compton scattering occurs, for the non-relativistic case, the frequency of the scattered photon can be obtained by the usual Compton expression, provided, one replaces the incoming frequency by twice that value. Including relativistic effects in the calculation gives rise to ponderomotive forces on the electron. At extremely high intensities (electric field >10000 a.u. for x-rays), the ponderomotive effects lead to the electron behaving as if it had a smaller mass and thus producing a bigger redshift for the scattered photons. It was more than two decades before experiments could study non-linear x-ray-matter interactions, but the arrival of x-ray free-electron lasers [7, 8] has made considerable progress [9, 10] possible.

More recently, Fuchs *et al.* [18] carried out an experiment to investigate non-linear x-ray matter interactions with the Linac Coherent Light Source at the SLAC National Accelerator Laboratory. They used a high-intensity x-ray free-electron laser to study non-linear scattering from solid beryllium. While non-linear Compton scattering had been earlier observed [17], Fuchs *et al.* [18] found a non-linear Compton signal that was substantially redshifted from the value predicted by Brown and Kibble [16]. To explain this additional redshift(∼800 eV), they proposed that the bound nature of the beryllium electrons could be responsible. This argument was analyzed by Krebs *et al.* [44]. They solved the time-dependent Schrödinger equation (TDSE) to simulate the non-linear x-ray scattering, with the bound electrons being modeled by a potential based on the Hartree-Fock-Slater model. Their calculations did not reveal any anomalies with respect to the free-electron results.

In this paper, we re-examine the additional frequency shift in Fuchs *et al.* [18]. We use a numerical approach different from that of Ref. [44] and study the effect of binding energy, electron-electron correlation, and photo-ionization on the non-linear Compton spectrum. We were able to obtain convergent results for both the differential cross section and the average scattered photon momentum for both linear Compton and non-linear Compton scattering. While we mainly agree with the results of Krebs *et al.* [44], our calculations reveal a small blue-shift in the frequency of the scattered photon with respect to the free-electron results. Following this, we explore two possible alternate causes for the redshift. First, we consider the role of electron-electron correlation effects on the scattering profile. Second, we examine the possibility of a semi-Compton process to give rise to the anomalous redshift.

For free-electrons, we performed calculations where the electron part of the wave function was restricted to 2D but for most of the bound electron calculations, the electron was fully 3D. For a given number of dimensions, the calculations for a bound electron involves less time and space computationally than its free-electron counterpart. It should be noted that a 2D model is quite adequate to describe both linear and non-linear Compton scattering but the exact factors required to calculate the differential cross length is not well defined. The 3D simulations lead to results with no adjustable parameters.

The model's validity is demonstrated by reproducing the differential cross length of x-ray scattering from a free-electron from a QED-2+1 scheme, which is a 2D analog of the Klein-

Nishina formula [3, 45]. Another way the validity of the model is tested is by comparing it with the non-linear Compton differential cross section of Brown and Kibble [16] for small binding energy. Finally the model is applied to the x-ray scattering scenario in Fuchs *et al.* [18] to study both the Compton and non-linear Compton scattering from a bound electron. In our calculations, we consider a range of binding energies for the bound electron from 0.4 a.u. to 6 a.u. This range of binding energies is relevant for Be because, the atomic Be has an ionization potential of 0.34 a.u. and that of Be^{2+} is 5.6 a.u.

Unless otherwise stated, atomic units will be used throughout this paper.

3.2 Methods and modeling

The first step in our approach is to model the initial state of the electron. For the free-electron case, we use a Gaussian wave-packet as the initial state. Recently, Pan and Gover [46] while analyzing spontaneous and stimulated emissions found that the size of the initial wave packet has non-trivial effects on the spectrum of the outgoing photons. These effects appear when the outgoing photons are in a coherent state and not a Fock state. However for the scattering problem under consideration, the size of the Gaussian wave packet is not significant.

For the bound electron case, we treat the electron as an atomic single electron and model the rest of the atom with an effective time-independent, local potential. We solve the time-independent Schrödinger equation to obtain the ground-state spatial wave function. For this, we use the relaxation method, propagating the Schrödinger equation in imaginary time until only the ground state remains. The ground-state wave function, thus obtained, was the initial state of the bound electrons in our calculations.

With the appropriate initial wave function, we can compute the time-dependent wave function for the electron in a classical field by numerically solving the TDSE. To model the scattered photon, we employ lowest order perturbation theory and solve for the case of a single outgoing photon. We obtain the scattering probability for different angles, which is used to calculate the differential cross section as a function of angle.

The non-relativistic treatment of the electron implied by the TDSE should be accurate enough for the conditions below. Consider the case of non-linear Compton scattering of a photon of $w = 340$ a.u. from a free electron. Even for the case of back scattering, the electron would at most gain approximately 1.2 keV of energy from the photon [Eq. (3.22)]. From the experiment by Fuchs *et al.* [18], we expect an additional kinetic energy gain of approximately 1 keV. Together, that would still give a Lorentz factor(γ) of only 1.004 which is well within the non-relativistic regime. As a check on the approximation, we consider the lowest order relativistic correction to the Schrödinger equation in Sec. 3.2.2 and demonstrate that it hardly changes the overall results.

3.2.1 Deriving the non-homogeneous Schrödinger equation

We model the vector potential by treating the incoming electromagnetic (EM) wave classically and quantizing the scattered wave [36]:

$$\hat{\boldsymbol{A}} = \boldsymbol{A}_C + \hat{\boldsymbol{A}}_Q. \tag{3.1}$$

Here, $\hat{\boldsymbol{A}}$ is the total vector potential. The quantities $\boldsymbol{A}_C$ and $\hat{\boldsymbol{A}}_Q$ refer to the classical vector potential and the quantized vector potential respectively. The quantized vector potential is given by [36],

$$\hat{\boldsymbol{A}}_Q = \sqrt{\frac{2\pi}{V}} \sum_{\boldsymbol{k},\boldsymbol{\epsilon}} \frac{1}{\sqrt{\omega_k}} \left[\boldsymbol{\epsilon} \mathrm{e}^{\mathrm{i}\boldsymbol{k}\cdot\boldsymbol{r}} \hat{a}_{\boldsymbol{k},\boldsymbol{\epsilon}} + \boldsymbol{\epsilon}^* \mathrm{e}^{-\mathrm{i}\boldsymbol{k}\cdot\boldsymbol{r}} \hat{a}^\dagger_{\boldsymbol{k},\boldsymbol{\epsilon}} \right] \tag{3.2}$$

The symbols $\boldsymbol{\epsilon}$ and $\boldsymbol{k}$ refer to the unit polarization vector and wave vector of the photon, respectively, with $\boldsymbol{k} \cdot \boldsymbol{\epsilon} = 0$. Here, $\omega_k = |\boldsymbol{k}|$ c. The operators $\hat{a}^\dagger_{\boldsymbol{k},\boldsymbol{\epsilon}}$ and $\hat{a}_{\boldsymbol{k},\boldsymbol{\epsilon}}$ can create or annihilate a photon in mode $(\boldsymbol{k}, \boldsymbol{\epsilon})$, respectively. The V in the pre-factor refers to the volume of the region used to quantize the electromagnetic field modes. The quantity $\boldsymbol{r}$ is the position vector and c is the speed of light in vacuum, which is approximately 137.036 a.u. It is to be noted that the final results are independent of the quantization volume V, because we consider the limit of an infinite volume.

The classical vector potential is modeled as a laser pulse with linear polarization. We choose the coordinate system such that the electric field only has a y-component and the x-ray pulse propagates in the x-direction. Our choice for this is given by the vector potential,

$$\boldsymbol{A}_C = \frac{E_C}{\omega_{in}} \cos\left[\omega_{in}(t - \frac{x}{c})\right] \exp\left[\frac{(-2\ln 2(t - \frac{x}{c})^2)}{t_{wid}^2}\right] \hat{y} \tag{3.3}$$

Here E_C and ω_{in}, refer to the amplitude and the angular frequency of the incoming electric field respectively and t_{wid} indicates the full width at half maximum (FWHM) of the pulse intensity. It is to be noted that $\boldsymbol{A}_C$ is a function of x and t only.

For the light-matter interaction, the Hamiltonian [37] is,

$$\hat{H} = \frac{(\hat{\boldsymbol{P}} + \hat{\boldsymbol{A}})^2}{2} + V(\hat{\boldsymbol{x}}) + \sum_{\boldsymbol{k},\boldsymbol{\epsilon}} \omega_k \hat{a}^\dagger_{\boldsymbol{k},\boldsymbol{\epsilon}} \hat{a}_{\boldsymbol{k},\boldsymbol{\epsilon}} \tag{3.4}$$

Note that the exact form of the potential energy $V(\hat{\boldsymbol{x}})$ is discussed in Sec. 3.3. We use Eqs. (3.1), (3.2) and (3.4) and separate out the terms with and without $\hat{\boldsymbol{A}}_Q$. The terms with $\hat{\boldsymbol{A}}_Q$ are part of the perturbative correction. In this paper, we retain only the terms of first order in $\hat{\boldsymbol{A}}_Q$. One reason for this is that the higher order terms, give rise to two scattered photons and the Lamb shift, both of which are beyond the scope of this paper. Thus, our unperturbed Hamiltonian is,

$$\hat{H}^{(0)} = \frac{(\hat{\boldsymbol{P}} + \boldsymbol{A}_C)^2}{2} + V(\hat{\boldsymbol{x}}) + \sum_{\boldsymbol{k},\boldsymbol{\epsilon}} \omega_k \hat{a}^\dagger_{\boldsymbol{k},\boldsymbol{\epsilon}} \hat{a}_{\boldsymbol{k},\boldsymbol{\epsilon}} \tag{3.5}$$

The perturbation term is,

$$\hat{H}^{(1)} = (\hat{\boldsymbol{P}} + \boldsymbol{A}_C) \cdot \hat{\boldsymbol{A}}_Q \tag{3.6}$$

The wave function is expanded in the Fock basis based on the number of scattered photons. Therefore our wave function ansatz is as follows,

$$|\psi_{total}\rangle = \psi^{(0)}(\boldsymbol{r}, t)\,|0\rangle + \sum_{\boldsymbol{k},\boldsymbol{\epsilon}} \psi^{(1)}_{\boldsymbol{k},\boldsymbol{\epsilon}}(\boldsymbol{r}, t) \mathrm{e}^{-\mathrm{i}\omega_k t} \hat{a}^\dagger_{\boldsymbol{k},\boldsymbol{\epsilon}}\,|0\rangle \tag{3.7}$$

where $|0\rangle$ refers to the vacuum state of the photon in Fock space. The ansatz is adequate because the first term describes an electron interacting with a classical EM field without any scattered photons. The wave function of this electron is given by $\psi^{(0)}(\boldsymbol{r}, t)$. The second term describes the presence of a scattered photon. The quantity $\psi^{(1)}_{\boldsymbol{k},\boldsymbol{\epsilon}}(\boldsymbol{r}, t)$ is the probability amplitude at time t, for a photon to scatter into momentum $\boldsymbol{k}$ and polarization $\boldsymbol{\epsilon}$ and the electron to be found at position $\boldsymbol{r}$.

Given the Hamiltonian and the wave function ansatz, we proceed with the TDSE retaining only the terms up to first order in perturbation and separating out the equations based on the number of scattered photons. For no scattered photons,

$$\mathrm{i}\frac{\partial\psi^{(0)}}{\partial t} - \hat{H}_C\psi^{(0)} = 0 \tag{3.8}$$

where,

$$\hat{H}_C = \hat{H}^{(0)} - \sum_{\boldsymbol{k},\boldsymbol{\epsilon}} \omega_k \hat{a}^\dagger_{\boldsymbol{k},\boldsymbol{\epsilon}} \hat{a}_{\boldsymbol{k},\boldsymbol{\epsilon}} \tag{3.9}$$

Note that $\hat{H}_C$ appears in Eq. (3.8) because $\psi^{(0)}$ is defined as the wave function of an electron interacting with a classical EM field. For 1 scattered photon we get,

$$\begin{aligned}\mathrm{i}\frac{\partial\psi^{(1)}_{\boldsymbol{k},\boldsymbol{\epsilon}}}{\partial t} - \hat{H}_C\psi^{(1)}_{\boldsymbol{k},\boldsymbol{\epsilon}} =& \sqrt{\frac{2\pi}{V\omega_k}}\mathrm{e}^{-\mathrm{i}\boldsymbol{k}\cdot\boldsymbol{r}}\mathrm{e}^{\mathrm{i}\omega_k t} \\ &\times \boldsymbol{\epsilon}^* \cdot (\hat{\boldsymbol{P}} + \boldsymbol{A}_C) W(t)\psi^{(0)}\end{aligned} \tag{3.10}$$

where,

$$W(t) = \mathrm{e}^{-(\frac{t}{\tau})^8} \tag{3.11}$$

The windowing function, W(t), adiabatically turns on the in-homogeneous term in Eq. (3.10) only for the duration of the incident laser pulse, t_{wid}. This is done to find the ground state of the electron-photon coupled system. This also prevents the unphysical emission of photons, that would occur if the interaction between the electron and quantized photons was instantaneously turned on. Note that the function should be smooth to avoid encountering the Gibbs phenomenon [38]. The choice of τ is determined by the duration of the pulse. The results of the calculation do not depend on τ as long as $\tau > 3.2\ t_{wid}$ approximately.

Another competing consideration is that, τ should be as small as possible to ensure that we only need to solve the TDSE for a short duration. In our calculations we chose $\tau \sim 3.2\ t_{wid}$. The results do not depend on the specific choice of the windowing function as long as it is a smooth function which attains a value of 1, only during the duration of the incoming pulse.

A modification of the procedure developed in this subsection is considered in Sec. 3.3.3 where the results of a two-electron calculation are discussed to probe electron-electron correlation effects in 2D.

3.2.2 Relativistic correction - $(\boldsymbol{P}+\boldsymbol{A})^4$ terms

Here, we demonstrate how a relativistic correction may be implemented. We do this by considering the next higher order term in mechanical momentum and re-deriving the expressions in Eqs. (3.8) and (3.10). A careful consideration of the non-commuting terms in $(\hat{\boldsymbol{P}}+\hat{\boldsymbol{A}})^4$ is required to derive the new equations. For no scattered photons,

$$\mathrm{i}\frac{\partial\psi^{(0)}}{\partial t} - \hat{H}_C\psi^{(0)} = -\frac{1}{8c^2}(\hat{\boldsymbol{P}}+\boldsymbol{A}_C)^4\psi^{(0)} \tag{3.12}$$

For 1 scattered photon,

$$\begin{aligned}\mathrm{i}\frac{\partial\psi^{(1)}_{\boldsymbol{k},\boldsymbol{\epsilon}}}{\partial t} - \hat{H}_C\psi^{(1)}_{\boldsymbol{k},\boldsymbol{\epsilon}} = &-\frac{1}{8c^2}(\hat{\boldsymbol{P}}+\boldsymbol{A}_C)^4\psi^{(1)}_{\boldsymbol{k},\boldsymbol{\epsilon}} \\ &+\sqrt{\frac{2\pi}{V\omega_k}}\boldsymbol{\epsilon}^*\cdot\Big[\mathrm{e}^{-\mathrm{i}\boldsymbol{k}\cdot\boldsymbol{r}}\mathrm{e}^{\mathrm{i}\omega_k t}(\hat{\boldsymbol{P}}+\boldsymbol{A}_C) \\ &-\frac{1}{2c^2}\mathrm{e}^{\mathrm{i}\omega_k t}\hat{\boldsymbol{G}}\Big]\psi^{(0)}\end{aligned} \tag{3.13}$$

where,

$$\begin{aligned}\hat{\boldsymbol{G}} = &\Big[\mathrm{e}^{-\mathrm{i}\boldsymbol{k}\cdot\boldsymbol{r}}(\hat{\boldsymbol{P}}+\boldsymbol{A}_C)^3\Big] \\ &+\Big[(\hat{\boldsymbol{P}}+\boldsymbol{A}_C)^3\mathrm{e}^{-\mathrm{i}\boldsymbol{k}\cdot\boldsymbol{r}}\Big] \\ &+\Big[(\hat{\boldsymbol{P}}+\boldsymbol{A}_C)^2\mathrm{e}^{-\mathrm{i}\boldsymbol{k}\cdot\boldsymbol{r}}(\hat{\boldsymbol{P}}+\boldsymbol{A}_C)\Big] \\ &+\Big[(\hat{\boldsymbol{P}}+\boldsymbol{A}_C)\mathrm{e}^{-\mathrm{i}\boldsymbol{k}\cdot\boldsymbol{r}}(\hat{\boldsymbol{P}}+\boldsymbol{A}_C)^2\Big]\end{aligned} \tag{3.14}$$

The above equations are a simple way in which relativistic corrections can be implemented. An alternative, more sophisticated approach would be to use the relativistic Schrödinger equation [47]. However, there is no need for such an approach given the results in Sec. 3.3.1. If the fields were a few orders of magnitude higher, there would be a need for a more sophisticated treatment of relativistic corrections [48].

3.2.3 Differential cross section

The probability for a photon to scatter with momentum $\boldsymbol{k}$ and polarization $\boldsymbol{\epsilon}$ is

$$P_{\boldsymbol{k},\boldsymbol{\epsilon}} = \int_v \psi^{(1)*}_{\boldsymbol{k},\boldsymbol{\epsilon}} \psi^{(1)}_{\boldsymbol{k},\boldsymbol{\epsilon}} d^n r \tag{3.15}$$

Here $d^n r$ refers to the volume element in n dimensions.

The method described in Sec. 3.2.1 automatically leads to a spread in the scattered photon momentum because the incoming field is not strictly monochromatic but rather a pulse. The amount of the spread in scattered photon momentum is determined by the width of the chosen laser pulse. Since there is a momentum spread in the scattered x-ray, the differential cross section for a given scattering angle is a summation over all possible magnitudes of scattered photon momentum. The total 1-photon cross section in 3D is given by,

$$\sigma^{(1)} = \sum_{\boldsymbol{k},\boldsymbol{\epsilon}} \frac{P_{\boldsymbol{k},\boldsymbol{\epsilon}}}{(\text{number of photons/area})} \tag{3.16}$$

where [36] ,

$$\sum_{\boldsymbol{k}} \longrightarrow \frac{V}{(2\pi)^3} \int d^3k \tag{3.17}$$

and,

$$\frac{\text{number of photons}}{\text{area}} = \frac{\int I dt}{\omega_{in}} \tag{3.18}$$

Here I refers to the intensity of the incoming field. It is to be noted that the incoming pulse is assumed to be quasi-monochromatic. This leads to the definition of the differential cross section:

$$\frac{\mathrm{d}\sigma}{\mathrm{d}\Omega}^{(1)} = \frac{V\omega_{\text{in}}}{(2\pi)^3}\frac{\int \sum_{\boldsymbol{\epsilon}} P_{\boldsymbol{k},\boldsymbol{\epsilon}} k^2 dk}{\int I dt} \tag{3.19}$$

Here V is the quantization volume. There exists a factor of $1/V$ in $P_{\boldsymbol{k},\boldsymbol{\epsilon}}$ which cancels out the V in the numerator. Note that ω_{in} refers to the angular frequency of the incoming electric field [Eq. (3.3)].

The 2-photon cross section in 3D has been defined in multiple ways [49, 50]. Here we define it so that the SI units would be $m^2/(W/m^2)$.

$$\sigma^{(2)} = \omega_{\text{in}} \frac{\sum\limits_{\boldsymbol{k},\boldsymbol{\epsilon}} P_{\boldsymbol{k},\boldsymbol{\epsilon}}}{\int I^2 dt} \tag{3.20}$$

Therefore the differential cross section would be,

$$\frac{\mathrm{d}\sigma}{\mathrm{d}\Omega}^{(2)} = \frac{V\omega_{\text{in}}}{(2\pi)^3}\frac{\int \sum_{\boldsymbol{\epsilon}} P_{\boldsymbol{k},\boldsymbol{\epsilon}} k^2 dk}{\int I^2 dt} \tag{3.21}$$

In both the 1-photon and 2-photon differential cross-sections, we calculate these integrals with respect to k^2dk by doing a Gaussian fit for the plots of $P_{\boldsymbol{k},\boldsymbol{\epsilon}}$ vs k and then performing an integral of the Gaussian function. The differential cross sections obtained from the 3D calculations do not have any adjustable parameters.

The exact factors to obtain the differential cross length from the scattering probability in 2D are not well defined. Therefore, we obtain this factor by scaling our differential cross sections to get an overall fit with the analytical free electron results [16, 45].

3.2.4 Solving the TDSE

We solve the TDSE using a Cartesian co-ordinate system with the wave function represented on a grid of points. The values of the grid parameters are specified in Sec. 3.2.5. For the kinetic energy operator in the Hamiltonian, we use a three-point central difference formula. The TDSE for $\psi^{(0)}(\boldsymbol{r}, t)$ [Eq. (3.8)] is solved using the leap-frog method [51]. We

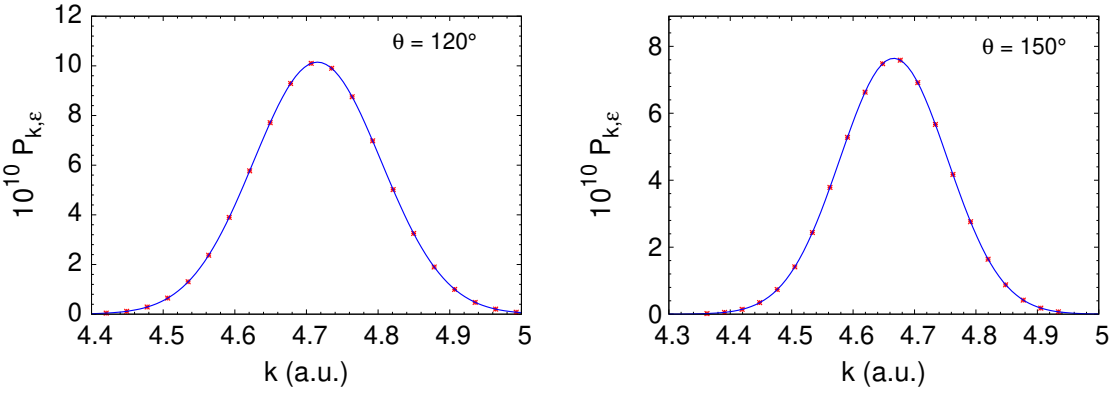

Figure 3.1. Scattering probability $P_{\boldsymbol{k},\boldsymbol{\epsilon}}$ as a function of scattered photon momentum k for non-linear Compton calculations in 2D for an angle of 120° and 150° respectively for a free-electron. The red points indicate the results of the numerical calculation and the blue line indicates a Gaussian fit. The calculations were performed over an equal number of k values on either side of the theoretical value. Note that the peaks are at the expected non-linear Compton momentum [Eq. (3.22)]. This calculations was done with E_C = 107 a.u. , ω_{in} = 340 a.u. and t_{wid} = 0.125 a.u.

choose the leap-frog method for two reasons: first, it preserves unitarity and second, it leads to converged results which is discussed in detail in Sec. 3.2.5. The leap-frog method involves computing the wave function which is two time-steps ahead of the current wave function, using the wave function at the current time-step and the wave function at the intermediate time. The second order Runge-Kutta method is used to obtain the value of the wave function at the first time-step which is required for the leap-frog approach. At every time instance, we simultaneously solve for $\psi^{(1)}_{\boldsymbol{k},\boldsymbol{\epsilon}}(\boldsymbol{r},t)$ for a range of scattered photon momenta centered around the Compton momentum or the Brown and Kibble prediction [Eq. (3.22)] for the linear Compton or non-linear Compton respectively. The plot of $P_{\boldsymbol{k},\boldsymbol{\epsilon}}$ [Eq. (3.15)] as a function of scattered photon momentum k is a Gaussian curve (see Fig. 3.1) to a good approximation.

In all our calculations unless otherwise stated, we use electric field $E_C = 107$ a.u. and angular frequency $\omega_{in} = 340$ a.u. for the incident laser pulse. In SI units, these values correspond to an electric field of $\sim$ 5 x 10^{13} V/m and an intensity of $\sim$ 3 x 10^{24} W/m^2. The chosen angular frequency corresponds to an incoming photon energy of about 9.25 keV. These values belong to the range used in the experiment by Fuchs *et al.* [18].

3.2.5 Grid and other numerical parameters

In our calculations, convergence is measured in two ways, by calculating the area under $P_{\boldsymbol{k},\boldsymbol{\epsilon}}$ vs k plots and by calculating the change in the peak position of the scattering probability. For all the calculations except in Sec. 3.3.3, the change in this area with respect to change in grid-spacing or grid-size was under 2%. The change in the peak position of scattering probability with respect to change in grid-spacing or grid-size was under 0.5% .

For the 2D free-electron calculations, a grid size of 400 X 400 with a grid-spacing of 0.1 a.u. in both x,y directions resulted in converged results. For the 3D calculations with Z=1, and 2 a grid range of 400 x 400 x 400 with a grid spacing of 0.1 a.u. resulted in converged results. For Z=4 a grid range of 229 X 229 X 229 with a grid-spacing of 0.07 units resulted in converged results.

The primary source of error in scattered photon momentum arises from the kinetic energy operator. The leading order error term is proportional to the square of the grid-spacing. For

the case of non-linear Compton scattering from a bound electron at an angle of 130° and for a grid-spacing of 0.07 a.u., the error is of the size of about 3% of the non-linear Compton shift. This error is much smaller than the size of the anomalous shift observed in Ref. [18] which is about 100% of the Compton shift. In Sec. 3.3.2, we take our estimate for scattered photon momentum, k below this 3% error by using Richardson's extrapolation to eliminate the leading order error term.

For t_{wid}, we use a range of 0.1 - 1 a.u. which corresponds to a pulse of duration $\sim 10^{-18}$s. The use of such a short pulse is justified because the results for the differential cross section are found to be independent of the choice of t_{wid}. A small change in peak scattered momentum is observed for different pulse widths. The magnitude of this change is less than about 1% of the momentum shift observed by Fuchs *et al.* [18]. Also, for the chosen range of t_{wid}, there is no reflection of the wave function from the walls, as the distance traveled by the wave packet of the electron is much smaller than the size of the grid.

3.3 Application

3.3.1 Free-electron case

We apply the method developed in Sec. 3.2, to a free electron interacting with a laser pulse in 2D and compare the results of our calculation with the equivalent of the Klein-Nishina formula in 2D [45]. Note that the Klein-Nishina formula and its analog in 2D are derived for monochromatic radiation. Since we employ a pulse, we evaluate the integral $D = \int \sum_{\boldsymbol{\epsilon}} P_{\boldsymbol{k},\boldsymbol{\epsilon}} k dk$ to find a quantity proportional to the differential cross length for a given intensity and incoming frequency. We compute this quantity D for different angles and compare this with the differential cross length from the QED-2+1 scheme [45] and the differential cross section from Brown and Kibble [16]. From this point in our discussions, we will refer to D as the differential cross length for convenience keeping in mind that the calculation has been scaled to match the analytical result.

We plot the differential cross length we obtained for linear Compton as a function of angle and the results from QED-2+1 [45] in Fig. 3.2. Upon comparison, we find that our calculated differential cross length agrees well with the free-electron analytical results.

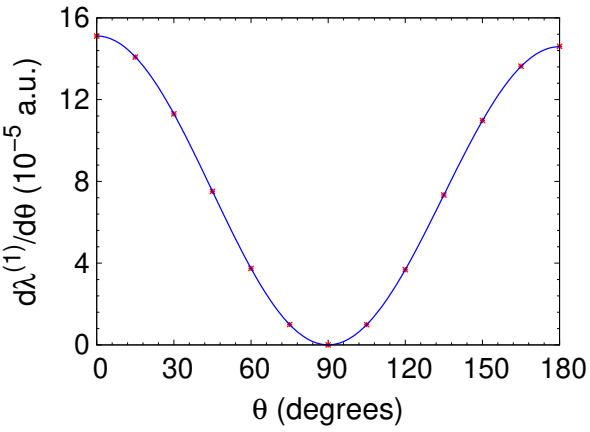

Figure 3.2. Comparison of differential cross length as a function of angle subtended by the detector with the analog of Klein-Nishina formula for 2D [45] for linear Compton scattering. The red points are the results of the numerical calculation and the blue line represents the results from the analytical expression [45]. The results of the numerical calculations in 2D were scaled by a single factor. This factor was chosen such that, overall, the numerical results fit well with the analytical results. The above calculations were done with the same parameters as Fig. 3.1.

Next, we compare the calculated 2D differential cross length (see Fig. 3.3) for non-linear Compton scattering with the analytical expression from Brown and Kibble [16]. We also evaluate the differential cross lengths using the relativistic corrections developed in Sec. 3.2.2 for comparison. The procedure for scaling the differential cross length used previously, is employed here as well. According to Brown and Kibble [16], for non-linear Compton scattering, the frequency of the scattered photon using a non-relativistic approximation is given by,

$$\omega = \frac{n\omega_{in}}{1 + n\alpha^2\omega_{in}(1 - cos\theta)} \tag{3.22}$$

Here, n determines the order of the process, for example $n = 1$ for Compton scattering. The discussions in this paper are restricted to processes where $n \leq 2$. The symbols ω and ω_{in} refers to the angular frequency of the scattered photon and incoming photon, respectively, and α is the fine-structure constant.

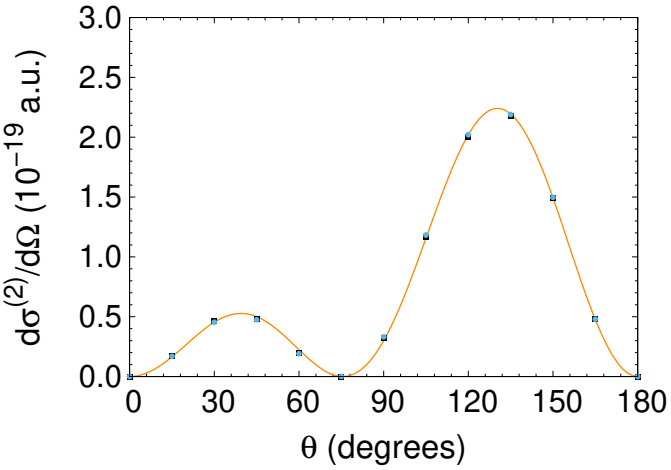

Figure 3.3. Comparison of differential cross sections(lengths) as a function of scattering angle in 2D with the results of Brown and Kibble for non-linear Compton scattering. The blue points indicate the non-relativistic results obtained using Eqs. (3.8) and (3.10). The black squares were obtained using the approach from Sec. 3.2.2. The orange line indicates the result from Brown and Kibble. The results of the numerical calculations in 2D were scaled by a single factor. This factor was chosen such that overall the numerical results fit well with the analytical results. The above calculations were done with the same parameters as Fig. 3.1.

It is important to note that the expression for the differential cross section by Brown and Kibble was derived in 3D, but our calculations are for the differential cross length in 2D. Upon comparison, we find that that our results are in good agreement with the Brown and Kibble results up to a constant factor. There is also no significant change (see Fig. 3.3) in the agreement with Brown and Kibble's result because of the relativistic correction discussed in Sec. 3.2.2. Brown and Kibble had arrived at their results by solving the Dirac equation but our agreement with their results justifies the approximation with the TDSE.

It was found that the scattering probability for non-linear Compton exhibits a second-order dependence on the intensity of the incoming EM field as expected and the scattering probability for Compton scattering exhibits a first-order dependence on the intensity of the incoming EM field. This behavior was observed over at least 3 orders of magnitude (up to 1000 a.u.) in the electric field.

3.3.2 Bound-electron case

Here we consider the case of bound electrons because of its relevance to Fuchs *et al.* [18]. Unlike the calculations for a free electron, here we adopt a 3D approach for the most part. It is to be noted that a 3D calculation can be done with relative ease for the case of a bound electron, as the grid needed for convergent solutions is smaller. Hence, it involves less memory and time computationally when compared to the case of a free electron.

While the method developed in Sec. 3.2 allows for flexibility with respect to the choice of potential, to keep things simple a softcore Coulombic potential of the following form is chosen:

$$V(\boldsymbol{r}) = \frac{-Z}{\sqrt{x^2 + y^2 + z^2 + a}} \tag{3.23}$$

Here, Z is equal to the effective nuclear charge seen by the electron in atomic units. By varying this, we can model the scattering from bound electrons of different BE. The parameter a is included to avoid the singularity [52–55] at the origin. While it is preferable to minimize the value of this parameter, there are constraints that arise from the grid-spacing.

With this potential, we proceed as per Sec. 3.2 and obtain the scattering probability, $P_{\boldsymbol{k},\boldsymbol{\epsilon}}$ (see Figs. 3.4 to 3.7).

From the scattering probability calculations for non-linear Compton scattering for different bound state parameters, two things should be noted. First, there *is* a momentum shift, albeit an insignificant one when compared to the shift measured by Fuchs *et al* [18]. Second, Ref. [18] measured a redshift while the simulations show a blue-shift. While the additional shift in Compton wavelength has been well documented and studied [56, 57], interestingly we find that a similar shift occurs in non-linear Compton as well.

We calculate the differential cross section for Compton and non-linear Compton as a function of angle for a bound electron. When we compare the calculated linear Compton differential cross section with the Klein-Nishina formula [3], we find excellent agreement (see Fig. 3.8) despite it being a bound electron. Upon comparing the non-linear Compton differential cross section with Brown and Kibble's result [16], we find a general agreement (see Fig. 3.9). However, the calculated differential cross section for angles between 120° and 150° exhibits about 10% discrepancy. A part of this discrepancy arises from the fact that

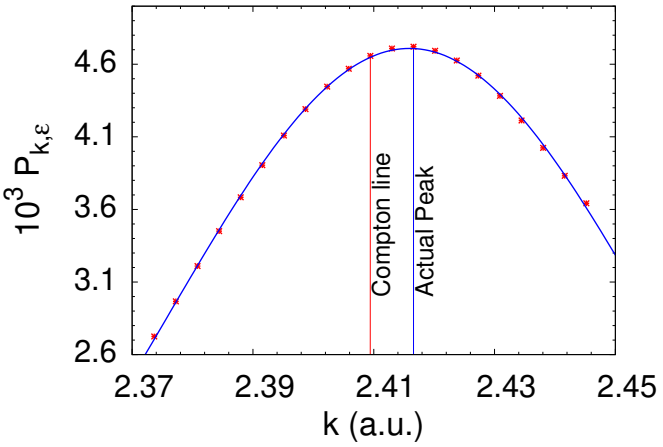

Figure 3.4. The above plot was computed by solving the problem in 2D for $Z = 4$, $a = 0.1$ a.u., with a binding energy(BE) of 5.9593 a.u. at an angle of 130° and $t_{wid} = 1$. It reveals the Compton defect in linear Compton scattering. The red vertical line and the blue vertical line indicates the expected peak (non-relativistic) and the actual peak respectively in the scattered photon momentum k. The red points indicate the results of the numerical calculation and the blue curve indicates a Gaussian fit.

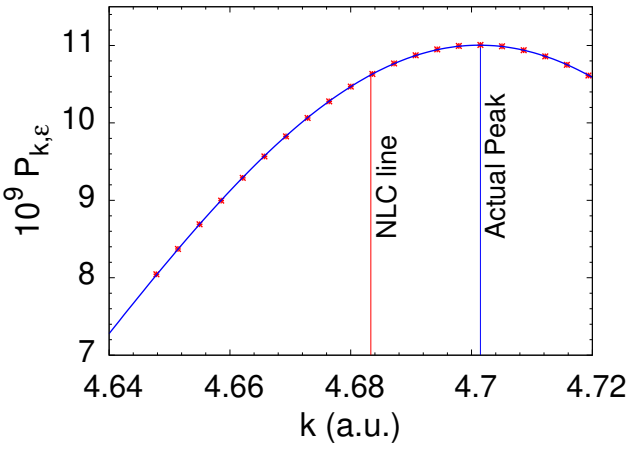

Figure 3.5. The above plot was computed by solving the problem in 2D at an angle of 130° for $Z = 4$, $a = 0.1$ a.u. leading to a binding energy of 5.9593 a.u. The red points indicate the results of the numerical calculation and the blue curve indicates a Gaussian fit. It reveals an analog of the Compton defect in non-linear Compton scattering. The red vertical line and the blue vertical line indicates the expected peak (non-relativistic) and the actual peak respectively in the scattered photon momentum k. Here, $t_{wid} = 1$.

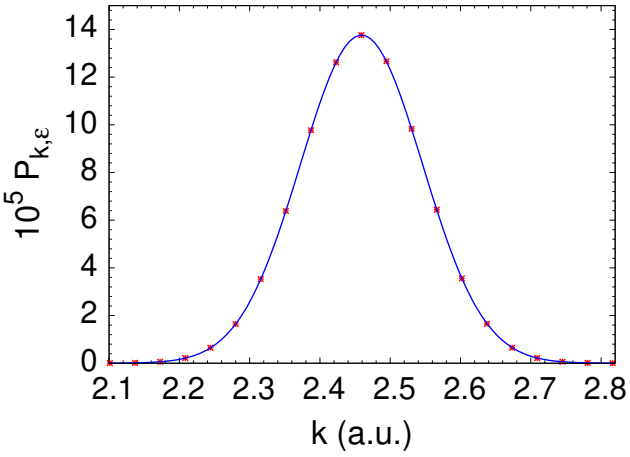

Figure 3.6. Scattering profile for Compton scattering for a bound electron in 3D at an angle of 60° with $t_{wid} = 0.1$. The bound state of the electron is characterised by parameters $Z = 4$, $a = 0.1$ a.u. leading to a BE of 3.9496 a.u. The red points indicate the results of the numerical calculation and the blue line indicates a Gaussian fit.

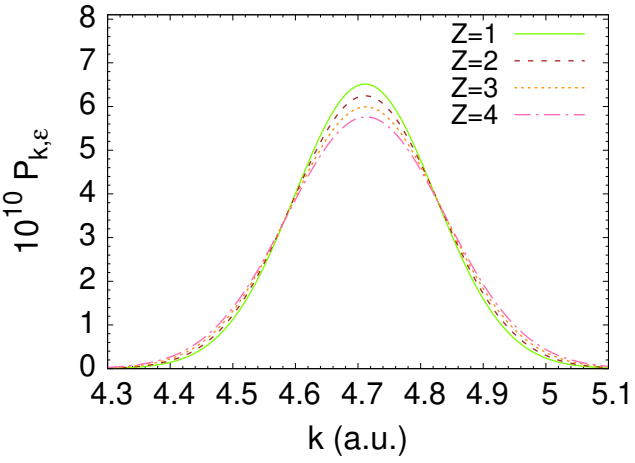

Figure 3.7. Scattering profile for non-linear Compton scattering for a bound electron in 3D at an angle of 120° with $t_{wid} = 0.1$. The figure contains the Gaussian fits from bound states characterised by Z=1, 2, 3, 4 with binding energies (a.u.) 0.4037, 1.322, 2.5345, and 3.9449 respectively. Here $a = 0.1$, $E_C = 107$ a.u., $\omega_{in} = 340$ a.u. In the experiment in Ref. [18], the peak was observed at a k value of ~ 4.5 a.u. , but from the calculations, the bound nature of the electron does not appear to have altered the peak scattered momentum from the free electron value.

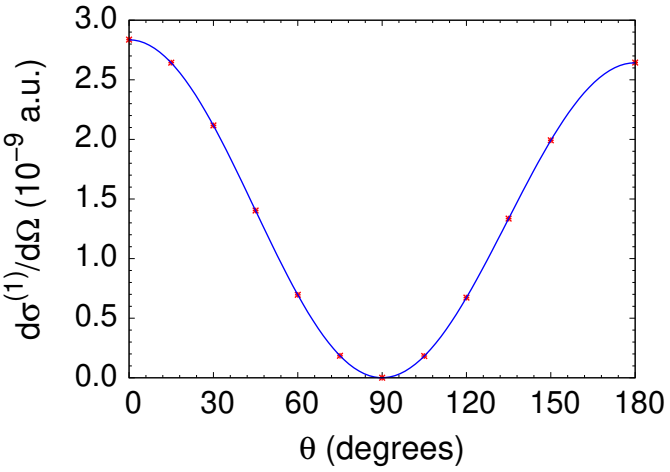

Figure 3.8. Comparison of the differential cross section for Compton scattering from a bound electron as a function of scattering angle with the results of the Klein-Nishina formula. The red points indicate the results of the numerical calculation and the blue line indicates the results of the Klein-Nishina formula. The above calculations were done with the same parameters as in Fig. 3.6. All numerical calculations in 3D were done with no adjustable parameters.

the Brown and Kibble formula used was non-relativistic and therefore is missing factors of $(\frac{\omega_k}{\omega_{in}})$. The differential cross section for Compton scattering from Kibble and Brown is also missing these factors which were included in the Klein-Nishina formula. Therefore, it is difficult to determine the amount of error that originates from the numerical calculation and the amount that originates from the electrons being bound. These calculations were done for a range of values for Z and a and the results were found to be approximately the same.

It is to be noted that the results of Krebs *et al.* [44] are in terms of the double differential cross section and their double differential cross section has an extra frequency factor. Upon finding the area under their curve for double differential cross section by approximating it as a Gaussian and after accounting for differences in frequency, we find that our results are of the same order as theirs and agree to within a factor of $\sim$2. This comparison is approximate because the estimate for the area is crude due to the limited number of data points in the results of Ref. [44].

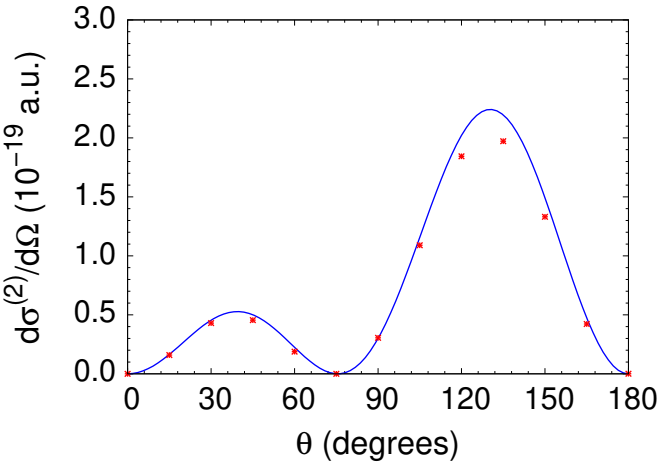

Figure 3.9. Comparison of the differential cross section as a function of scattering angle for non-linear Compton scattering from bound electrons with the Brown and Kibble's free-electron result. The bound electron is characterised by parameters $Z = 4$ and $a = 0.1$ a.u. with a BE of 3.9496. The red points are a result of the numerical calculations in 3D while the blue line indicates the results of Brown and Kibble. The above calculations were done with the same parameters as Fig. 3.7. All numerical calculations in 3D were done with no adjustable parameters.

For all the calculations, the polarization of the scattered photon was in the same plane as that of the plane of polarization of the incoming photons. When the polarization of the scattered photon was chosen to be perpendicular to the plane of polarization of the incoming photons, the scattering probabilities were found to be more than 6 orders of magnitude smaller, for the case of non-linear Compton scattering.

For calculating the additional shifts(defect) in k, we first numerically calculate the average k instead of obtaining the peak momentum from the Gaussian fit. When the polarization of the scattered photon is in the plane of polarization of the incoming photons,

$$k_{avg} = \frac{\sum\limits_{k} kP_k}{\sum\limits_{k} P_k} \tag{3.24}$$

Here k_{avg} is the estimate for the scattered photon momentum that we use to calculate the defect, with respect to the theoretical non-relativistic free electron prediction for both linear

and non-linear Compton scattering. Because the x-rays in the calculation have a Gaussian time dependence, the final momentum distribution is the convolution of the infinite resolution distribution with a Gaussian. The average of the final k is unchanged by the convolution because the Gaussian is a symmetric function while the peak value does slightly shift with the t_{wid}. In the calculations here, the scattering probability falls off slower than a Gaussian distribution for k values far from that for free electron linear and non-linear Compton scattering which leads to small shifts. The underlying cause for this lies in the nature of the Compton profile of the bound electron. Following this, Richardson's extrapolation method [51] is used to obtain an estimate for the defect in scattered photon momentum after accounting for the numerical error from the grid-spacing to the leading order. For the cases of $Z = 1$, 2, 3, and 4 with $a = 0.1$, the defects were found to be of the size of $\sim 10^{-3}$ a.u. in k which corresponds to an energy of about a few eV. It was found that the size of the defect increases with the binding energy of the electron. The defect was also found to be independent of the incident field over the range 1-110 a.u. of electric field amplitude.

Let k_{final} and $k_{initial}$ be the peak scattered momentum of the outgoing x-ray photon and the peak momentum of the incoming x-ray photons respectively. For the case of non-linear Compton scattering from a free electron at an angle of 120°, $k_{final} - k_{initial} \sim$ - 0.25 a.u. From the experiment [18], $k_{final} - k_{initial} \sim$ - 0.5 a.u. From our bound electron calculations, we find that $k_{final} - k_{initial} \sim$ - 0.25 a.u. but there is a small blueshift correction to this which is of the size $\sim + 10^{-3}$ a.u. From these results, it is evident that the bound nature of the electron cannot explain the anomalous shift observed in Ref. [18].

3.3.3 Electron-electron correlation effects

We examine if electron-electron interaction effects could contribute to the redshift in the non-linear Compton scattering. This can be done by a simple extension of the procedure developed in Sec. 3.2. The Hamiltonian is modified to include the mechanical momentum from each electron and an interaction potential is introduced.

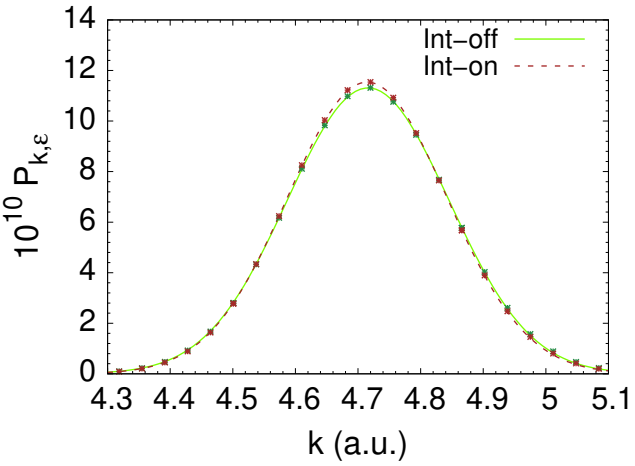

Figure 3.10. Scattering profile for non-linear Compton scattering for an angle of 130°. The curves represent Gaussian fits while the points are the result of the numerical calculation. The dark green points and the green curve represent the case with the electron-electron interaction turned off and the brown points and the brown dotted line indicate the case with the interaction turned on. Here $Z = 4$, $a = 0.1$, $E_C = 107$ a.u., $\omega_{in} = 340$ a.u., $t_{wid} = 0.1$ a.u.

The modified Hamiltonian is given by,

$$\begin{aligned}\hat{H} =& \frac{(\hat{\boldsymbol{P}}_1 + \hat{\boldsymbol{A}}(\boldsymbol{r}_1))^2}{2} + \frac{(\hat{\boldsymbol{P}}_2 + \hat{\boldsymbol{A}}(\boldsymbol{r}_2))^2}{2} + V(\boldsymbol{r}_1) + V(\boldsymbol{r}_2) \\ &+ \frac{1}{\sqrt{(x_1 - x_2)^2 + (y_1 - y_2)^2 + a}} \\ &+ \sum_{\boldsymbol{k},\boldsymbol{\epsilon}} \omega_k \hat{a}^\dagger_{\boldsymbol{k},\boldsymbol{\epsilon}} \hat{a}_{\boldsymbol{k},\boldsymbol{\epsilon}}\end{aligned} \tag{3.25}$$

Here $\boldsymbol{r}_1$ and $\boldsymbol{r}_2$ refer to the position vectors of the electrons and $V(\boldsymbol{r}_1)$ and $V(\boldsymbol{r}_2)$ are the 2D equivalents of the expression in Eq. (3.23). The wave function ansatz remains the same except that the quantities $\psi^{(0)}$ and $\psi^{(1)}_{\boldsymbol{k},\boldsymbol{\epsilon}}$ are now functions of both $\boldsymbol{r}_1$ and $\boldsymbol{r}_2$ along with time t.

With this approach, the calculations have to be restricted to 2D because of the time and space required to handle the problem computationally. Restricting the calculation to 2D is

reasonable given that there was not any significant difference in the 2D and 3D results from Sec. 3.3.1 and Sec. 3.3.2 respectively.

The same numerical procedure discussed in Sec. 3.2.4 is used to obtain the scattering probability $P_{\boldsymbol{k},\boldsymbol{\epsilon}}$ as a function of scattered photon momentum k. A comparison of the calculation with and without the electron-electron interaction does not indicate any significant change (Fig. 3.10).

This calculation is performed with a grid-spacing of 0.14 a.u. and therefore it is not converged to the same extent as the previous calculations. In single bound electron calculations in 2D and 3D, there is no substantial change in the nature of our results as the grid-spacing is decreased from 0.2 to 0.07 a.u. We extrapolate from this trend and argue that the electron-electron correlation effects are unlikely to be the cause of the redshift observed in the experiment by Fuchs *et al.* [18].

3.3.4 Semi-Compton process

We consider a process where a bound electron absorbs an incoming photon and the now-ionised electron scatters another incoming photon inelastically to give rise to a photon of frequency $\sim 2\omega_{in}$. The electron ends up being re-captured by the atom during the process. This process should manifest itself in the calculations if the grid-spacing was decreased enough to access the energy range in the continuum of the ionised electron. When the bound electron absorbs a photon, it gains a momentum of $\sim$ 26 a.u. This would not be represented in a grid with a spacing of 0.1 a.u., hence we consider a grid-spacing of 0.02 a.u.

We resort to a 2D calculation to probe such a fine grid. The calculations do not reveal any significant difference in the scattering profile. We also consider the effect of binding energy on this scattering profile by decreasing the parameter a in the potential. We do not find any significant effect beyond the Compton defect discussed in Sec. 3.3.2 which is at least 2 orders of magnitude smaller than the shift observed by Fuchs *et al.* [18].

3.3.5 Effect of electronic band structure on nonlinear Compton

In this section, we model an electron in a crystal lattice and examine nonlinear Compton scattering from it. For an electron in a crystalline solid, because of the periodic potential and Bloch's theorem, there exists an effective mass for the electron that can be different from its rest mass. This can be observed from the dispersion relation of the electron. Here, we examine if nonlinear Compton scattering can depend on the effective mass of the electron in a solid. There are two motivations for this investigation: First, the experiment by Fuchs et al. involves an x-ray pulse that is incident on solid beryllium in which the electrons reside in a periodic potential. Second, it appears that an electron with an effective mass that is different from the rest mass m_e could perhaps give rise to a Compton and nonlinear Compton shift that is different from the rest mass case. Remember that the Compton and nonlinear Compton shift depends on the mass of the charged particle that scatters the x-ray. We investigate this using a 2D calculation to keep it computationally simple. For the discussions on the validity of a 2D calculation, refer to Sec. 3.3.1.

The electron is initially modelled in a 2D infinite square lattice with the potential modelled by Gaussian wells. This is used to estimate the dispersion relation for the electron in a band. The lattice potential is described by four parameters: the peak of the potential, the full width at half-maximum, and the lattice separation in x and y-direction. For a given crystal momentum, we solve for the ground state eigenfunction for an electron in a unit cell. The wave function at points outside of the unit cell can be obtained using the Bloch condition. The dispersion relation is obtained by plotting the calculated ground-state energy as a function of the crystal momentum. The effective mass for the electron is calculated by examining the dispersion in the neighbourhood of $k \to 0$. Different values of the effective mass can be achieved by varying the parameters of the lattice.

Given the form of the differential equations that describe x-ray scattering [Eq. (3.8) and (3.10)], it is more straightforward to solve the problem in a finite lattice than an infinite lattice. The reason being that in an infinite lattice, the differential equations for the scattering probability [Eq. (3.8) and (3.10)] would have to be recast into the frequency domain instead of time domain. This process can be non-trivial. Instead, to simulate an infinite

lattice, an $N \times N$ array of Gaussian potential wells is used with only a single electron in the entire lattice. By increasing the number of Gaussian wells (N) and examining the scattering profile, the effect of the finiteness of the system can be reduced.

The eigenfunction of the electron calculated for an infinite lattice is spatially delocalised. For a bound state in a finite lattice, the probability density should fall to zero as one approaches the boundaries of the lattice. To achieve this, the zero crystal momentum eigenfunction from the infinite lattice, is modified for a finite lattice by multiplying a masking function. The masking function is chosen such that that the probability density decreases to zero smoothly towards the boundaries of the finite lattice. The wave function thus obtained is used as the starting wave function in the relaxation approach (Sec. 3.2) to obtain the ground state eigenfunction in a finite lattice.

Using the above finite lattice eigenfunction, one can follow the procedure in Sec. 3.2, to obtain the Compton and nonlinear Compton scattering probability as a function of scattered photon momentum. The calculations do not reveal a significant shift in the peak scattered photon momentum as the effective mass is varied from $1.0 - 2.3$ a.u. The calculations were repeated for an array of 6×6, 8×8, and 10×10 Gaussian wells with no noticeable difference in the scattering profile. We also find that the scattering profile for the electron in a finite lattice resembles the scattering profile of an atomic electron of comparable binding energy.

The fact that this scattering profile is largely independent of the effective mass can be understood in the following manner: for the electron in the band, the binding energy is of the size of several eV. This is extremely small compared to the energy of the scattered electron. An estimate for the energy of the scattered electron is given by the maximum Compton shift ($\sim$ 320 eV) and nonlinear Compton shift ($\sim$ 1.2 keV) associated with an incident photon of energy 9.25 keV. After the scattering of the x-ray, the electron ionizes and departs the crystal solid with an enormous kinetic energy relative to its initial binding energy. There is very little propagation of the electron inside the crystal. Therefore, the band structure of the electron plays very little role given the highly inelastic nature of the scattering process.

3.4 Conclusion and summary

We described a method to numerically calculate the linear and non-linear Compton effect for free or bound electrons. The results from the calculation can be used to determine whether the bound nature of the electrons caused the anomalous frequency shift observed in the experiment by Fuchs *et al.* [18]. To justify the approximations we compared our free-electron results with the analytical expressions available for differential cross sections of Compton [3, 45] and non-linear Compton scattering [16]. We found excellent agreement in those cases.

We employed a Coulombic interaction potential to model bound electrons and obtained their differential cross sections for Compton and non-linear Compton scattering. Despite the electrons being bound, the calculations for the differential cross section agreed with the Brown and Kibble results. The calculations did not exhibit a redshift in the wavelength of the scattered photon, in disagreement with the experiment [18] but in agreement with the calculations of Krebs *et al.* [44]. For bound electrons, we also found the small expected blue shift in the case of Compton scattering and interestingly a blue shift in the case of non-linear Compton scattering as well. The role of the band structure of the electron in a crystal in nonlinear Compton scattering was examined. The effective mass of the electron was found to not play a role in the anomalous shift in Fuchs et al. [18]. Our calculations support the conclusion in Ref.[44] that it is not the bound character of the electron that is causing the anomalous frequency shift seen in Fuchs *et al.* [18].

The role of electron-electron correlation effects on the redshift was explored by doing a two-electron calculation in 2D. The results of the calculation did not indicate the presence of the redshift in Ref. [18]. Following this, we considered the case of a semi-Compton process where linear Compton-scattering occurs off of an ionised electron with the electron getting re-captured. This could give rise to a photon of frequency of $\sim 2\omega_{in}$. A calculation accounting for this process, did not exhibit a redshift similar to the one observed in the experiment by Fuchs *et al.* [18]. No reproducible calculations have yet been able to reproduce the shift observed in Ref. [18].

4. INTERFERENCE IN NONLINEAR COMPTON SCATTERING

The contents of this chapter were published as Venkatesh, A., & Robicheaux, F. (2021). Interference in nonlinear Compton scattering using a Schrödinger's equation approach. Physical Review A, **103**, 013111.

4.1 Introduction

The advent of high-intensity sources of light has made it possible to probe a wide range of non-linear phenomenon ranging from multi-photon absorption [12, 58] to higher harmonic generation [11, 59–61]. The progress in x-ray free-electron laser (XFEL) technology [62, 63] in particular has enabled the study of nonlinear Compton scattering. Nonlinear Compton scattering is a term that has been used to refer to several multi-photon scattering processes [14, 15]. In this paper, we restrict our discussions of nonlinear Compton scattering to a process where two incoming photons scatter from a free or a bound electron into one outgoing photon. First theoretically described by Brown and Kibble for free electrons in 1964 [16], it wasn't until 1996 that it could be experimentally confirmed [64]. For an incoming photon of frequency ω_{in}, Brown and Kibble [16] showed that the frequency of the nonlinear Compton scattered photon can be obtained approximately using the Compton expression [2], provided one uses $2\omega_{in}$ for the incoming photon frequency. The scattering angle dependence of the differential cross section for nonlinear Compton scattering [16] substantially differs from that of Compton scattering [3].

Despite the emergence of XFELs, experimental analysis of nonlinear Compton scattering has been challenging. One reason for this difficulty is the small size of the nonlinear Compton signal, even with incident field intensities as high as $\sim 10^{20}\ W/cm^2$ ($E = 107\ a.u.$). In this intensity regime, the nonlinear Compton signal can be six orders of magnitude smaller than the size of the corresponding Compton signal for the same field [65, 66]. The relatively few experiments that have studied nonlinear Compton scattering reflects the difficulty. Another major challenge in such an experiment can be the noise from the XFEL itself [67, 68]. The second harmonic from the XFEL can undergo Compton scattering and add to the noise in

the already small nonlinear Compton signal. Both these challenges were discussed in a recent experiment by Fuchs *et al.* [18].

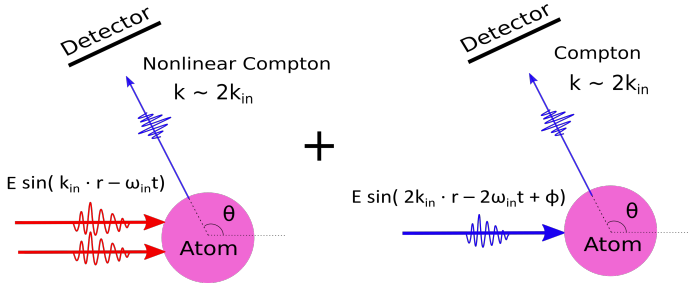

Figure 4.1. A schematic diagram of the interference between Compton and nonlinear Compton scattering from a bound electron using a two-color field. Here k_{in} refers to the momentum of an incoming photon in the case of nonlinear Compton scattering and k refer to the momentum of an outgoing photon.

In this paper, we study the interference in Compton scattering when using a two-color field of frequency ω_{in} and $2\omega_{in}$ with a phase difference. The interference is between the Compton scattered photons of the $2\omega_{in}$ field and nonlinear Compton scattered photons of the ω_{in} field (see Fig. 4.1). Let the intensities of the ω_{in} field and the $2\omega_{in}$ field be $I_{\omega_{in}}$ and $I_{2\omega_{in}}$ respectively. In general, the nonlinear Compton signal scales with the square of the incoming field intensity ($\propto I^2_{\omega_{in}}$) and the Compton signal scales linearly with intensity ($\propto I_{2\omega_{in}}$), for intensities that are within the limits stated in Sec. 4.3.1. The interference term scales as $\propto I_{\omega_{in}}\sqrt{I_{2\omega_{in}}}$. Interference is possible since it cannot be deduced whether the photon came from Compton scattering of the $2\omega_{in}$ field or nonlinear Compton scattering of the ω_{in} field.

This study suggests techniques to overcome two challenges involved in nonlinear Compton scattering experiments. First, the difference in the intensity between the constructively and the destructively interfered scattered waves, combined with pure Compton scattering measurements can help in determining the extent of nonlinear Compton scattering without having to measure the small signal directly. For example, if the nonlinear Compton signal is 6 orders of magnitude smaller than the Compton signal, then the interference would be 3 orders of magnitude smaller. Second, the noise from the second-harmonic of the XFEL

can be determined by examining the interference between Compton and nonlinear Compton scattering. For this, consider the ω_{in} field to be the XFEL fundamental. It gives rise to the desired nonlinear Compton signal at $\sim 2\omega_{in}$ frequency. The second harmonic of the XFEL is the $2\omega_{in}$ field and the Compton scattered photons from this field is the noise at $\sim 2\omega_{in}$ frequency. Introducing a phase factor (ϕ) to the ω_{in} field (or the $2\omega_{in}$ field) and examining the interference can help in identifying the noise.

Several papers in the last few decades, have examined interference effects in multi-photon processes when there occurs an overlap in the initial and final states [69–71]. Using two-color fields to analyze interference effects is also not uncommon. For instance, Yin *et al.* [69] examined the interference in the angular distribution of photo-electrons from single and double-photon ionization from a two-color field. Their experiment revealed an interesting asymmetry in the angular distribution despite the initial state of the atom being spherically symmetric.

The few research works on interference effects involving nonlinear Compton scattering [72, 73] have focused on high-energy electrons where, the frequencies of the incident electromagnetic waves are around the visible region. These works have also relied on a field-theoretic approach. Unlike the previous work, here we focus on the case of x-ray scattering from bound and non-relativistic free electrons and examine the interference using a Schrodinger equation approach. To understand the interference between Compton and nonlinear Compton scattered wave functions, we use a perturbative approach. We study the dependence of the phase shifts on the frequencies of the incoming field and the binding energy (BE) of the electron. This analysis is performed over a range of frequencies from 50 a.u. (1.3 keV) to 680 a.u. (18.5 keV). This choice for the frequency is motivated by the typical frequencies accessible from the XFELs [62, 63] in use and in particular, a recent experiment on nonlinear Compton scattering at the Linac Coherent Light Source at the SLAC National Accelerator Laboratory [18].

This paper is organized as follows: In Sec. 4.2, we discuss the theoretical approach to describe Compton and nonlinear Compton scattering both non-perturbatively and perturbatively in the incoming classical field in the limit of non-relativistic electrons. Then, the procedure for studying the interference using them is described. In Sec. 4.3, the validity of

the perturbative approach is demonstrated. Then the case of interference from a two-color field is discussed.

Unless otherwise stated, atomic units will be used throughout this paper.

4.2 Methods and modeling

4.2.1 Non-perturbative treatment in the classical field

We use a time-dependent Schrödinger equation approach to study nonlinear Compton scattering [65]. The approach is the one described previously [66]. This non-relativistic treatment is well justified [66] in the regime of nonlinear Compton scattering studied in this paper. This section briefly describes the method; see Ref. [66] for a detailed discussion of the derivation.

The Hamiltonian that describes the laser-electron interaction is given by

$$\hat{H} = \frac{(\hat{\boldsymbol{P}} + \hat{\boldsymbol{A}})^2}{2} + V(\hat{\boldsymbol{x}}) + \sum_{\boldsymbol{k},\boldsymbol{\epsilon}} \omega_k \hat{a}^\dagger_{\boldsymbol{k},\boldsymbol{\epsilon}} \hat{a}_{\boldsymbol{k},\boldsymbol{\epsilon}} \tag{4.1}$$

where, $\hat{\boldsymbol{P}}$ and $V(\hat{\boldsymbol{x}})$ refer to the momentum operator and the atomic potential experienced by the electron. The quantity ω_k refers to the angular frequency of the scattered photon. The operators $\hat{a}^\dagger_{\boldsymbol{k},\boldsymbol{\epsilon}}$ and $\hat{a}_{\boldsymbol{k},\boldsymbol{\epsilon}}$ can create or annihilate respectively a photon in the mode $(\boldsymbol{k}, \boldsymbol{\epsilon})$. Here $\boldsymbol{k}$ and $\boldsymbol{\epsilon}$ refer to the momentum and the polarization of the scattered photon respectively. The vector potential $\hat{\boldsymbol{A}}$ is written as the sum of the incoming and scattered EM waves. The incoming wave is treated classically while the outgoing wave is quantized [16, 36]. One can then derive the homogeneous Schrödinger equation for the electron in a classical EM-field and the non-homogeneous Schrödinger equation for the scattering probability amplitude. The equations are derived by only considering terms up to the first order in the quantized field.

The homogeneous Schrödinger equation describing the wave function of an electron in a classical EM field with no outgoing photons is given by

$$\mathrm{i}\frac{\partial \psi^{(0)}}{\partial t} - \hat{H}_C \psi^{(0)} = 0 \tag{4.2}$$

where,

$$\hat{H}_C = \frac{(\hat{\boldsymbol{P}} + \boldsymbol{A_C})^2}{2} + V(\hat{\boldsymbol{x}}). \tag{4.3}$$

The quantity $\boldsymbol{A_C}$ refers to the vector potential of the incoming laser pulse. Note that we do not restrict ourselves to the dipole approximation and therefore we include the full space and time dependence for the vector potential. The explicit space and time dependence ($\boldsymbol{r}$, t) is given by,

$$\begin{aligned} \boldsymbol{A}_C =& \frac{E}{\omega_{in}} \cos\left[(\omega_{in} t - \boldsymbol{k_{in}} \cdot \boldsymbol{r})\right] \\ & \times \exp\left[\frac{(-(2\ln 2)(t - \frac{\hat{\boldsymbol{k}}_{in} \cdot \boldsymbol{r}}{c})^2)}{t_{wid}^2}\right] \boldsymbol{\epsilon_{in}} \end{aligned} \tag{4.4}$$

where the quantities E, ω_{in}, $\boldsymbol{k_{in}}$, t_{wid} and $\boldsymbol{\epsilon_{in}}$ refer to the incoming electric field amplitude, angular frequency, momentum, the full width at half maximum (FWHM) of the pulse intensity and polarization direction respectively. Note that the quantity $\hat{\boldsymbol{k}}_{in}$ refers to a unit vector in the direction of $\boldsymbol{k_{in}}$.

The non-homogeneous Schrödinger equation describes the electron part of the wave function after scattering a photon. It is given by,

$$\begin{aligned} \mathrm{i}\frac{\partial \psi^{(1)}_{\boldsymbol{k},\boldsymbol{\epsilon}}}{\partial t} - \hat{H}_C \psi^{(1)}_{\boldsymbol{k},\boldsymbol{\epsilon}} =& \sqrt{\frac{2\pi}{V\omega_k}} \mathrm{e}^{-\mathrm{i}\boldsymbol{k}\cdot\boldsymbol{r}} \mathrm{e}^{\mathrm{i}\omega_k t} \\ & \times \boldsymbol{\epsilon}^* \cdot (\hat{\boldsymbol{P}} + \boldsymbol{A}_C) W(t) \psi^{(0)}. \end{aligned} \tag{4.5}$$

Here, V refers to the quantization volume that comes from quantizing the outgoing field [36]. The final results for the differential cross section are independent of the quantization volume. The quantity $\psi^{(1)}_{\boldsymbol{k},\boldsymbol{\epsilon}}(\boldsymbol{r}, t)$ refers to the probability amplitude for a scattered photon to be of momentum $\boldsymbol{k}$ and polarization $\boldsymbol{\epsilon}$ and the electron to be found at position $\boldsymbol{r}$ at time t. The quantity W(t), is a windowing function that is used to turn on the source term adiabatically only for the duration of the incoming laser pulse. The reason for W(t) is twofold: First, to prevent the unphysical emission of photons. Second, to find the ground-state of the electron-photon coupled system.

For the atomic potential, we choose the following:

$$V(r) = \frac{-Z}{2\sqrt{r^2+a}}\Big[1 + exp(-r)\Big]. \tag{4.6}$$

Here a is a small parameter used to avoid the singularity at the origin. A value of $a = 0.05$ a.u. is used for all the calculations. The quantity Z, characterizes the effective nuclear charge, which is varied to model a range of binding energies (BE) for the electron. This potential was not chosen to reproduce any atomic orbitals but was chosen to give a range of binding energy, confinement distance, and nuclear charge.

These two equations [Eqs. (4.2) and (4.5)] are solved numerically in a Cartesian grid of points to obtain the scattering probability ($P_{\boldsymbol{k},\boldsymbol{\epsilon}}$) which is the probability density in k-space for a photon to scatter with momentum $\boldsymbol{k}$ and polarization $\boldsymbol{\epsilon}$. The $P_{\boldsymbol{k},\boldsymbol{\epsilon}}$ is defined as,

$$P_{\boldsymbol{k},\boldsymbol{\epsilon}} = \int_v \psi^{(1)^*}_{\boldsymbol{k},\boldsymbol{\epsilon}} \psi^{(1)}_{\boldsymbol{k},\boldsymbol{\epsilon}} d^3r. \tag{4.7}$$

4.2.2 Perturbative approach in the classical field

To understand the phase shifts involved in the interference between Compton and non-linear Compton scattering, a perturbative approach in the classical field is used. We begin by expanding the wave function perturbatively in powers of the incoming *classical* field:

$$\psi^{(0)} = \psi^{(0)}_0 + \psi^{(0)}_1 + \psi^{(0)}_2 + ... \tag{4.8}$$

The subscript refers to the order of the incoming classical field and the superscript refers to the order of the outgoing quantized field. For example, the quantity $\psi^{(0)}_1$ refers to the term that is zeroth order in the quantized field but first order in the classical field.

One can then substitute Eq. (4.8) in the homogeneous Schrödinger equation [Eq.(4.2)]. Separating out the terms based on the order of the classical field, the equations for the corresponding wave functions can be derived. The equations for the wave function that is zeroth, first and second order in the classical field respectively are given by:

$$\mathrm{i}\frac{\partial \psi^{(0)}_0}{\partial t} - \hat{H}_a \psi^{(0)}_0 = 0 \tag{4.9}$$

$$\mathrm{i}\frac{\partial \psi_1^{(0)}}{\partial t} - \hat{H}_a \psi_1^{(0)} = \hat{\boldsymbol{P}} \cdot \boldsymbol{A}_C \ \psi_0^{(0)} \tag{4.10}$$

$$\mathrm{i}\frac{\partial \psi_2^{(0)}}{\partial t} - \hat{H}_a \psi_2^{(0)} = (\hat{\boldsymbol{P}} \cdot \boldsymbol{A}_C) \ \psi_1^{(0)} + \frac{\boldsymbol{A}_C^2}{2} \ \psi_0^{(0)} \tag{4.11}$$

where,

$$\hat{H}_a = \frac{\hat{\boldsymbol{P}}^2}{2} + V(\hat{\boldsymbol{x}}). \tag{4.12}$$

The quantity $\psi_0^{(0)}$ refers to the electronic wave function that does not depend on the external field. $\psi_1^{(0)}$ and $\psi_2^{(0)}$ are the probability amplitudes for the electron to absorb one and two photons respectively.

Similarly, the first order wave function in the quantized field $\psi^{(1)}_{\boldsymbol{k},\boldsymbol{\epsilon}}$, can also be expanded in a perturbative power series in the classical field:

$$\psi^{(1)} = \psi_0^{(1)} + \psi_1^{(1)} + \psi_2^{(1)} + ... \tag{4.13}$$

Note that, the subscripts $\boldsymbol{k}, \boldsymbol{\epsilon}$ have been dropped from $\psi^{(1)}$ to reduce clutter in the notation. But one has to keep in mind that every term that is first order in the quantized field will depend on these quantities.

Substituting Eq.(4.13) in the non-homogeneous Schrödinger equation [Eq. (4.5)] and separating out the terms based on the order of the classical field yields the following equations for the wave function that is zeroth, first, and second order in the classical field respectively:

$$\begin{aligned}\mathrm{i}\frac{\partial \psi_0^{(1)}}{\partial t} - \hat{H}_a \psi_0^{(1)} =& \sqrt{\frac{2\pi}{V\omega_k}} \mathrm{e}^{-\mathrm{i}\boldsymbol{k}\cdot\boldsymbol{r}} \mathrm{e}^{\mathrm{i}\omega_k t} \\ & \times \boldsymbol{\epsilon}^* \cdot \hat{\boldsymbol{P}} \ \psi_0^{(0)} \ W(t)\end{aligned} \tag{4.14}$$

$$\begin{aligned}\mathrm{i}\frac{\partial \psi_1^{(1)}}{\partial t} - \hat{H}_a \psi_1^{(1)} =& \sqrt{\frac{2\pi}{V\omega_k}} \mathrm{e}^{-\mathrm{i}\boldsymbol{k}\cdot\boldsymbol{r}} \mathrm{e}^{\mathrm{i}\omega_k t} \\ & \times \boldsymbol{\epsilon}^* \cdot (\hat{\boldsymbol{P}} \ \psi_1^{(0)} + \boldsymbol{A_C} \ \psi_0^{(0)}) \ W(t) \\ & + (\boldsymbol{A_C} \cdot \hat{\boldsymbol{P}}) \psi_0^{(1)}\end{aligned} \tag{4.15}$$

$$
\begin{aligned}
\mathrm{i}\frac{\partial \psi_2^{(1)}}{\partial t} - \hat{H}_a \psi_2^{(1)} = & \sqrt{\frac{2\pi}{V\omega_k}} \mathrm{e}^{-\mathrm{i}\boldsymbol{k}\cdot\boldsymbol{r}} \mathrm{e}^{\mathrm{i}\omega_k t} \\
& \times \boldsymbol{\epsilon}^* \cdot (\hat{\boldsymbol{P}}\ \psi_2^{(0)} + \boldsymbol{A_C}\ \psi_1^{(0)})\ W(t) \\
& + (\boldsymbol{A_C} \cdot \hat{\boldsymbol{P}})\ \psi_1^{(1)} + \frac{\boldsymbol{A_C^2}}{2}\ \psi_0^{(1)}
\end{aligned}
\tag{4.16}
$$

Here, $\psi_0^{(1)}$ describes the probability amplitude of having one outgoing photon of momentum $\boldsymbol{k}$ and polarization $\boldsymbol{\epsilon}$ when there is no incoming field and the electron to be in position $\boldsymbol{r}$ at time t. Similarly, $\psi_1^{(1)}$ is the probability amplitude for the case with one outgoing photon and one incoming photon being absorbed and $\psi_2^{(1)}$ refers to the case with one outgoing photon but with two incoming photons being absorbed. A detailed analysis of the source terms can be found in Sec. 4.3.2.

These perturbative equations [Eq. (4.9) - (4.16)] are solved simultaneously using the same numerical framework that was developed in Ref. [66] to solve the equations summarized in Sec. 4.2.1.

4.2.3 Two-color field

To study the interference, we replace the single incoming laser pulse with two pulses of different frequencies. For the case where one of the incoming pulses has a frequency twice that of the other, the dominant interference pattern would consists of linear Compton photons from the $2\omega_{in}$ field and nonlinear Compton photons from the ω_{in} field.

The effect of the two-color pulse is examined both non-perturbatively as well as perturbatively. In the non-perturbative treatment (Sec. 4.2.1), this is simulated by simply choosing the incoming vector potential as the resultant of the two vector potentials from each incoming pulse. In the perturbative treatment (Sec. 4.2.2), each incoming pulse is treated perturbatively and the results for $\psi^{(1)}$ from each pulse is superposed to obtain the total scattering probability.

We choose the full width at half maximum of the pulse intensity (t_{wid}) of the $2\omega_{in}$ field to be $1/\sqrt{2}$ of that of the ω_{in} field. This is motivated by a preference for a large overlap for

the scattering probability in k-space between Compton and nonlinear Compton scattered photons. The pulse widths are chosen in this manner since, it is the second order wave function ($\psi_2^{(1)}$) that matters for nonlinear Compton and A_C^2 effectively would have $1/\sqrt{2}$ of the pulse width of A_C.

4.2.4 Convergence

The amount of convergence is determined in the interference calculations by examining the relative change in the total differential cross section. For the calculations in Fig. 4.2, the difference in the differential cross section between a grid size of 24 a.u. and 16 a.u. was under 10^{-3}%. The difference in the differential cross section between a grid spacing of 0.1 a.u. and 0.07 a.u. was below 0.8%. In Fig. 4.3, for Z=4 and a scattering angle of 135°, the difference in the calculated differential cross section between a grid size of 24 a.u. and 16 a.u. was under 10^{-9}%. The difference in the differential cross section between a grid spacing of 0.1 a.u. and 0.07 a.u. was below 0.08%. For the calculations in Fig. 4.6, the difference in the differential cross section between a grid size of 30 a.u. and 40 a.u. is under 10^{-9}%. The difference in the differential cross section between a grid spacing of 0.1 a.u. and 0.07 a.u. was below 0.09%. For a discussion on the choice of other parameters, see Sec. 4.3.

4.3 Applications

4.3.1 Perturbative vs non-perturbative

The region of interest involves incoming x-rays with frequencies (ω_{in}) between 50 a.u. and 680 a.u. and electric field amplitudes (E) up to a few hundred atomic units which is typical of XFELs in use [62, 63]. In this regime, we find that for the case of linear Compton scattering, a perturbative treatment in the first order in the classical field [Eqs. (4.9), (4.10), (4.14) and (4.15)] is adequate to describe the problem both for free electrons as well as bound electrons. Nonlinear Compton scattering however, requires a second-order perturbative calculation in the classical field [Eqs. (4.9) - (4.16)].

For the case of nonlinear Compton scattering, the results for the scattering probability obtained from the second order perturbative calculations reveal an excellent agreement with

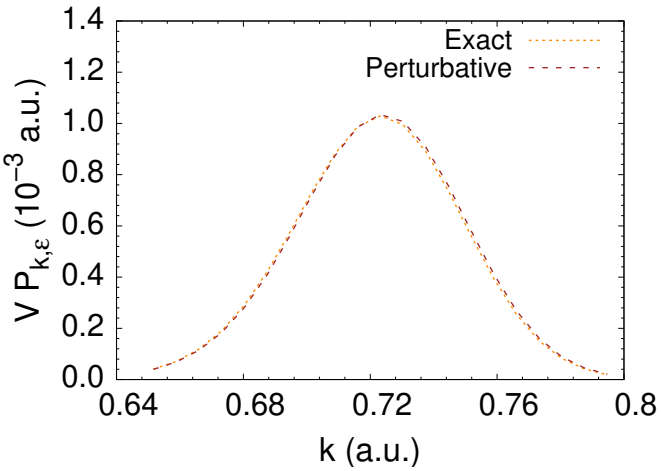

Figure 4.2. Comparison of the results of the non-perturbative treatment and a second-order perturbative calculation in the classical field for the case of nonlinear Compton scattering. The results show a good agreement between the two in the chosen regime. Here $\omega_{in} = 50$ a.u., $E = 502.9$ a.u., $t_{wid} = 0.5$ a.u., $\theta = 135°$, $Z = 4$ and $a = 0.05$ with a binding energy (BE) of 3.306 a.u.

the non-perturbative calculations (Fig. 4.2). Note that the validity of the perturbative expansion depends on the magnitude of $\boldsymbol{A_C}$ ($\sim E/\omega_{in}$). For ω_{in}=50 a.u. and electric fields (E) below $\sim$ 600 a.u. we find that the scattering probability for nonlinear Compton scattering scales with the square of the intensity of the incident wave. As the electric field is increased beyond $E \sim 600$ a.u. (with the other parameters fixed), the scattering probability starts exhibiting non-perturbative behavior.

It is to be noted that in this regime, Compton scattering adheres to first order perturbative behavior in the classical field as well as the quantized field.

4.3.2 Interference between Compton and nonlinear Compton

We now examine the interference effect in the scattered photons when the incoming field consist of two different frequencies with one being twice that of the other and with a phase shift (ϕ) imposed on the $2\omega_{in}$ field.

To understand how the phase difference in the incoming field affects the scattering probability, we use the perturbative framework developed in Sec. 4.2.2. The interference between

the Compton scattered photons and nonlinear Compton scattered photons from the two incoming fields can be understood as the superposition of the scattering probability amplitudes from each field alone. For Compton scattering from the $2\omega_{in}$ field, a first order perturbative calculation in the classical field is used to obtain the scattering probability amplitude. For nonlinear Compton scattering from the ω_{in} field, a second order perturbative calculation is needed.

The resultant scattering probability amplitude leading to photons with momentum $\sim 2k_{in}$ is given by,

$$\psi^{(1)}_{total} = \psi^{(1)}_{1,2\omega_{in}}(\phi) + \psi^{(1)}_{2,\omega_{in}} \tag{4.17}$$

where the first term on the right-hand side ($\psi^{(1)}_{1,2\omega_{in}}(\phi)$) is the Compton scattering probability amplitude from the $2\omega_{in}$ field which is first order in the classical field. The second term ($\psi^{(1)}_{2,\omega_{in}}$) is the nonlinear Compton scattering probability amplitude from the ω_{in} field that is second order in the classical field. Here $\psi_{1,2\omega_{in}}$ depends on the phase shift ϕ. Also, only the two terms that are in Eq. (4.17) are relevant because the frequency bandwidth of the incoming field is small compared to the frequency ω_{in} so that the peaks in the scattering probabilities [Eq. (4.7)] are localized in k-space.

In Eq. (4.17), the phase dependence of $\psi^{(1)}_{1,2\omega_{in}}(\phi)$ can be determined by examining the three source terms in the first order non-homogeneous differential equation [Eq. (4.15)]. The first source term (S1) determined by $\hat{\boldsymbol{P}}\ \psi^{(0)}_1$, is due to photo-absorption, the second source term (S2) determined by $\boldsymbol{A_C}\ \psi^{(0)}_0$, is due to pure Compton scattering, the third (S3) determined by $\boldsymbol{A_C}\cdot\hat{\boldsymbol{P}}\psi^{(1)}_0$, describes the laser-dressing of virtual photon emission. Note that all three terms depend on $\boldsymbol{A_C}$. The $\boldsymbol{A_C}$ being real contains terms of the form $e^{i(2k_{in}\cdot r-2\omega_{in}t+\phi)}$ and $e^{-i(2k_{in}\cdot r-2\omega_{in}t+\phi)}$, where $2\omega_{in}$ and $2k_{in}$ refers to the angular frequency and momentum respectively of the incoming field. One can then employ the rotating wave approximation, which would result in only the term with $e^{i(2k_{in}\cdot r-2\omega_{in}t+\phi)}$ surviving. This leads to the phase factor ($e^{i\phi}$) appearing in every source term (S1, S2 and S3) and hence the final wave function ($\psi^{(1)}_1$) for that field. Therefore Eq. (4.17) becomes,

$$\psi^{(1)}_{total} = \psi^{(1)}_{1,2\omega_{in}}(0)\ \mathrm{e}^{\mathrm{i}\phi} + \psi^{(1)}_{2,\omega_{in}} \tag{4.18}$$

where $\psi^{(1)}_{1,2\omega_{in}}(0)$ is calculated at $\phi = 0$.

The contribution from the three source terms to $\psi^{(1)}_{1,2\omega_{in}}$ are not of the same size. Given that the incoming EM waves are in the x-ray regime, the photo-absorption term (S1) is small with respect to the Compton term (S2) [74, 75]. Also, the contribution from the terms S1 and S3 appear to be of comparable size to each other, but they appear to have a phase factor between them. Their combined scattering probability amplitude is found to be an order of magnitude lower than each of them individually.

As an added check on the approximations made so far, we compared our results from both the non-perturbative and perturbative approaches and they showed an excellent agreement within the perturbative regime.

From the total scattered wave function, $\psi^{(1)}_{total}$, the total scattering probability P_{Tot} can be obtained.

$$\begin{aligned} P_{Tot} = &\int_v |\psi^{(1)}_{1,2\omega_{in}}|^2\ d^3r + \int_v |\psi^{(1)}_{2,\omega_{in}}|^2\ d^3r \\ &+ \int_v \Big(\mathrm{e}^{-\mathrm{i}\phi} \psi^{(1)\ *}_{1,2\omega_{in}}\ \psi^{(1)}_{2,\omega_{in}} \\ &+ \mathrm{e}^{\mathrm{i}\phi} \psi^{(1)}_{1,2\omega_{in}}\ \psi^{(1)\ *}_{2,\omega_{in}} \Big)\ d^3r \end{aligned} \tag{4.19}$$

Of the 4 terms on the right-hand side, the first term represents the Compton scattering probability and scales linearly with intensity ($\propto I_{2\omega_{in}}$). The second term represents the nonlinear Compton scattering probability and scales quadratically with the intensity($\propto I^2_{\omega_{in}}$). The third and fourth terms together gives rise to the interference. Both the third and the fourth terms are $\propto I_{\omega_{in}}\sqrt{I_{2\omega_{in}}}$. To illustrate this dependence, consider the case when scattering probability for nonlinear Compton is 1% of that of Compton. Then, the interference term can be as large as ∼20% of the Compton scattering probability.

We choose the two incoming fields to be of equal electric field amplitude with $E = 107$ a.u., with polarizations in the same direction and frequency $\omega_{in} = 170$ a.u. The scattered

photon momentum and its polarization are both chosen to be in the same plane as the incoming fields and a range of scattering angles (θ) from 0° to 180° are considered. Other cases for these quantities are explored after that.

We evaluate the differential cross section from the total scattering probability [Eq. (4.19)] using the expression for one-photon differential cross section from Ref. [66]. The differential cross section is then given by,

$$\frac{\mathrm{d}\sigma}{\mathrm{d}\Omega}^{(1)} = \frac{2V\omega_{in}}{(2\pi)^3}\frac{\int \sum_{\epsilon} P_{Tot} k^2 dk}{\int I_{2\omega_{in}} dt}. \tag{4.20}$$

Note that we use the Compton differential cross section expression even though the total scattered wave function is the result of interference between Compton and nonlinear Compton. For the intensities chosen ($E = 107$ a.u. for both), this is reasonable since the Compton scattering probability is at least 3 orders of magnitude more than the nonlinear Compton scattering probability. As a reminder, for the case of free-electrons, the differential cross section for Compton scattering is given by the Klein-Nishina formula [3] and for nonlinear Compton scattering is described by Brown and Kibble [16].

In the case of interference between linear and nonlinear Compton scattering, from Eqs. (4.19) and (4.20), we expect the differential cross section to be of the following form:

$$\frac{\mathrm{d}\sigma}{\mathrm{d}\Omega} = C + D\ cos(\phi - \delta). \tag{4.21}$$

Here C is the Klein-Nishina differential cross section for Compton scattering when the scattering probability for non-linear Compton is much smaller than that of linear Compton. D arises from the interference term in Eq. (4.19) and is proportional to $I_{\omega_{in}}/\sqrt{I_{2\omega_{in}}}$. The quantity δ is the intrinsic phase shift between the probability amplitude of Compton and nonlinear Compton scattering.

The results of the calculation are shown in Fig. 4.3 ($\theta = 135°$) and Fig. 4.4 ($\theta = 84°$). The results are consistent with the dependence expected [Eq. (4.21)]. The plot (Fig. 4.3) shows that the intrinsic phase difference (δ) between the scattering probability amplitude of Compton and nonlinear Compton to be zero for $\theta = 135°$. Further investigation reveals that

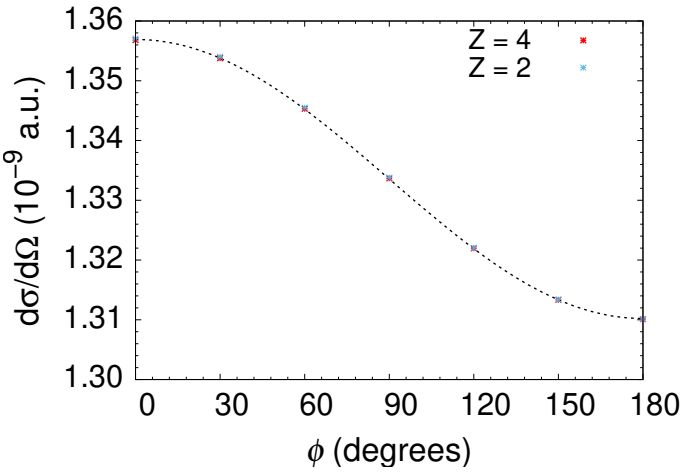

Figure 4.3. The figure shows the differential cross section computed using the interfered wave functions from Compton and nonlinear Compton scattering as a function of the imposed phase difference ϕ on the $2\omega_{in}$ field for a scattering angle of 135°. The dotted line is a curve fit of the form C + D cos ϕ. The plot reveals that there is no intrinsic phase difference between the Compton and nonlinear Compton scattered wave functions. It is clear, there is almost no effect of the binding energy (BE) on the interference pattern in the chosen parameter regime. Here ω_{in} = 170 a.u. , E = 107 a.u. , t_{wid} = 0.1 a.u. for the ω_{in} field. Both initial and final polarizations are in the scattering plane. The BE for $Z = 2$ and $Z = 4$ are 0.8744 a.u. and 3.306 a.u. respectively. The parameter a remains the same for both with a = 0.05 a.u.

the intrinsic phase difference δ depends on the scattering angle θ (see Fig. 4.5). It is zero for scattering angles between $\theta = 0$ and $\theta \sim 75°$ which is a zero of the nonlinear Compton differential cross section. If the scattering angle is increased beyond this value ($\theta \sim 75°$), the intrinsic phase difference (δ) jumps to a value of $\boldsymbol{\pi}$ (Fig. 4.4) and it drops back to zero if you increase θ beyond 90°. It is evident that the intrinsic phase difference switches between a value of 0 or $\boldsymbol{\pi}$ every time the scattering angle crosses a zero of the differential cross section of Compton or nonlinear Compton scattering [16]. This is confirmed if one chooses a negative scattering angle. For $\theta = -30°$, the intrinsic phase difference is $\boldsymbol{\pi}$ because there lies a zero of the differential cross section for nonlinear Compton scattering at $\theta = 0°$. Note that the Compton scattering differential cross section [3] given by the Klein-Nishina formula *does not*

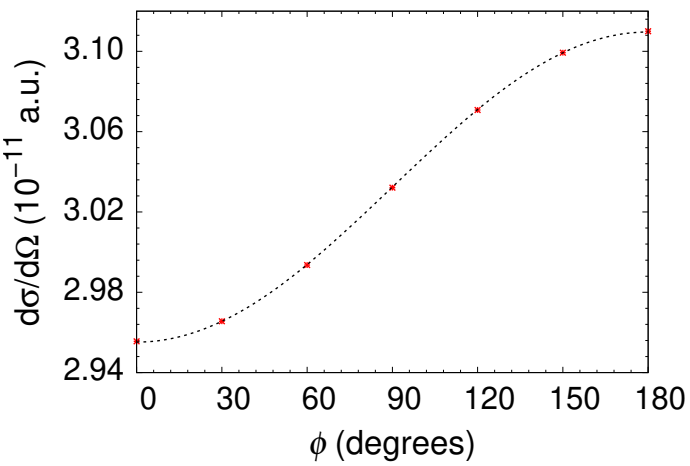

Figure 4.4. The figure shows the differential cross section computed using the interfered wave functions from Compton and nonlinear Compton scattering as a function of the imposed phase difference ϕ on the $2\omega_{in}$ field for a scattering angle of 84°. The dotted line is curve fit of the form C + D cos ϕ. The plot reveals that there is a intrinsic phase difference of $\boldsymbol{\pi}$ between the Compton and nonlinear Compton scattered wave functions. Here Z= 4 with the other parameters remaining the same as in Fig. 4.3.

have a zero but rather a minimum at $\theta \sim 90°$. But, for our non-relativistic calculation the differential cross section appears to go to zero in the absence of the Compton profile.

A comparison of the scattering angle dependence of C and the Klein-Nishina formula gave a good agreement. The quantities C and D also exhibit a dependence on the incoming frequencies similar to the one expected based on the Klein-Nishina formula [3] and the differential cross section from Brown and Kibble [16]. Also it is evident from Fig. 4.3, that the binding energy(BE) of the ground state of the electron does not have a significant effect on the interference between Compton and nonlinear Compton scattering.

We examine if the intrinsic phase difference (δ) depends on the pulse width (t_{wid}). We increase the t_{wid} to 3 a.u., which is 30 times the pulse width used in Fig. 4.3. There are computational challenges associated with this long calculation, so a 2D calculation is performed instead. For a detailed discussion on a 2D treatment of nonlinear Compton scattering, see Ref. [66]. For this calculation, fields with different intensities are chosen to illustrate the difference in their scattering profile. The electric field amplitudes for ω_{in} field ($E_{\omega_{in}}$) and

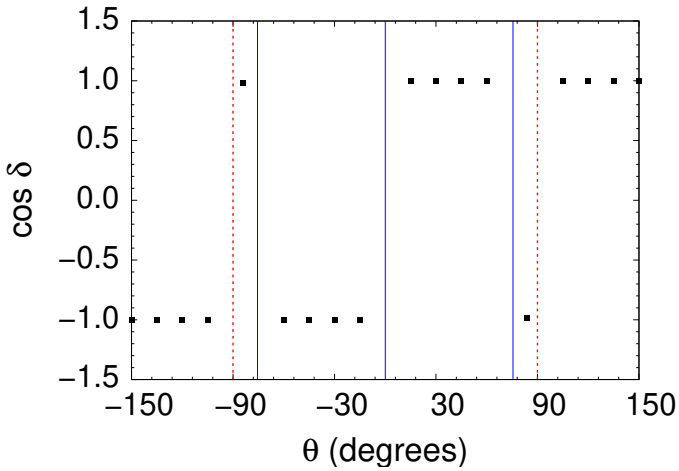

Figure 4.5. The figure shows the dependence of the intrinsic phase difference δ (black dots) versus the scattering angle θ. The blue solid line indicates the zeroes in the differential cross section of Brown and Kibble [16]. The red dotted line indicates the zeroes in the differential cross section of Compton scattering. The calculation reveals a discontinuous jump in the intrinsic phase difference (δ) at scattering angles which are zeroes of the differential cross section for Compton or nonlinear Compton scattering [16]. Here Z= 4 with the other parameters remaining the same as in Fig. 4.3

$2\omega_{in}$ field ($E_{2\omega_{in}}$), are chosen to be 10.7 a.u. and 0.535 a.u. respectively. The results of the 2D calculation reveal an intrinsic phase difference (δ) that is 0 or π depending on the scattering angle. Increasing the pulse width decreases the bandwidth of the incoming pulse. The shorter bandwidth reveals two scattering mechanisms for the incoming photons (see Fig. 4.6). In Fig. 4.6, the first peak $k \sim 2.41$ a.u. centered around the Compton scattered momentum for the $2\omega_{in}$ field, arises from the inelastic scattering of the incoming photons by the electron. The second peak $k \sim 2.48$ a.u., sharply centered around the incoming wavenumber of the $2\omega_{in}$ field, arises from the elastic scattering of the incoming photons by the electron, leaving the electron in the ground state. Note that the contribution of this elastic scattering peak to the overall area under the curve is small (see Fig. 4.6). The figure (Fig. 4.6) shows that the intrinsic phase difference between the Compton and non-linear Compton scattering is the same for the elastic and the inelastic process.

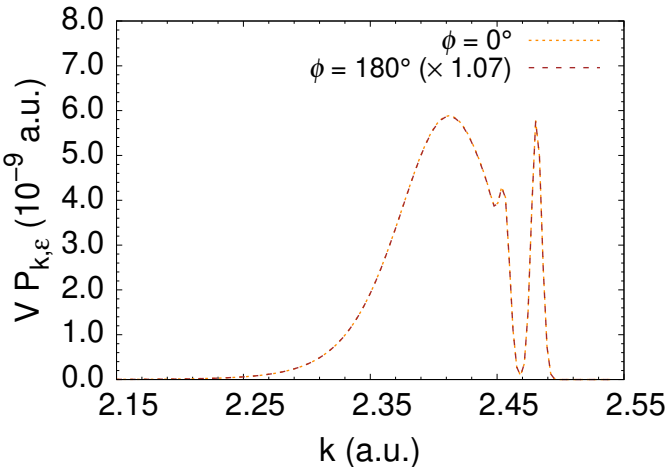

Figure 4.6. The results of a 2D calculation for the total scattering probability as a function of scattered photon momentum for the interference between Compton and nonlinear Compton scattering from a two-color field. The two curves correspond to the cases when the imposed phase difference (ϕ) is 0° (constructive) and 180° (destructive). The curve corresponding to $\phi = 180°$ has been scaled by a constant factor to make it coincide with the $\phi = 0°$ curve at the first peak. The first peak ($k \sim 2.41$ a.u.) describes the case of inelastic scattering of the incoming photons from the electron and the second peak ($k \sim 2.48$ a.u.) describes elastic scattering. The coincidence of the two curves ($\phi = 0°$ and $\phi = 180°$) reveals that the elastic and the inelastic scattering processes have the same relative phase. Here $\omega_{in} = 170$ a.u. , $E_{\omega_{in}} = 10.7$ a.u. , $E_{2\omega_{in}} = 0.535$ a.u. , $t_{wid} = 3$ a.u. , $Z = 4$ and $a = 0.1$ a.u. with BE = 4.805 a.u.

The effect of polarization directions can be interesting. For a single incoming field, there are 4 possible orientations based on the direction of the incoming field's polarization(ϵ_{in}) and momentum(k_{in}) and the polarization (ϵ) and the momentum (k) of the outgoing fields. We choose the 4 cases in the following manner:

(i) Case 1: $\boldsymbol{\epsilon_{in}} = \hat{y}$, $\boldsymbol{k_{in}} = \hat{x}$, $\boldsymbol{\epsilon} = -\hat{x}\ sin\ \theta + \hat{y}\ cos\ \theta$ and $\boldsymbol{k} = \hat{x}\ cos\ \theta\ + \hat{y}\ sin\ \theta$; i.e. the initial and final polarizations in the scattering plane.

(ii) Case 2: $\boldsymbol{\epsilon_{in}} = \hat{y}$, $\boldsymbol{k_{in}} = \hat{x}$, $\boldsymbol{\epsilon} = \hat{z}$ and $\boldsymbol{k} = \hat{x}\ cos\ \theta + \hat{y}\ sin\ \theta$; i.e. the initial polarization in the scattering plane but the final polarization perpendicular to the scattering plane.

(iii) Case 3: $\boldsymbol{\epsilon_{in}} = \hat{z}$, $\boldsymbol{k_{in}} = \hat{x}$, $\boldsymbol{\epsilon} = -\hat{x}\ sin\ \theta + \hat{y}\ cos\ \theta$ and $\boldsymbol{k} = \hat{x}\ cos\ \theta + \hat{y}\ sin\ \theta$; i.e. the initial polarization perpendicular to the scattering plane but the final polarization in the scattering plane.

(iv) Case 4: $\boldsymbol{\epsilon_{in}} = \hat{z}$, $\boldsymbol{k_{in}} = \hat{x}$, $\boldsymbol{\epsilon} = \hat{z}$ and $\boldsymbol{k} = \hat{x}\ cos\ \theta + \hat{y}\ sin\ \theta$; i.e. the initial and final polarizations perpendicular to the scattering plane.

Note that for interference to be possible, the scattered photons from both Compton and nonlinear Compton should have the same final polarization and momentum vector. Also, for nonlinear Compton scattering, from Ref. [16] only Case 1 and Case 3 are expected to yield non-zero scattering probabilities (more on this point later). Therefore based on these two requirements, only the interference cases with Compton scattering corresponding to Case 1 or Case 3 and nonlinear Compton scattering pertaining to Case 1 or Case 3 are significant. The results presented so far (Figs. 4.3 - 4.6) correspond to Case 1 for both linear and nonlinear Compton scattering. While we expect this to be the dominant case from Ref. [3] and Ref. [16], the other cases become relevant when one considers the interference effects from crossed polarizations or from unpolarized photons. From here on, a short-hand notation of say Case 1 - Case 3 refers to the interference when the Compton scattering pertains to Case 1 and nonlinear Compton scattering pertains to Case 3.

The nonlinear Compton scattering probability pertaining to Case 3, is expected to be approximately the same size as Case 1 from Ref. [16]. For $\theta \in [0, 180]$ the differential cross section for Case 1 has zeroes at $\theta = 0°, \sim 75°$ and $180°$ but Case 3 has zeroes only at $\theta = 0°$ and $180°$. We examine Case 1 - Case 3 interference for the same set of parameters as Fig. 4.5. The intrinsic phase difference δ is found to have a similar dependence on the scattering angle to that of Case 1 - Case 1 interference in that, it switches between 0 or $\boldsymbol{\pi}$ every time the scattering angle crosses a zero of the differential cross section of Compton or nonlinear Compton scattering [16]. For a given scattering angle, the calculations with $Z = 2$ and $Z = 4$ show a small difference in the differential cross sections of about ~ 0.014 %. But, they both still have the same intrinsic phase δ.

The polarization directions are chosen to be Case 3 for Compton scattering and Case 1 for nonlinear Compton scattering. This is an interesting case because for such an arrangement

we expect the nonlinear Compton signal to be comparable to the Compton signal. This arises out of the interplay of two factors. First, for the chosen intensity ($E = 107$ a.u.) nonlinear Compton signal from the incoming field is less than that of the Compton signal. Second, the Compton scattering for this arrangement is suppressed because of the choice of polarization (Case 3). The results of the calculation reveal that the size of the Compton scattered wave function ($\psi^{(1)}_{1,2\omega_{in}}$) is in fact comparable to that from nonlinear Compton scattering ($\psi^{(1)}_{2,\omega_{in}}$). However, no interference occurs because the scattered wave function for Compton scattering and that for nonlinear Compton scattering are found to be orthogonal to each other. This is found to be a consequence of the fact that the Compton scattered wave function is anti-symmetric in the $\hat{z}$ direction but the nonlinear Compton scattered wave function is symmetric along the same direction. These symmetries can be deduced from the form of the perturbation equations.

Consider the equations from the perturbative approach (Sec. 4.2.2) keeping in mind our choice of Case 3 for Compton scattering and Case 1 for nonlinear Compton scattering. The symmetric or the anti-symmetric nature of the scattered wave function can be understood by tracking the effect of the source terms involved. The Hamiltonian for the atomic electron (H_a) is parity-symmetric and the starting wave function ($\psi^{(0)}_0$) being the ground state of the electron is symmetric. The source terms in all the equations from Eq. (4.9) - (4.11) and from Eq. (4.14) - (4.16), have definite parity in the z-direction. Therefore, the wave functions of different perturbative order also have definite parity in the z-direction, since the homogeneous part of the equations preserves parity. One can track the changes in the parity of the ground state wave function of the electron ($\psi^{(0)}_0$) from each source term in the first order perturbative treatment for Compton scattering and the second order treatment for nonlinear Compton scattering respectively. Such an analysis can be used to determine that the scattered wave function for Compton scattering ($\psi^{(1)}_{1,2\omega_{in}}$) is anti-symmetric in the z-direction for Case 3 and the scattered wave function for nonlinear Compton scattering ($\psi^{(1)}_{2,\omega_{in}}$) is symmetric in the z-direction for Case 1.

For the scenario, when Compton scattering corresponds to Case 3 and nonlinear Compton scattering corresponds to Case 3, we find that similar to the previous case there is no interference. Again, one can use a similar approach using perturbative equations to deduce

that the Compton scattered wave function for Case 3 is anti-symmetric and the nonlinear Compton scattered wave function for Case 3 is symmetric in z.

Upon exploring other cases for polarization, we find that for some cases we expect a zero scattering probability for nonlinear Compton scattering. Consider the case when the polarization of the scattered photons for nonlinear Compton pertains to Case 4. From Ref. [16], one would expect a zero scattering probability. The calculations however reveal a non-zero but small scattering probability. It is small when compared to nonlinear Compton scattering of Case 1. This expectation of zero scattering probability is a consequence of the assumption [16] that the electron is initially at rest. In our calculations, this is not the case because of the Compton profile of the ground state electron. The effect of the Compton profile on the nonlinear Compton scattering probability can be studied by examining the scattering from a free electron modeled by a Gaussian wave packet. Changing the spatial width of the initial free electron wave packet ($\psi_0^{(0)}$) along the z-direction is found to change the scattering probability for nonlinear Compton scattering for Case 4. This confirms that the non-zero scattering probability for nonlinear Compton scattering for Case 4 is the effect of the Compton profile.

4.4 Conclusion and summary

The interference between Compton scattering and nonlinear Compton scattering from two incoming fields was examined. To understand the phase shifts involved, a first order perturbative approach in the incoming classical field was used to describe Compton scattering and a second order perturbative approach was used to describe nonlinear Compton scattering. The regimes where the approach is valid was analyzed by comparing it with a previously developed approach that was non-perturbative in the classical field [66]. For interference to exist, the scattered wave vector and polarization of the scattered wave for both Compton scattering and nonlinear Compton scattering have to be the same.

When both Compton scattering and nonlinear Compton scattering pertain to Case 1, the results of the numerical calculation shows that the phase shift between Compton scattering and nonlinear Compton scattering was either 0 or $\boldsymbol{\pi}$, switching between the two, every time

the scattering angle crosses a zero in the differential cross section of Compton or nonlinear Compton scattering [16]. A similar behaviour for the intrinsic phase difference is found for Case 1 - Case 3 interference.

For both Case 3 - Case 1 interference and Case 3 - Case 3 interference, it was found that the scattered wave functions for Compton and nonlinear Compton scattering were orthogonal to each other. Therefore, no interference was found to exist.

These results can help with two common experimental challenges in nonlinear Compton scattering. First, the interference could be used to detect the small nonlinear Compton scattering signal. Second, the interference could be used to distinguish the Compton scattering noise originating from the second-harmonic of the XFEL and the nonlinear Compton scattering signal from the fundamental harmonic of the XFEL.

5. X-RAY IMAGING OF WAVE-PACKET DYNAMICS

The contents of this chapter were published as Venkatesh, A., &; Robicheaux, F. (2022). Simulations for x-ray imaging of wave-packet dynamics. Physical Review A, **106**, 033125.

5.1 Introduction

Since the discovery of Bragg diffraction [1] and Compton scattering [2] over a century ago, x-rays have been used as a probe at the subatomic scale [76–79]. X-rays generally exhibit a low scattering cross section with matter. Therefore, as x-rays travel through a sample, the likelihood of re-scattering after the first scattering event is minimal, making them a useful probing tool. For decades, the scattering of x-rays from an electron in a stationary state has been used to map the momentum density of the electron, also known as the Compton profile [5, 6, 80, 81]. Such measurements on a system in a stationary state are independent of time. However, measurements on a system described by a wave packet, which is a superposition of stationary states, will generally depend on time. To study the time dynamics of electronic wave packets, one requires pulses that have a pulse duration comparable to the oscillatory timescale of the wave packet. In the last two decades, the advent of x-ray free-electron lasers (XFEL) [7, 82–87] that generate pulses in the femtosecond and now attosecond timescales has made this possible. Pump-probe experiments at the attosecond timescale outside the x-ray regime have been previously shown to be quite effective in studying both atomic and molecular wave packets [88–90]. The measurement of time-dependent electron density in molecules can be used to construct molecular movies that offer insight into molecular processes such as bond formation and breaking [19–23].

While x-ray scattering from an electronic stationary state can be used to access the momentum density of the electron, the results for x-ray scattering from a wave packet was shown to have non-trivial dependence on the instantaneous charge density of the electron [24]. In 2012, Dixit et al. [24] showed that when x-rays scatter from an electron in a wave packet state, the incident x-ray field can inelastically scatter, causing transitions from the wave packet state to several final states which depend on the bandwidth of the x-ray pulse. This leads to scattering patterns that deviate substantially from the Fourier transform of the instanta-

neous charge density of the wave packet. Some of the works that have followed Ref. [24] have offered alternative techniques to extract information about the instantaneous charge density of the wave packet [91–93]. For instance, in Ref. [91], Dixit et al. describe a phase contrast imaging technique by examining the interference between the incident and scattered field to obtain the Laplacian of the projected instantaneous charge density. However, this approach requires the placement of detectors in the near field regime which may be experimentally challenging. Recently, Grosser et al. [93] showed that using inelastic Compton scattering, one can achieve x-ray imaging of electron wave packet dynamics provided the scattered electron ends up in a continuum state.

It should be noted that theoretical descriptions of time-resolved x-ray scattering have existed prior to Ref. [24] and the first fully-quantized description of this problem can be attributed to Henriksen and Møller [94]. A detailed overview of the history of the theoretical descriptions can be found in Ref. [95]. In this paper, we derive the double differential scattering probability for x-rays to scatter from an electron in a non-stationary state into a specified final state (or states) resulting in an expression which is related to the ones in Ref. [24, 94–96]. We show that if the final state of the electron after scattering can be detected, it is possible to obtain meaningful information about the dynamics of the electronic wave packet. The scattering profile is shown to reveal the modulus square of the Fourier transform of the instantaneous transition charge density of the electron.

The paper is organized in the following manner: In Sec. 5.2, the double differential scattering probability for x-ray scattering from an electron wave packet is derived and the expression is tailored for the special case of an electron wave packet made of two eigenstates. In Sec. 5.3, the imaging technique is illustrated using several examples. In Sec. 5.4, the conclusions and a summary of the paper are presented.

Unless otherwise stated, atomic units will be used throughout this work.

5.2 Methods and modeling

5.2.1 Deriving the double differential scattering probability

The approach we use to model x-ray scattering from electrons involves treating the incoming field classically and quantizing the outgoing field [16]. Since the problem is non-relativistic for the parameter regime explored, a time-dependent Schrödinger equation approach is adequate. One-photon scattering processes in the parameter regime studied in this paper were shown in Ref. [97] to be adequately described by the first order perturbative treatment of the incoming field. For a complete description of this approach and its validity, see Ref. [97]. Using this approach, the scattering probability amplitude for the process $\psi^{(1)}_{\boldsymbol{k},\boldsymbol{\epsilon}}$ can be obtained from the following equation:

$$\begin{aligned} \mathrm{i}\frac{\partial \psi^{(1)}_{\boldsymbol{k},\boldsymbol{\epsilon}}}{\partial t} - \hat{H}_a \psi^{(1)}_{\boldsymbol{k},\boldsymbol{\epsilon}} = & \sqrt{\frac{2\pi}{V\omega_k}} \mathrm{e}^{-\mathrm{i}\boldsymbol{k}\cdot\boldsymbol{r}} \mathrm{e}^{\mathrm{i}\omega_k t} \\ & \times \boldsymbol{\epsilon}^* \cdot (\hat{\boldsymbol{P}}\ \psi^{(0)}_1 + \boldsymbol{A_C}\ \psi^{(0)}_0)\ W(t) \\ & + (\boldsymbol{A_C}\cdot\hat{\boldsymbol{P}})\psi^{(1)}_0. \end{aligned} \tag{5.1}$$

The quantity $\psi^{(\mathrm{j})}_{\mathrm{i}}$ refers to the scattering probability amplitude for a process that is of order i in the incoming classical field and order j in the outgoing quantized field. Note that the quantity $\psi^{(1)}_{\boldsymbol{k},\boldsymbol{\epsilon}}$ in Eq. (5.1) corresponds to $\psi^{(1)}_1$ in this notation [97]. In Eq. (5.1), $\hat{H}_a$ is the Hamiltonian for an electron in the absence of the incident x-ray field, V is the quantization volume, and $\boldsymbol{k}$ and ω_k are the scattered photon momentum and angular frequency respectively. ϵ denotes the scattered photon polarization. Here, $\boldsymbol{k}\cdot\boldsymbol{\epsilon} = 0$ and $\omega_k = |\boldsymbol{k}|c$ with c being the speed of light in vacuum ($\sim$137.036 a.u.). $\hat{\boldsymbol{P}}$ is the canonical momentum operator for the electron, $\boldsymbol{A_C}$ is the vector potential for the classical incoming field, $\boldsymbol{r}$ refers to the position vector associated with the electron and t refers to time. $W(t)$ is a windowing function which turns the source terms on only for the duration of the incident x-ray pulse. The final results are independent of the choice of the windowing function provided it is sufficiently smooth. [66, 97]

For the parameter regime explored, the only source term in Eq. (5.1) that contributes to the scattering probability is the Compton scattering term $\boldsymbol{A_C}\psi_0^{(0)}$ [97]. This term is sometimes referred to as the off-resonant contribution in x-ray scattering [92, 98] and this step is analogous to neglecting the dispersive correction term in Ref. [24]. The time dependence of $\psi_0^{(0)}$ is dictated by the time-dependent Schrödinger equation with the field-free Hamiltonian $\hat{H}_a$. The vector potential of the incoming pulse $\boldsymbol{A}_C$ is chosen to be the following:

$$\begin{aligned}\boldsymbol{A}_C =& \frac{E}{\omega_{in}} \cos\left[(\omega_{in}t - \boldsymbol{k_{in}}\cdot\boldsymbol{r})\right] \\ &\times \exp\left[\frac{(-(2\ln 2)(t-\frac{\hat{\boldsymbol{k}}_{\boldsymbol{in}}\cdot\boldsymbol{r}}{c})^2)}{t_{wid}^2}\right]\boldsymbol{\epsilon_{in}},\end{aligned} \tag{5.2}$$

where E, ω_{in}, $\boldsymbol{k_{in}}$, t_{wid}, and $\boldsymbol{\epsilon_{in}}$ refer to the incoming electric field amplitude, angular frequency, momentum, the full width at half maximum (FWHM) of the pulse intensity, and polarization of the incoming field respectively. The interaction between the electron and the incident x-ray field is modelled by considering the full space and time dependence of the vector potential because in the studied parameter regime the dipole approximation has limitations [99]. Using Eq. (5.2) and applying the rotating-wave approximation to Eq. (5.1) yields

$$\begin{aligned}\mathrm{i}\frac{\partial\psi^{(1)}_{\boldsymbol{k},\boldsymbol{\epsilon}}}{\partial t} - \hat{H}_a\psi^{(1)}_{\boldsymbol{k},\boldsymbol{\epsilon}} =& \sqrt{\frac{2\pi}{V\omega_k}}\frac{1}{2}\frac{E}{\omega_{in}}\boldsymbol{\epsilon}^*\cdot\boldsymbol{\epsilon}_{in} \\ &\times\exp\left[\frac{(-(2\ln 2)(t-\frac{\hat{\boldsymbol{k}}_{\boldsymbol{in}}\cdot\boldsymbol{r}}{c})^2)}{t_{wid}^2}\right] \\ &\times \mathrm{e}^{\mathrm{i}(\boldsymbol{k_{in}}-\boldsymbol{k})\cdot\boldsymbol{r}}\mathrm{e}^{\mathrm{i}(\omega_k-\omega_{in})t}\ \psi_0^{(0)}.\end{aligned} \tag{5.3}$$

The scattering probability amplitude in the bra-ket notation can be expanded in an eigenbasis of electronic bound states and continuum states of the field-free Hamiltonian $\hat{H}_a$:

$$|\psi^{(1)}_{\boldsymbol{k},\boldsymbol{\epsilon}}(t)\rangle = \sum_n C_{n,\boldsymbol{k}\boldsymbol{\epsilon}}(t)\mathrm{e}^{-\mathrm{i}E_n t}\,|\psi_n\rangle\,. \tag{5.4}$$

Here $\{n\}$ includes the set of all bound and continuum states and E_n denotes the corresponding eigenenergies.

Substituting Eq. (5.4) in Eq. (5.3), one obtains the following expression for $C_{n,\boldsymbol{k}\boldsymbol{\epsilon}}$ in the bra-ket notation after integrating over $t \in (-\infty, \infty)$,

$$\begin{aligned}\lim_{t\to\infty} C_{n,\boldsymbol{k}\boldsymbol{\epsilon}}(t) = &-\mathrm{i}\sqrt{\frac{2\pi}{V\omega_k}}\frac{1}{2}\frac{E}{\omega_{in}}\boldsymbol{\epsilon}^*\cdot\boldsymbol{\epsilon}_{in}\int_{-\infty}^{\infty} dt\,\langle\psi_n|\,\mathrm{e}^{\mathrm{i}E_n t} \\ &\times\exp\left[\frac{(-(2\ln 2)(t-\frac{\hat{\boldsymbol{k}}_{\boldsymbol{in}}\cdot\boldsymbol{r}}{c})^2)}{t_{wid}^2}\right] \\ &\times\mathrm{e}^{\mathrm{i}(\boldsymbol{k}_{\boldsymbol{in}}-\boldsymbol{k})\cdot\boldsymbol{r}}\mathrm{e}^{\mathrm{i}(\omega_k-\omega_{in})t}\;\;|\psi_0^{(0)}\rangle\,.\end{aligned} \tag{5.5}$$

In this paper, the initial state of the electron ($|\psi_0^{(0)}\rangle$) is described by a wave packet. The wave packet can be expanded in the same basis as Eq. (5.4),

$$|\psi_0^{(0)}(t)\rangle = \sum_{n''} a_{n''}\;\mathrm{e}^{-\mathrm{i}E_{n''}t}\,|\psi_{n''}\rangle\,. \tag{5.6}$$

Here, $a_{n''}$ is the probability amplitude associated with state $|\psi_{n''}\rangle$ at $t = 0$. The envelope function of the incoming classical field [Eq. (5.2)] can be approximated as a pure Gaussian since $\hat{\boldsymbol{k}}_{\boldsymbol{in}}\cdot\boldsymbol{r}/c << t_{wid}$. Then, Eq. (5.5) after integration over time is

$$\begin{aligned}\lim_{t\to\infty} C_{n,\boldsymbol{k}\boldsymbol{\epsilon}}(t) = &-\mathrm{i}\sqrt{\frac{2\pi}{V\omega_k}}\frac{1}{2}\frac{E}{\omega_{in}}t_{wid}\sqrt{\frac{\pi}{2\ln 2}}\boldsymbol{\epsilon}^*\cdot\boldsymbol{\epsilon}_{in} \\ &\times\sum_{n''} a_{n''}\mathrm{e}^{-\left(E_n-E_{n''}+\omega_k-\omega_{in}\right)^2\frac{t_{wid}^2}{8\ln 2}} \\ &\times\langle\psi_n|\;\;\mathrm{e}^{\mathrm{i}(\boldsymbol{k}_{\boldsymbol{in}}-\boldsymbol{k})\cdot\boldsymbol{r}}\;\;|\psi_{n''}\rangle\,.\end{aligned} \tag{5.7}$$

Given that the scattered electron is in the state $|\psi_f\rangle$, the double differential scattering probability is given by the modulus square of the corresponding scattering probability amplitude $C_{f,\boldsymbol{k}\boldsymbol{\epsilon}}$.

$$\begin{aligned}\frac{\partial^2 P_f(\boldsymbol{Q})}{\partial\Omega\ \partial\omega_k} =& \frac{2\pi}{V\omega_k}\frac{1}{4}\frac{E^2}{\omega_{in}^2}t_{wid}^2\ \frac{\pi}{2\ln 2}|\boldsymbol{\epsilon}^*\cdot\boldsymbol{\epsilon}_{in}|^2 \\ &\times\sum_{n',n''} a_{n'}^* a_{n''}\ \langle\psi_{n'}|\,\mathrm{e}^{-\mathrm{i}\boldsymbol{Q}\cdot\boldsymbol{r}}\,|\psi_f\rangle \\ &\times\mathrm{e}^{-\left[(\epsilon_f-E_{n'})^2+(\epsilon_f-E_{n''})^2\right]\frac{t_{wid}^2}{8\ln 2}} \\ &\times\langle\psi_f|\,\mathrm{e}^{\mathrm{i}\boldsymbol{Q}\cdot\boldsymbol{r}}\,|\psi_{n''}\rangle\,,\end{aligned} \tag{5.8}$$

where $\epsilon_f = E_f + \omega_k - \omega_{in}$ and $\boldsymbol{Q} = \boldsymbol{k}_{in} - \boldsymbol{k}$. Here the quantity E_f denotes the energy of the stationary state $|\psi_f\rangle$

It is useful to examine Eq. (5.8) for the case of a free electron starting in a momentum eigenstate, the quantity inside the summation on the right hand side of Eq. (5.8) is unity only when $|\psi_f\rangle$ is the corresponding momentum eigenstate that is allowed by momentum and energy conservation after the momentum kick from the x-ray photon. In all other cases, the summation results in zero. Therefore, the free electron double differential scattering probability is given by

$$\frac{\partial^2 P_f(\boldsymbol{Q},\boldsymbol{p}_\mathrm{i})}{\partial\Omega\ \partial\omega_k} = \frac{\partial^2 P_\mathrm{e}}{\partial\Omega\ \partial\omega_k}\ \delta(\boldsymbol{p_f}-\boldsymbol{p}_\mathrm{i}-\boldsymbol{Q}), \tag{5.9}$$

where $\boldsymbol{p_f}$ and $\boldsymbol{p}_\mathrm{i}$ are the momentums that correspond to the final and initial electron momentum eigenstates respectively and $\frac{\partial^2 P_\mathrm{e}}{\partial\Omega\ \partial\omega_k}$ is defined as

$$\frac{\partial^2 P_\mathrm{e}}{\partial\Omega\ \partial\omega_k} = \frac{2\pi}{V\omega_k}\frac{1}{4}\frac{E^2}{\omega_{in}^2}t_{wid}^2\ \frac{\pi}{2\ln 2}|\boldsymbol{\epsilon}^*\cdot\boldsymbol{\epsilon}_{in}|^2. \tag{5.10}$$

To understand how Eq. (5.8) describes the wave packet dynamics, recall that the quantity a_n was defined to be the probability amplitude at $t = 0$ and the incident x-ray pulse attained its peak intensity at $t = 0$. For convenience, the peak intensity of the x-ray pulse is now shifted to a later time t_0 (delay time) by carrying out $t \to t - t_0$. Then, the double differential scattering probability for a bound electron as a function of the delay time can be written as

$$\begin{aligned}\frac{\partial^2 P_f(\boldsymbol{Q}, t_0)}{\partial\Omega\ \partial\omega_k} =& \frac{\partial^2 P_e}{\partial\Omega\ \partial\omega_k} \sum_{n',n''} a^*_{n'} a_{n''}\ \mathrm{e}^{\mathrm{i}(E_{n'}-E_{n''})t_0} \\ & \times \langle\psi_{n'}|\ \mathrm{e}^{-\mathrm{i}\boldsymbol{Q}\cdot\boldsymbol{r}}\ |\psi_f\rangle \\ & \times \mathrm{e}^{-\left[(\epsilon_f - E_{n'})^2 + (\epsilon_f - E_{n''})^2\right]\frac{t_{wid}^2}{8\ln 2}} \\ & \times \langle\psi_f|\ \mathrm{e}^{\mathrm{i}\boldsymbol{Q}\cdot\boldsymbol{r}}\ |\psi_{n''}\rangle\ .\end{aligned} \tag{5.11}$$

Note that Eq. (5.11) does not depend explicitly on the electric field amplitude or the polarization of the incoming or outgoing field. The dependence on the polarization and electric field is however implicitly contained in $\frac{\partial^2 P_e}{\partial\Omega\partial\omega_k}$. Therefore, it is convenient to scale Eq. (5.11) by $\frac{\partial^2 P_e}{\partial\Omega\partial\omega_k}$ to obtain the scaled double differential probability. The results from the final expression in Eq. (5.11) has been evaluated and bench marked with the results of the non-perturbative Schrödinger equation from Ref. [66, 97]. They show excellent agreement for the parameter regime discussed in the manuscript thus validating the approximations involved.

While expressions similar to Eq. (5.11) have been derived previously [24, 95, 96], we have included a detailed derivation in this work to provide clarity and to discuss the different stages in the derivation where approximations are used. Equation (5.11) differs from the expression given by Dixit et al. [24] in two aspects. First, instead of the mean energy of the wave packet, the individual energies of the constituent stationary states (E_n) appear. This difference is only introduced towards the end of the derivation in Ref. [24] and is a valid approximation if the x-ray pulse width is much shorter than the oscillation period of the wave packet. Second, instead of a summation over all possible final states for the scattered electron, the final state is selected to be $|\psi_f\rangle$. In Ref. [24] and other previous works [95, 96], it is the summation over all the final scattered electron states that makes it difficult to access the information about the instantaneous charge density of the wave packet. The lack of summation in Eq. (5.11) allows one to extract the Fourier transform of the weighted probability amplitude of the instantaneous wave packet. This is similar to the idea implicit in Grosser et al. [93] where the final state of the electron was assumed to be a plane wave. The approach described in this paper however is not restricted to the case of a continuum

state for the scattered electron but rather on the principle that determining the final state of the electron simultaneously with the scattered photon momentum allows access to the momentum density of the electron wave packet.

5.2.2 Two-state wave packet

While Eq. (5.11) is valid for an arbitrary electronic wave packet, for simplicity we have used wave packets consisting of two eigen states for the derivation and examples below. There is no fundamental requirement for two states. The basic features are unchanged as long as the time scale of the wave packet is longer than that of the incident x-ray pulse.

Let the wave packet consisting of two eigenstates be,

$$|\psi(t_0)\rangle = a_\alpha |\psi_\alpha\rangle + a_\beta e^{i\phi(t_0)} |\psi_\beta\rangle . \tag{5.12}$$

The instantaneous phase $\phi(t_0)$ satisfies $\phi(t_0) = (E_\alpha - E_\beta) * t_0$, where E_α and E_β are the eigenenergies corresponding to the eigenstates $|\psi_\alpha\rangle$ and $|\psi_\beta\rangle$ respectively. For such a wave packet one can then simplify Eq. (5.11) by imposing a condition on the energy of the scattered photons (ω_k). The condition is that the energy difference between scattered and incident xray, $\omega_k - \omega_{in}$, corresponds to the average transition energy between the stationary states in the wave packet and the final state of the electron (ψ_f). Then using Eq. (5.11) the scaled double differential scattering probability can be written as

$$\begin{aligned}\left(\frac{\partial^2 P_f(\boldsymbol{Q}, t_0)}{\partial\Omega\ \partial\omega_k}\right)_{sc} &= e^{\frac{-\Delta E^2 t_{wid}^2}{16 \ln 2}} \\ &\times \left| \int \psi_f^*(\boldsymbol{r})\ \psi(\boldsymbol{r}, t_0) e^{i\boldsymbol{Q}\cdot\boldsymbol{r}} d^3r \right|^2 ,\end{aligned} \tag{5.13}$$

where ΔE is the energy difference between the two stationary states that constitute the wave packet [Eq. (5.12)]. The term $\psi_f(\boldsymbol{r})$ is the probability amplitude in position space of the final state of the electron. The quantity $\psi(\boldsymbol{r}, t_0)$ refers to the instantaneous probability amplitude of the wave packet in the absence of the incident x-ray field. It is evident from Eq. (5.13) that the scaled double differential scattering probability is proportional to the Fourier transform

of the instantaneous wave function of the electron weighted by the electron's final state wave function. Given the constraint on the scattered photon frequency, note that Eq. (5.13) is identical to Eq. (5.11) for a wave packet made of two eigenstates. It is worth pointing out that in some communities [100–103] what we call as the weighted probability amplitude of the instantaneous wave packet in Eq. (5.13), that is $\psi_f^*(\boldsymbol{r})\psi(\boldsymbol{r}, t_0)$, is referred to as the transition charge density [100].

The result in Eq. (5.13) is suitable for the ideal case where the detector resolution is assumed to be much smaller than the bandwidth of the x-ray pulse. Experimentally in cases with limited detector resolution, one might be interested to integrate Eq. (5.13) over a range of scattered photon energies over which the detector is sensitive, to obtain the differential scattering probability. A discussion of the energy-integrated double differential scattering probability and its implications are presented in Sec. 5.3.3.

5.2.3 Convergence

To evaluate the double differential scattering probability, the relevant matrix elements in Eq. (5.11) were calculated numerically on a grid in spherical coordinates. The convergence is determined by calculating the change in the scaled double differential scattering probability. The only convergence parameters that give rise to a measurable difference in the final results for the scaled differential probability are the radial grid spacing and the radial grid size.

For the results in Fig. 5.1, a grid spacing of 0.1 and 0.05 a.u. leads to a difference of 0.81% in the scaled double differential scattering probability. A grid size of 86 a.u. and 121 a.u. leads to difference of 10^{-6} %. For the results in Fig. 5.2, a grid spacing of 0.025 and 0.05 a.u. gives a difference of 0.28 % when the final state is 2s and 0.03 % when the final state is 2p (summed over all m) respectively. The grid size parameters for Fig. 5.2 exhibit the same convergence behaviour as that of Fig. 5.1 for both 2s and 2p final states.

5.3 Applications

For the example calculations below, the wave packet is probed using an x-ray pulse with a mean photon energy of 147 a.u. (4 keV) and a pulse duration (t_{wid}) of 41.34 a.u. (1 fs).

The incoming field is chosen to be propagating in the $\hat{y}$ direction with its polarization in the $\hat{z}$ direction. It should be noted that Eq. (5.11) does not make assumptions whether the system under study consists of atoms or molecules. However for a simple illustration of the method, we choose a wave packet that consist of two eigenstates of hydrogen.

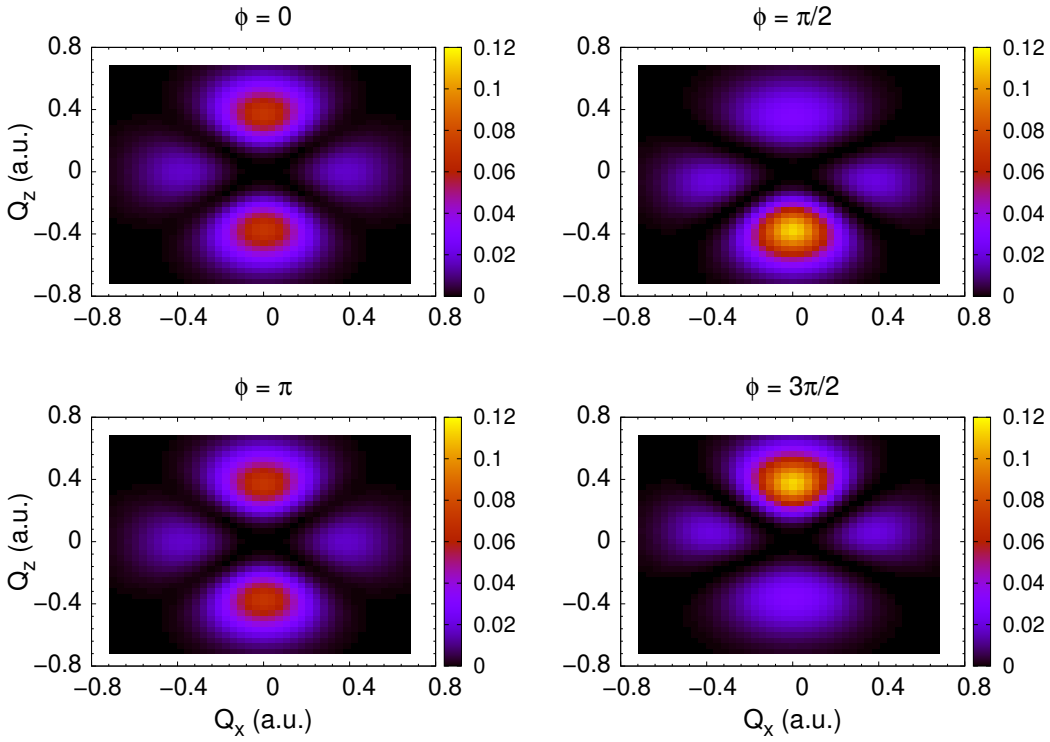

Figure 5.1. The plots show the scaled double differential scattering probability vs momentum transferred to the electron in hydrogen calculated at different propagation times for the wave packet. The initial wave packet consists of equal probabilities of 3d and 4f, m=0 states. The different phase angles specified at the top of each tile correspond to different delay times [Eq. (5.12)] for the probe pulse. The final state of the scattered electron has been chosen to be $2s$. The scaled double differential scattering probability is proportional to the modulus square of the Fourier transform of the instantaneous transition charge density [Eq. (5.13)]. Here, ω_{in} = 147 a.u.(4 keV), t_{wid} = 41.34 a.u. (1 fs).

5.3.1 Fixing the final state up to a given l

To illustrate this method, first we consider the case (Fig. 5.1) when the initial wave packet consist of equal weights of 3d and 4f m = 0 states of hydrogen. There exist several experi-

mental techniques for preparing electronic wave packets (see Ref. [104, 105] and references therein). In this paper, we begin our discussions by assuming that there exists a prepared electronic wave packet. This case corresponds to an instantaneous wave packet [Eq. (5.12)] where $|\psi_\alpha\rangle = |3,2,0\rangle$, $|\psi_\beta\rangle = |4,3,0\rangle$ and $a_\alpha = a_\beta = \frac{1}{\sqrt{2}}$. Here $|n,l,m\rangle$ refers to a state described by the usual atomic quantum numbers n, l, and m respectively.

In Fig. 5.1, the scaled double differential scattering probability is studied as the components of $\boldsymbol{Q}$ (Q_x and Q_z only) are varied independently. It should be noted that the component Q_y is determined for a given Q_x and Q_z because of conservation of energy and momentum. The final state of the electron is chosen to be $2s$. This is an ideal case when a final state with quantum numbers described by n and l can be precisely selected. This ideal case serves to provide a simple conceptual demonstration of the imaging technique. A similar example of an electronic wave packet in hydrogen has been discussed previously in Ref. [24, 96] however in those previous works, the scattering pattern is the result of a summation over all possible final states and not for the case of a given final state. In this work, a numerical approach is used and convergent results have been obtained (see Sec. 5.2.3) for scattering probabilities. Note that it has been shown by Ref. [96] that for the case of hydrogenic wave packets it is possible to obtain analytic solutions if one employs parabolic coordinates.

A qualitative understanding of the scattering profile (Fig. 5.1) can be obtained by looking at the different terms that contribute to the double differential scattering probability.

$$\begin{aligned}\left(\frac{\partial^2 P_f(\boldsymbol{Q},t_0)}{\partial\Omega\ \partial\omega_k}\right)_{sc} = \mathrm{e}^{\frac{-\Delta E^2 t_{wid}^2}{16\ln 2}}\Bigg[&\left|a_\alpha \langle\psi_f|\, \mathrm{e}^{\mathrm{i}\boldsymbol{Q}\cdot\boldsymbol{r}}\, |\psi_\alpha\rangle\right|^2 \\ &+ \left|a_\beta \langle\psi_f|\, \mathrm{e}^{\mathrm{i}\boldsymbol{Q}\cdot\boldsymbol{r}}\, |\psi_\beta\rangle\right|^2 \\ &+ 2Re\Big(a_\alpha^* \langle\psi_f|\, \mathrm{e}^{\mathrm{i}\boldsymbol{Q}\cdot\boldsymbol{r}}\, |\psi_\alpha\rangle^* \\ &\times \mathrm{e}^{\mathrm{i}\phi(t_0)} a_\beta \langle\psi_f|\, \mathrm{e}^{\mathrm{i}\boldsymbol{Q}\cdot\boldsymbol{r}}\, |\psi_\beta\rangle\Big)\Bigg].\end{aligned} \tag{5.14}$$

The phase dependence in Fig. 5.1 originates from the interference terms in Eq.(5.14). It is evident from the interference term in Eq. (5.14) that when a_α and a_β are real, $\phi = 0$ and $\phi = \boldsymbol{\pi}$ cases depend on the real part of $\langle\psi_f|\, \mathrm{e}^{\mathrm{i}\boldsymbol{Q}\cdot\boldsymbol{r}}\, |\psi_\alpha\rangle^* \langle\psi_f|\, \mathrm{e}^{\mathrm{i}\boldsymbol{Q}\cdot\boldsymbol{r}}\, |\psi_\beta\rangle$ and the cases $\phi = \boldsymbol{\pi}/2$

and $\phi = 3\pi/2$ depend on the imaginary part of this product. For the case in Fig. 5.1, from parity arguments $\langle\psi_f|\, e^{i\boldsymbol{Q}\cdot\boldsymbol{r}}\, |\psi_\alpha\rangle$ is real while $\langle\psi_f|\, e^{i\boldsymbol{Q}\cdot\boldsymbol{r}}\, |\psi_\beta\rangle$ is imaginary. This leads to the product of the matrix elements being purely imaginary when $\phi = 0$ and $\phi = \pi$ thus making the $\phi = 0$ and $\phi = \pi$ plots in Fig. 5.1 look identical. The overall shape of the plot (Fig. 5.1) however is largely determined by the non-interfering terms in Eq.(5.14). One can expand the matrix elements that appear in these non-interfering terms, in a series of spherical harmonics $Y_{l'}^{m'}(\hat{\boldsymbol{Q}})$. For example for the parameters in Fig. 5.1, only the coefficients of $Y_2^0(\hat{\boldsymbol{Q}})$ and $Y_3^0(\hat{\boldsymbol{Q}})$ are non-zero because of the rules associated with the addition of angular momentum. The coefficients of $Y_2^0(\hat{\boldsymbol{Q}})$ and $Y_3^0(\hat{\boldsymbol{Q}})$ involve an integral that depends on the radial part of the wave functions present and the spherical Bessel function $j_2(Qr)$ and $j_3(Qr)$ respectively which gives rise to the regions of minimum scattering probability seen in Fig. 5.1. These together give an idea of the shape of the plot in Fig. 5.1.

5.3.2 Selecting the final state based on energy

Experimentally it might be reasonable to expect that the final states of the electron can only be broadly distinguished by their energies. Then, this would result in an incoherent sum of the scaled double differential scattering probability [Eq. (5.13)] over all the nearly-degenerate final states of the electron (sum over all possible l and m for a given n). The results shown in Fig. 5.2 involve a summation over the degenerate final states $2s$, $2p_{-1}$, $2p_0$, and $2p_1$. Note that this is an incoherent sum over $|\psi_f\rangle$ as it involves the sum of the probabilities and not probability amplitudes. This is similar to the sum that appears in Ref. [96], except here the summation is only over the nearly-degenerate final states. It is evident from Fig. 5.2, that such a summation still preserves the dynamical phase information of the instantaneous wave packet.

Since coincidental measurement of the final state of the electron and the momentum of the scattered photon have challenges, we discuss an alternative approach. If the scattered photons that correspond to the resonant transition to a specific final state of the electron can be precisely selected, then it would no longer be required to select the final state of the electron. The idea of using energy-resolved measurements was discussed by Bennet et al. [102]

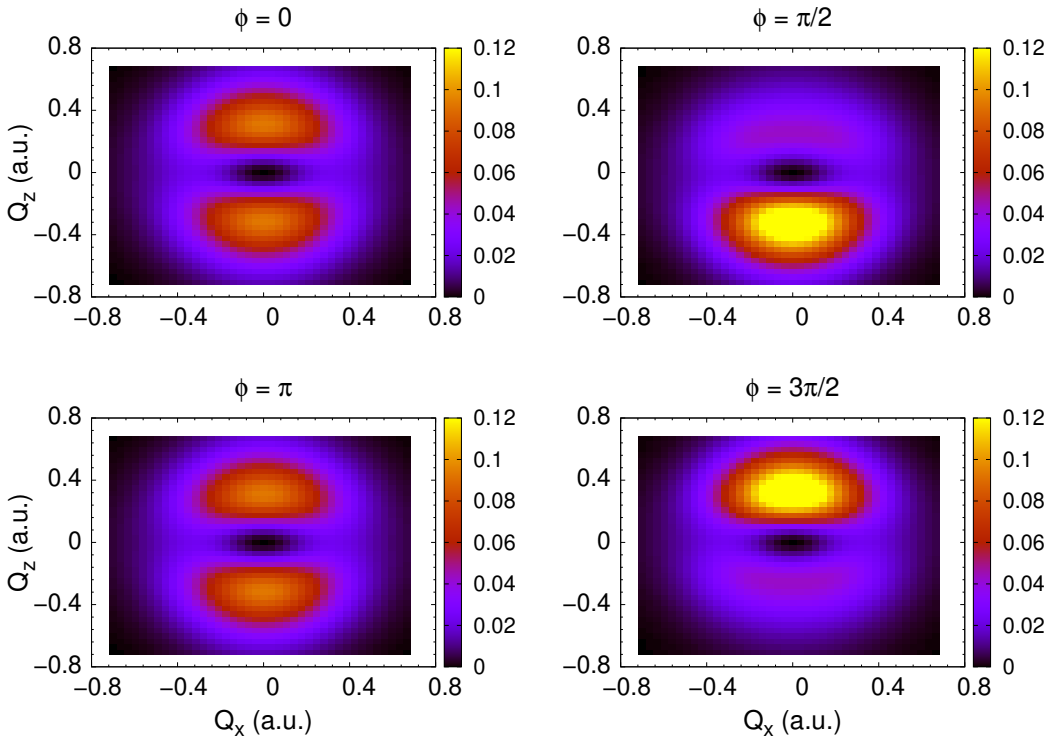

Figure 5.2. The results for the scaled double differential scattering probability vs momentum transferred to the electron calculated at different propagation times for the wave packet. The parameters are the same as that of Fig. 5.1, except here the results are summed over the electron final states $2s$ and $2p$ for all possible values of m. Even when the final state of the scattered electron can only be distinguished broadly based on the energy, dynamical phase information of the wave packet is still preserved.

to broadly distinguish between elastic and inelastic transitions. In this case, we discuss energy-resolved measurements as a way to precisely narrow down the scattered electron to a specific final state(s). As an extreme example, the average of the transition energy between $3d \rightarrow 1s$ and $4f \rightarrow 1s$ is ~ 0.457 a.u. (12.44 eV) and the bandwidth of the incoming x-ray pulse (1 fs) is ~ 0.055 a.u. (1.5 eV). If only those scattered photons with energy between 147.457 ± 0.028 a.u. are selected, then this effectively fixes the final state of the electron to be the $1s$ state. The reason being that the transitions to other final states are unlikely given the limited bandwidth for the given scattered photon energy. This expectation is supported by calculations which show that the scaled double differential scattering probability for

transitions to other final electron states are several orders of magnitude smaller than for the case of $1s$. A detailed discussion of the energy-integrated double differential scattering probability is presented in the next section (Sec. 5.3.3). This approach is especially useful for selecting those final states which have a large energy separation from the wave packet constituent states and other neighbouring eigenstates. This technique can be exploited for several final states by choosing x-ray pulses with appropriate bandwidths. As an example, increasing the bandwidth of the x-ray pulse to 1.5 fs allows one to narrow the final state of the electron to be $2s$ or one of the $2p$ states without the need to detect it.

5.3.3 Integrating the double differential scattering probability over the resolution of detector

In this section, we discuss the effect of integrating the double differential scattering probability over the energy range of the detector. Typically, if the integration is performed over all possible energies, then it is referred to as the differential scattering probability.

Consider Eq. (5.11), for a desired electronic final state $|\psi_f\rangle$, the detector is tuned to detect scattered photons centred around the frequency,

$$\omega_{kd} = \omega_{in} - E_f + E_{wpkt}. \tag{5.15}$$

Here E_{wpkt} refers to the mean energy of the wave packet. The detector resolution is chosen to be δ.

$$\frac{\partial P_f(\boldsymbol{Q}, t_0, \omega_{kd})}{\partial \Omega} = \frac{V}{(2\pi)^3} \int_{\omega_{kd}-\delta}^{\omega_{kd}+\delta} d\omega_k \; \omega_k^2 \; \frac{\partial^2 P_f(\boldsymbol{Q}, t_0)}{\partial \Omega \; \partial \omega_k}. \tag{5.16}$$

It should be noted that in the above expression we have assumed for simplicity that the detector window behaves like a step-function by only detecting the photons in the energy range $\omega_k \in [\omega_{kd} - \delta, \omega_{kd} + \delta]$.

First, the implications of the energy-integrated double differential scattering probability are discussed analytically with approximations. Then the integration is discussed numerically with an example. To proceed with the integration, the Waller-Hartree approximation [106] is

applied to Eq. (5.16) which refers to the assumption, $\omega_k \approx \omega_{in}$ and $\boldsymbol{Q}$ is largely independent of ω_k, Eq. (5.16). This approximation is valid as long as the energy transferred by the x-ray probe photon to the scattered electron is small compared to ω_{in} [96]. This leads to,

$$\begin{aligned}\frac{\partial P_f(\boldsymbol{Q}, t_0, \omega_{kd})}{\partial \Omega} =& \frac{V\ \omega_{\text{in}}^2}{(2\pi)^3} \frac{\partial^2 P_{\text{e}}}{\partial \Omega\ \partial \omega_k} \\ & \times \sum_{n', n''} a^*_{n'} a_{n''}\ \mathrm{e}^{\mathrm{i}(E_{n'} - E_{n''})t_0} \\ & \times \langle \psi_{n'} |\, \mathrm{e}^{-\mathrm{i}\boldsymbol{Q}\cdot\boldsymbol{r}}\, | \psi_f \rangle \langle \psi_f |\, \mathrm{e}^{\mathrm{i}\boldsymbol{Q}\cdot\boldsymbol{r}}\, | \psi_{n''} \rangle \\ & \times \int_{\omega_{kd}-\delta}^{\omega_{kd}+\delta} d\omega_k \mathrm{e}^{-\left[(\epsilon_f - E_{n'})^2 + (\epsilon_f - E_{n''})^2\right] \frac{t_{wid}^2}{8 \ln 2}}\end{aligned} \tag{5.17}$$

Examining Eq. (5.17) for the case of a two-state wave packet, there are two integrals from the non-interference terms and an integral that arises from the interference term.

$$\begin{aligned}\left(\frac{\partial P_f(\boldsymbol{Q}, t_0, \omega_{kd})}{\partial \Omega}\right)_{sc} =& \Bigg[I_1 \left| a_\alpha \langle \psi_f |\, \mathrm{e}^{\mathrm{i}\boldsymbol{Q}\cdot\boldsymbol{r}}\, | \psi_\alpha \rangle \right|^2 \\ & + I_2 \left| a_\beta \langle \psi_f |\, \mathrm{e}^{\mathrm{i}\boldsymbol{Q}\cdot\boldsymbol{r}}\, | \psi_\beta \rangle \right|^2 \\ & + 2 I_3\ Re\Big(a^*_\alpha \langle \psi_f |\, \mathrm{e}^{\mathrm{i}\boldsymbol{Q}\cdot\boldsymbol{r}}\, | \psi_\alpha \rangle^* \\ & \times \mathrm{e}^{\mathrm{i}\phi(t_0)} a_\beta \langle \psi_f |\, \mathrm{e}^{\mathrm{i}\boldsymbol{Q}\cdot\boldsymbol{r}}\, | \psi_\beta \rangle \Big) \Bigg].\end{aligned} \tag{5.18}$$

where I_1 and I_2 are the integrals that arise for the non-interference terms and I_3 is the integral for the interference term. In the left hand side of the above equation [Eq. (5.18)], the energy-integrated double differential scattering probability has been scaled by the free electron expression similar to the earlier convention for double differential scattering probability [Eq. (5.14)].

$$
\begin{aligned}
I_1 &= \int_{\omega_{kd}-\delta}^{\omega_{kd}+\delta} d\omega_k \mathrm{e}^{-\left[(E_f+\omega_k-\omega_{\mathrm{in}}-E_\alpha)^2\right]2\tau} \\
&= \frac{1}{2}\sqrt{\frac{\pi}{2\tau}}\left[erf\left(\sqrt{2\tau}\left[\frac{1}{2}(E_\alpha - E_\beta)+\delta\right]\right)\right. \\
&\quad \left. - erf\left(\sqrt{2\tau}\left[\frac{1}{2}(E_\alpha - E_\beta)-\delta\right]\right)\right].
\end{aligned} \tag{5.19}
$$

$$
\begin{aligned}
I_2 &= \int_{\omega_{kd}-\delta}^{\omega_{kd}+\delta} d\omega_k \mathrm{e}^{-\left[(E_f+\omega_k-\omega_{\mathrm{in}}-E_\beta)^2\right]2\tau} \\
&= \frac{1}{2}\sqrt{\frac{\pi}{2\tau}}\left[erf\left(\sqrt{2\tau}\left[\frac{1}{2}(E_\beta - E_\alpha)+\delta\right]\right)\right. \\
&\quad \left. - erf\left(\sqrt{2\tau}\left[\frac{1}{2}(E_\beta - E_\alpha)-\delta\right]\right)\right].
\end{aligned} \tag{5.20}
$$

$$
\begin{aligned}
I_3 &= \int_{\omega_{kd}-\delta}^{\omega_{kd}+\delta} d\omega_k \exp\left(-\tau\left[(E_f+\omega_k-\omega_{\mathrm{in}}-E_\alpha)^2\right.\right. \\
&\quad \left.\left. +(E_f+\omega_k-\omega_{\mathrm{in}}-E_\beta)^2\right]\right) \\
&= \frac{1}{2}\sqrt{\frac{\pi}{2\tau}}\mathrm{e}^{\frac{-\tau}{2}(E_\beta-E_\alpha)^2}\left[erf\Big(\sqrt{2\tau}\delta\Big)\right. \\
&\quad \left. - erf\Big(-\sqrt{2\tau}\delta\Big)\right].
\end{aligned} \tag{5.21}
$$

In the above equations, we have used $\omega_{kd} = \omega_{\mathrm{in}} - \Big(E_f - \frac{1}{2}(E_\alpha + E_\beta)\Big)$. The quantity $\tau = \frac{t_{wid}^2}{8\ln 2}$.

A comparison of the integrals (see Fig. 5.3) from Eqs. (5.19), (5.20), and (5.21) shows that $I_1 = I_2$. The integrals I_1 and I_3 agree for small detector resolutions (δ) and are nearly equal (to within a few percent) for detector resolutions (δ) that are as high as ten times the bandwidth of the pulse. This implies that the energy -integrated double differential scattering probability [Eq. (5.18)] is still nearly proportional to the double differential scat-

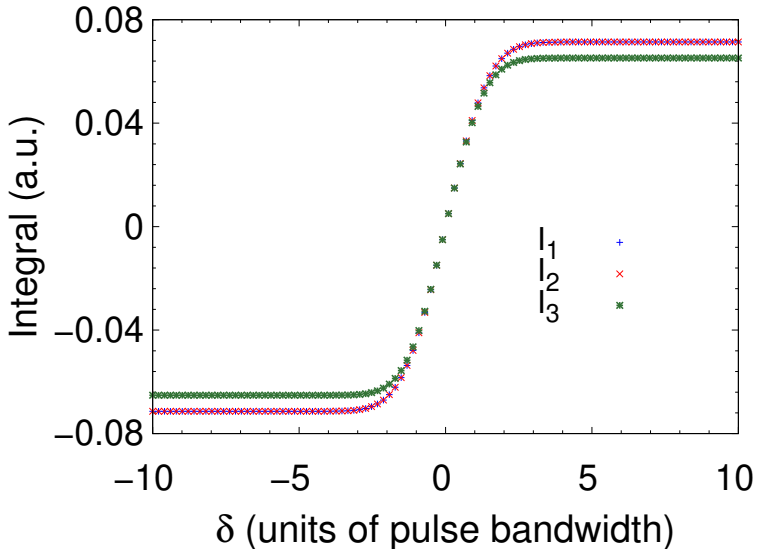

Figure 5.3. The plots show the integrals in Eqs. (5.19) - (5.21) as a function of detector resolution δ which is expressed in multiples of x-ray probe pulse energy bandwidth. It is evident that the integrals that come from integrating the non-interference terms I_1 amd I_2 are equal. Also, the integral I_3 that arises from integrating the interference term of the double differential scattering probability is nearly equal to I_1 even for large detector resolutions (δ). Therefore, the energy-integrated double differential scattering probability is still nearly proportional to the double differential scattering probability. The parameters used are the same as that of Fig. 5.1 except here the final state is chosen to $1s$.

tering probability [Eq. (5.14)]. It should be noted that the effect of integrating the double differential scattering probability can be precisely broken down. That is the non-interference terms reveal the effects of I_1 and I_2 and the interference terms reveal the effects of I_3. Remember that the interference term depends on the probe-delay time [Eq. (5.14)] while the non-interference terms do not. Therefore, the effect of these integrals can be extracted experimentally in principle by examining the interference and the non-interference terms of the energy-integrated double differential scattering probability.

Independent of the analytic discussion, we now calculate the energy-integrated double differential scattering probability [Eq. (5.16)] numerically for the case discussed in Sec. 5.3.2 that is when $|\psi_f\rangle = 1s$. For this case, $\omega_{kd} = 147.457$ a.u. Let $\delta = 0.22$ a.u. (6 eV). This corresponds to a detector resolution that is eight times the bandwidth of the pulse.

To calculate the energy-integrated double differential scattering probability numerically, it is assumed that $\omega_k \approx \omega_{in}$ in the ω_k^2 term on the right-hand side of Eq. (5.16). However unlike in the analytic discussion, for the integration, $\boldsymbol{Q}$ in $\frac{\partial^2 P_f(\boldsymbol{Q},t_0)}{\partial\Omega\ \partial\omega_k}$ is not assumed to be independent of ω_k. Despite this, we find that

$$\frac{\partial P_f(\boldsymbol{Q}, t_0, \omega_{kd}, \delta)}{\partial\Omega} \propto \frac{\partial^2 P_f(\boldsymbol{Q}, t_0)}{\partial\Omega\ \partial\omega_k}. \tag{5.22}$$

Here the double differential scattering probability was evaluated at $\omega_k = \omega_{kd}$. while varying $\boldsymbol{Q}$ and t_0. The deviation from the above proportionality ($\sim 2\%$) is lower than what is expected from Fig. 5.3. The reason is the double differential scattering probability is suppressed by orders of magnitude when ω_k is far from ω_{kd}, so these values don't contribute to the energy-integrated expression as much. Given the proportionality, the double differential scattering probability can be used directly instead of the energy-integrated double differential scattering probability to understand the dynamics of the wave packet.

It should be noted that in the above example, the chosen resolution of the detector (eight times the bandwidth of the pulse) is much less stringent than the typical resolutions used for the same problem previously [24, 96]. For instance in Ref.[96] a detector energy resolution of 0.25 eV which is 1/3 of the pulse energy bandwidth is used. The reason we don't require such high resolutions is because in the examples we discussed, the scattering has more inelastic character than the transitions examined in Ref. [24, 96]. This is an important point, because it is this inelastic behaviour which allows us to select the final state(s). Hence making it possible to interpret the dynamics from the scattering signal which was found to be difficult in Ref. [24]. However, there is a trade-off in that inelastic transitions have a lower overall probability than elastic ones, thus leading to a lower signal strength than in the previous cases. For comparison, the peak of the signal in the case of transition to 1s ($\omega_k = 147.457 \pm 0.22$ a.u.) is more than two orders of magnitude smaller than the peak of the elastic signal ($\omega_k = 147 \pm 0.0092$ a.u.). However, if we consider the same detector resolution as that of Ref. [24, 96], there is a more interesting case. The inelastic transition where the final state is either 2s or 2p ($\omega_k = 147.082 \pm 0.0092$ a.u.) gives a peak signal which is only an order of magnitude smaller than the elastic signal ($\omega_k = 147 \pm 0.0092$ a.u.). Here,

the inelastic transition to 2s or 2p constitutes roughly 90% of the signal. Therefore, in this case the scattering pattern can be interpreted to reveal the instantaneous transition charge density which would have been difficult in the elastic case examined in Refs. [24, 96] and this is achieved by a mere detuning of the detector.

If one needs to access the instantaneous transition charge density from the x-ray scattering profile using Eq. (5.13), either one has to have a detector resolution in the range discussed above or one can resort to coincidental measurement wherein the final state of the scattered electron is fixed and the scattered photon momentum is measured simultaneously. However, the use of coincidental measurements offers much more flexibility with detector resolution. For instance when the final state of the electron is 1s, most of the transition probability is captured by the scattered photons that are within a couple of bandwidths from ω_{kd}. If the scattered photons that are far away in energy from ω_{kd} are detected, in an ideal coincidental measurement only photons that are coming from the electronic transition to final state 1s are counted. Effectively, in the case of coincidental measurements, one has a chance to trade-off accuracy in the detector resolution of the scattered photon energy, with accuracy in the coincidental measurement of the final state of the electron. As a limiting case, one can think of the converse scenario where a highly accurate measurement of the final state of the electron can be substituted for any measurement of the scattered photon energy but note that the direction and the scattered photon count are still required.

So far the discussions have focused around a two-state wave packet but the main results presented in this work are valid for an arbitrary wave packet. In this spirit, we perform calculations for the case of a wave packet consisting of a superposition of three eigenstates. The wave packet was chosen to consist of equal probabilities of $3d$, $4f$ and $5p$. When the final state of the electron is fixed to be 1s, unsurprisingly it was found that Eq. (5.22) still holds true for similar detector resolutions.

5.3.4 Case of a partially known wave packet

As a final example, the case of a wave packet [Eq. (5.12)] which is largely made up of a known eigenstate $|\psi_\beta\rangle$ with $a_\beta \simeq 1$ and a small amount a_α of an unknown eigenstate $|\psi_\alpha\rangle$

is explored. We offer a method using the approach described in Sec. 5.2 to determine the unknown eigenstate.

In the previous examples, the time-dependence of the scattering profile was presented and could be seen to originate from the time-dependent interference terms. In this case, we present the time-independent amplitude of the interference terms which reveals properties of the unknown eigenstate. This quantity can be calculated by examining the terms in Eq. (5.14). The first term can be neglected given that a_α is small. The second term in Eq. (5.14) is a known quantity. The interference (third) term before evaluating the real part can be written as $\chi e^{i(\phi(t_0)-\delta)}$ for some real χ and intrinsic phase δ which depend on the matrix elements. For a given $\boldsymbol{Q}$, the amplitude of the interference term (χ) can be calculated from Eq. (5.14) by varying $\phi(t)$ to obtain the maximum value. Algebraically one can show

$$\begin{aligned}\chi(\boldsymbol{Q}) = 2e^{\frac{-\Delta E^2 t_{wid}^2}{16 \ln 2}} \Big| & a_\alpha \langle \psi_f | \, e^{i\boldsymbol{Q}\cdot\boldsymbol{r}} \, | \psi_\alpha \rangle \\ & \times a_\beta \langle \psi_f | \, e^{i\boldsymbol{Q}\cdot\boldsymbol{r}} \, | \psi_\beta \rangle \Big|.\end{aligned} \tag{5.23}$$

The amplitude of the interference term along with the intrinsic phase (δ) serve as a fingerprint of the eigenstates in the initial wave packet (Figs. 5.4 and 5.5). The amplitude plots alone shown in Fig. 5.4 and Fig. 5.5(a) reveal substantial qualitative differences which can be used to uniquely identify the unknown state up to a given $|m|$ value. To distinguish between the different signs of the magnetic quantum number m for the unknown state, one can examine the plots in Fig. 5.5 describing the dependence of the intrinsic phase (δ) on $\boldsymbol{Q}$.

In principle, experimentally one can estimate the unknown eigenstate using the following steps. First, the energy of the unknown eigenstate can be determined from the time period of oscillation of the wave packet. This can be measured from the x-ray scattering profile by varying the delay time t_0 with no measurement of the final state of the electron required. Recall that the time period of oscillation of the wave packet is $2\pi/|E_\alpha - E_\beta|$. Given the energy of the unknown eigenstate in the wave packet, one can extract the amplitude (χ) of the interference term by making successive measurements of the scaled double differential scattering probability at different delay times t_0 for the wave packet $\psi(\boldsymbol{r}, t_0)$. For a given

$\boldsymbol{Q}$, the delay time that results in the largest magnitude of the interference term can be used to obtain the intrinsic phase. The amplitude (χ) of the interference term and the intrinsic phase (δ) profile (see Figs. 5.4 and 5.5) can then be used to identify the unknown state from a set of eigenstates of the system.

For the examples discussed in Figs. 5.4 and 5.5 the choice for the final state of the electron to be $1s$ may appear to be challenging because of it being the ground state. However, if one follows the approach discussed in Sec. 5.3.2 one needs to measure only the scattered photon momentum precisely to obtain the scattering profiles without any need for coincidental measurements of the final state of the electron .

5.4 Conclusion and summary

Previous research on x-ray scattering from a wave packet revealed that the scattering patterns have a non-trivial dependence on the instantaneous probability density of the wave packet [24]. In this work, we discussed how coincidentally selecting the final state of the scattered electron and the momentum of the scattered photon allows one to extract information about the instantaneous probability density of the wave packet from the scattering signal. The double differential scattering probability from the wave packet was found to be proportional to the modulus square of the Fourier transform of the instantaneous transition charge density. An alternative method which only requires a measurement of the scattered photon momentum without the need to simultaneously measure the final state of the electron was also presented. It was shown to be applicable in cases where the scattered photon energy can be measured precisely enough such that only the transition from the wave packet states to the desired final state(s) occurs. The effect of the energy resolution of the photon detector on the scattering probability was presented. Several examples were discussed with an emphasis on cases that might be more experimentally favourable. Finally, the case of x-ray scattering from a wave packet which is largely (e.g. 95% probability) made of a known eigenstate and has a small amount (5%) of an unknown eigenstate is discussed. The amplitude of the interference term in the double differential scattering probability and its intrinsic phase can be used to identify the unknown eigenstate.

It is worth pointing out that for all of the examples explored in this work, strong incident fields while not necessary (Intensity $\sim 10^{20}$ W/cm^2) can be used to obtain a larger absolute differential scattering probability if desired. From a theoretical perspective, Eq. (5.11) is valid even for x-ray intensities $\sim 10^{20}$ W/cm^2. A more detailed discussion on the validity of the perturbative approach in the strong field regime can be found in Ref. [97]. From an experimental perspective, it should be noted that the currently available XFELs [18, 85–87, 107–110] are capable of generating x-rays in the discussed parameter regime.

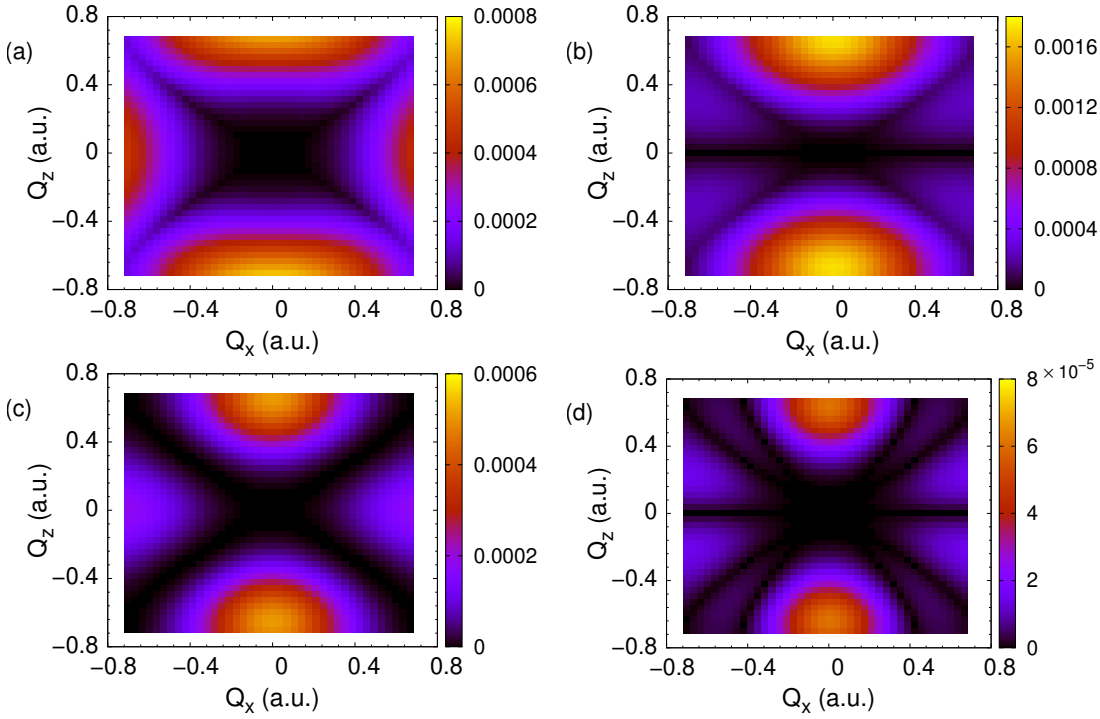

Figure 5.4. The results for the amplitude of the interference term [Eq. (5.23)] vs momentum transferred to the electron. Here the final state of the electron is chosen to be $1s$. The initial wave packet consists of 95% of $|\psi_\beta\rangle = |3d_0\rangle$ and 5% probability of an unknown eigenstate $|\psi_\alpha\rangle$. Different cases for the unknown state $|\psi_\alpha\rangle$ are explored with (a) $4s$ (b) $4p_0$, (c)$4d_0$, and (d) $4f_0$. It is evident that the choice of the initial wave packet leaves a finger print on the x-ray scattering profile. This can be used to uniquely identify the unknown eigenstate in the initial wave packet. The other parameters are the same as Fig. 5.1. A qualitative way to understand the decreasing spread in momentum space from plots (a)-(d) is from the uncertainty principle. The amplitude plotted involves matrix elements using the state $|\psi_\alpha\rangle$ whose uncertainty in position increases from plots (a)-(d) as the orbital angular momentum l increases for a given principal quantum number n.

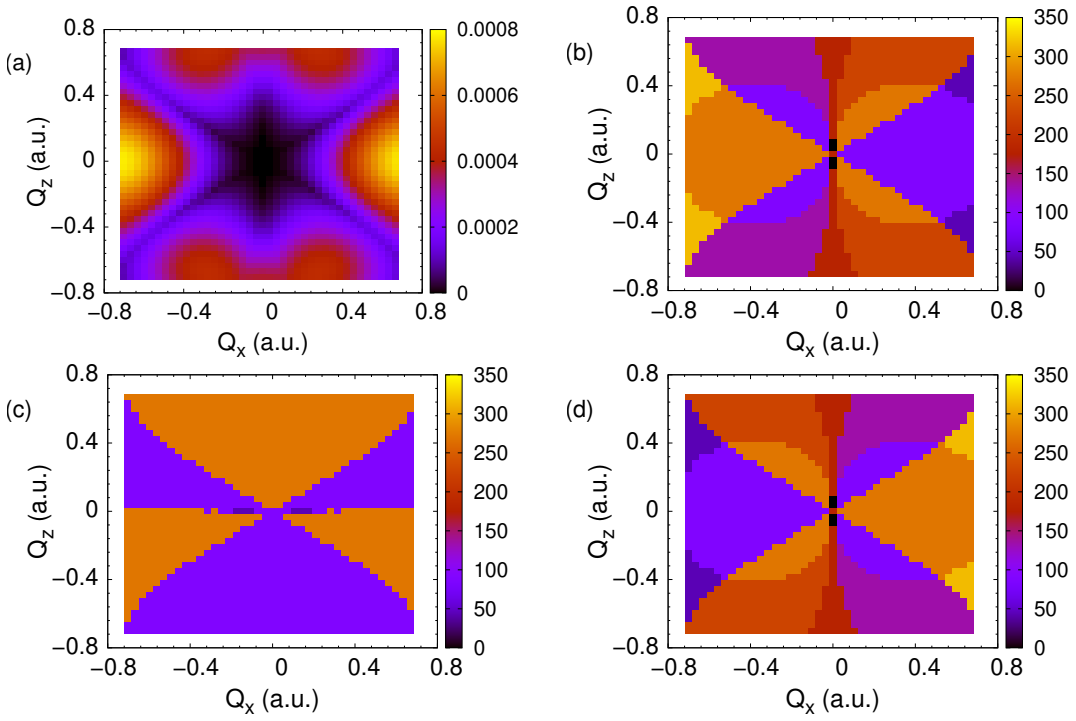

Figure 5.5. The effect of the magnetic quantum number m of the eigenstates in the wave packet on the amplitude and the intrinsic phase of the interference term. Plot (a) contains the amplitude of the interference term [Eq. (5.23)] vs momentum transferred to the electron. The initial wave packet consist of 3d and $4p_1$ states with all the other parameters being the same as Fig. 5.4. Note that the amplitude of the interference term is only sensitive to the absolute value of the magnetic quantum number $|m|$ of the eigenstates in the initial wave packet (compare with Fig. 5.4(b)). Plots (b) - (d) reveal the dependence of the intrinsic phase δ (in degrees) of the interference term on the momentum transferred to the electron. The unknown eigenstate $|\psi_\alpha\rangle$ is chosen to be (b) $4p_{-1}$, (c) $4p_0$, and (d) $4p_1$.

6. EFFECT OF ORIENTATION OF RYDBERG ATOMS ON THEIR COLLISIONAL IONIZATION CROSS SECTION

The contents of this chapter were published as Venkatesh, A., &; Robicheaux, F. (2020). Effect of the orientation of Rydberg atoms on their collisional ionization cross section. Physical Review A, **102**, 032819.

6.1 Introduction

The study of Rydberg atoms has seen considerable progress in the past few decades [25]. The highly excited state of the electrons in these Rydberg atoms gives rise to many interesting properties such as controllable long range interactions [111], a strong response to electric and magnetic fields [112, 113] and classical behavior of valence electrons, all of which have seen considerable analysis [26]. Their manipulable interactions have enabled the study of quantum entanglement effects across multiple atoms and by extension brought about the pursuit for robust qubits built from neutral atoms [27].

The highly excited nature of the valence electron in Rydberg atoms, makes them susceptible to ionization due to either collisions involving Rydberg atoms or interaction with blackbody radiation [28]. In this paper, we focus exclusively on collisions between Rydberg atoms that can lead to one of the atoms becoming ionized through Penning ionization. In Penning ionization, two highly excited atoms with principal quantum number n, collide to give a positive ion, a free electron and the other atom with its valence electron having a principal quantum number n'. If there is no energy transferred to the electrons from the translational kinetic energy of the atoms, it can be shown that $n' < n/\sqrt{2}$ for the process to conserve energy.

Rydberg atoms experience considerable separation when they are prepared because of Rydberg blockade effects [114, 115]. However, collisions between Rydberg atoms can still occur because of their strong interaction. These atoms interact due to van der Waals forces, dipole-dipole forces or other higher multi-pole moments depending on the distance of separation and the nature of the electronic states. Even if these atoms were initially at rest, these interactions could lead to their eventual collisional ionization [29]. More recently,

the effect of van der Waals and dipole-dipole forces on the collisional cross section between Rydberg atoms was examined [30] theoretically and was shown to agree reasonably well with experiment.

The thermal energies of Rydberg atoms can also lead to collisional ionization. The recent work by Fields *et al.* [31] not only provided an idea of the scale and the physics of destruction of Rydberg atoms from collisional ionization but also verified experimentally once again the results of a classical trajectory Monte Carlo approach for collision between two Rydberg atoms. They concluded that these collisional cross sections were significant and comparable to that of collisions between hard spheres of size comparable to the Rydberg orbit. These collisions can also be a source of transition from Rydberg atoms to ultra-cold plasma [116, 117]. Effectively, these collisions can lead to a significant loss of the prepared Rydberg atoms and can be a cause for concern in experiments.

Inspired by the recent results by Fields *et al.* [31], here we try to answer the next relevant question i.e. the effect of orientation of Rydberg atoms on their collisional ionization cross section. Two quantities that should adequately characterize the orientation of the colliding Rydberg atoms are the direction of angular momentum and the direction of the Laplace-Runge-Lenz vector. The research until this point, has been carried out either by assuming some arbitrary choice for the direction and magnitude of angular momentum and the direction of the Laplace-Runge-Lenz vector (see Figs. 6.1 and 6.2) or by averaging the results over them. In this paper we vary these parameters in a systematic way for a couple of orientations to begin understand their impact on the ionization cross section. There is a wide variety of combination of parameters that could be explored; only a few cases are investigated to limit the size of this study. One restriction on the calculation was determined by the experimental arrangement in Ref. [31]: We have the two atoms excited to the same state and interacting through the difference in their thermal, center of mass velocities.

The ionization cross section in general is expected to have some dependence on the magnitude of the angular momentum as it determines the eccentricity of the orbit of the electron. Our investigations of the effect of orientation reveal that for a given magnitude of angular momentum, there can exist a difference of a factor of ~ 2.5 in the ionization cross section between the orientations with the highest and the lowest cross sections. This can

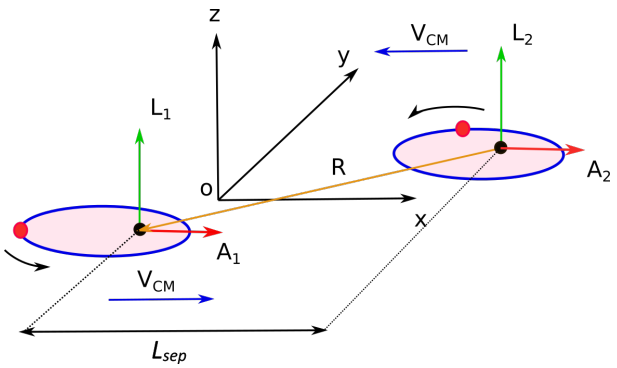

Figure 6.1. Schematic diagram of the two Rydberg atoms for the initial orientation of type-Frisbees. The Red circle on the edge of each ellipse represents an electron and the black circle at the focus of each ellipse represents an ion. The angular momentum vector $\boldsymbol{L}$, the Laplace-Runge-Lenz vector $\boldsymbol{A}$ and $\boldsymbol{V_{CM}}$ are properties of each atom when the separation vector $\boldsymbol{R}$ goes to infinity. To emulate recent experiments [31], all calculations are performed with $\boldsymbol{L_1} = \boldsymbol{L_2}$, $\boldsymbol{A_1} = \boldsymbol{A_2}$ and $\boldsymbol{V_{CM}} = 10^{-4}$ a.u. Note that the orbits of the electrons are in a plane parallel to the x-y plane and L_{sep} is measured along the x-axis.

be relevant because the currently proposed methods [31] to decrease the collisional loss of Rydberg atoms is either to lower the temperature to increase the timescale for collisional destruction or to create the Rydberg atoms in a spaced-out manner, both of which could be difficult to implement. The results in this paper can provide an additional perspective into the physics of collisional ionization with possible insights to minimize it. However, note that our results are not well-suited for application in ultra-cold Rydberg gas experiments such as Ref. [118] as they operate in a parameter regime which is outside the scope of this paper.

Following this, we briefly consider the case of exchange ionization and study its dependence on the magnitude of angular momentum. By exchange ionization we refer to a scenario where one of the approaching Rydberg atoms loses its electron but captures the electron from the other atom leaving the other atom effectively ionized.

One may also be interested in studying the cross sections for a double ionization process in which both the colliding atoms end up being ionized, but the calculations reveal that in order for double ionization to be of significance the velocities have to be much higher and of the same order as the orbital velocity of the electrons [119].

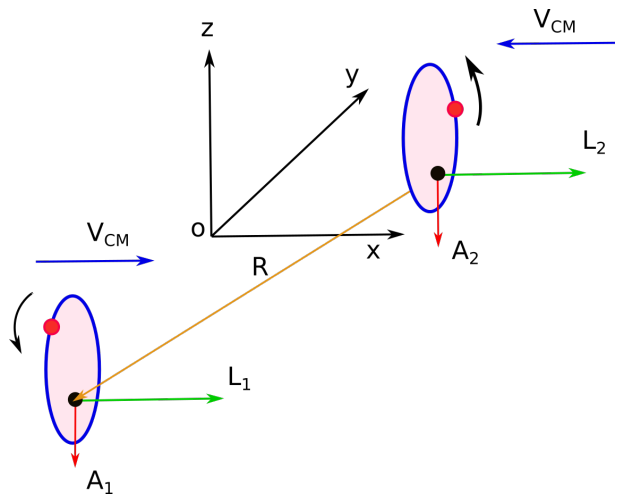

Figure 6.2. Schematic diagram of the two Rydberg atoms for the initial orientation of type-Cymbals. The notation is the same as in Fig. 6.1. Note that the orbits of the electrons are in a plane parallel to the y-z plane.

On the experimental side, Rydberg atoms are usually synthesised with the valence electron being in a state with low orbital angular momentum l. Over the past three decades, there have been several theoretical proposals to obtain high l circular states and high m states which have been followed up by successful experiments [120–127]. Given the experimental progress, we believe that the manipulations proposed in this paper are within reach of current experimental techniques.

This paper is organized as follows. In Sec. 6.2, we describe the approach to analyse collisional ionization. A discussion of the numerical method used and convergence is included. In Sec. 6.3, we apply the method described in Sec. 6.2 to different orientation of the two Rydberg atoms and study its effect on the ionization cross section. We summarize in Sec. 6.4.

Unless otherwise stated, atomic units will be used throughout this paper.

6.2 Methods and modeling

A classical approach is used to model the pair of Rydberg atoms and their scattering. This can be justified in three ways. First, this is reasonable from the classical correspondence principle given the large principal quantum number n of the Rydberg atoms. Second, we

are interested in the ionization cross section with little focus on the nature of the final state of the other electron. Therefore a classical treatment of ionization is desirable as it yields a good approximation of the ionization cross section with an averaging over all possible final states (n,l, and m) of the electrons involved. Third, the final state of each electron will be in energy states which are well above the ones where quantum effects are important. Under these conditions, there is strong experimental support for such a classical approach [31–34].

Each Rydberg atom is modeled as having a nucleus with a unit charge and an electron in a classical Keplerian orbit [128] around the center of mass of the atom with the interaction being purely Coulombic. The initial state of the electron in each atom up to an orbital phase angle, is characterised by its energy, angular momentum and Laplace-Runge-Lenz vector. The energy chosen, corresponds to a Bohr orbit of principal quantum number n. The particular choice of n is not important as the classical results for the collisional cross section scale with n^4, provided the velocity of the atoms is scaled by $1/n$. For our calculations, we choose rubidium-85 with $n = 60$. The orbital angular momentum l is chosen to have a value in the range of (0,n]. The case of $l = n$ corresponds to the special case of Bohr orbits which are ideally circular. Decreasing l below n increases the eccentricity of the orbit. Therefore, the chosen range of angular momentum covers the entire range of eccentricities for the electron's orbit. The direction of the Laplace-Runge-Lenz vector is varied during the course of the calculations to study its effect on the ionization cross section. The initial position and velocity of the electron are determined up to an orbital phase angle which is randomized.

The force exerted by particle j on particle i is given by,

$$\boldsymbol{F}_{\mathrm{ij}} = \frac{q_{\mathrm{i}} q_{\mathrm{j}}}{|\boldsymbol{r}_{\mathrm{i}} - \boldsymbol{r}_{\mathrm{j}}|^3} (\boldsymbol{r}_{\mathrm{i}} - \boldsymbol{r}_{\mathrm{j}}) \tag{6.1}$$

Here, the indices $\mathrm{i}, \mathrm{j} \in \{1,2,3,4\}$ and $\mathrm{i} \neq \mathrm{j}$. The quantity q_{i} refers to the charge of particle i and the quantity r_{i} refers to the position vector of particle i. The equations of motion can then be obtained by solving the two equations.

$$\frac{\mathrm{d}\boldsymbol{v}_{\mathrm{i}}}{\mathrm{d}t} = \frac{\sum_{\mathrm{j}} \boldsymbol{F}_{\mathrm{ij}}}{m_{\mathrm{i}}} \tag{6.2}$$

$$\frac{\mathrm{d}\boldsymbol{r}_{\mathrm{i}}}{\mathrm{d}t} = \boldsymbol{v}_{\mathrm{i}} \tag{6.3}$$

where, the terms $\boldsymbol{v}_{\mathrm{i}}$, $\boldsymbol{r}_{\mathrm{i}}$ and m_{i} denote the velocity, position and mass of the i^{th} particle, respectively.

The two atoms start with a separation of L_{sep}, measured along the x-axis (see Fig. 6.1). The value for L_{sep} is motivated by the minimum L_{sep} required for convergence (refer Sec. 6.2.2) of the cross section. There still remains 2 degrees of freedom for the position of center of mass (CM) of each atom. The y and z coordinates of the center of mass of atom 1 are randomly (uniform) placed inside a disk of radius 0.5 b_{max} centered on the x-axis and is parallel to the y-z plane (refer Sec. 6.2.2 for b_{max}). The CM of atom 2 is positioned such that the total center of mass of the two atoms lies at the origin.

At the initial time, the CM of the first atom is imparted a net velocity in the positive x-direction and the CM of the second atom in the negative x-direction. As the two Rydberg atoms drift towards each other, one of them may ionize depending on the initial conditions. In our calculations, we consider the electron to be ionized if the distance to any of the electrons from the origin of the coordinate system is greater than the initial length of separation between the two Rydberg atoms, L_{sep}.

We define two quantities which serve as a convenient time scale and length scale in the problem. $T_{Ryd} = 2\pi n^3$ is the time period of a Bohr orbit for the chosen principal quantum number n and $R_{Ryd} = n^2$ is the radius of the same Bohr orbit. The aim is to study the ionization cross section as a function of the direction and magnitude of the orbital angular momentum and the direction of the Laplace-Runge-Lenz vector of the electron. In order to determine the cross section, we resort to a Monte Carlo approach. We estimate the cross section by first calculating the probability of ionization from a set of 10,000 Monte Carlo runs by randomly varying the initial orbital phase angle of both the electrons and the impact parameter. The randomized initial conditions form the population of a micro-canonical statistical distribution of the phase space [129] with an additional requirement that the orbital angular momentum of the electrons remain fixed. The initial values for the V_{CM}

of the atoms, the energy of each electron, and the direction and magnitude of the angular momentum of each electron all remain the same during each set.

The orbital phase angle of the electron in the first atom is randomized by allowing the electron to dynamically evolve with time in the absence of the second atom for a random duration between 0 and T_{Ryd}. To randomize the orbital phase angle of the second electron, a small distance which randomly varies between 0 and $V_{CM}T_{Ryd}$ is added to the length of the separation, L_{sep}.

The cross section is typically calculated using the expression $\int 2\pi b P(b) db$ where, the probability of ionization as a function of the impact parameter $P(b)$ is integrated over all possible impact parameters [31]. Here using Monte Carlo sampling described below Eq. (6.3), the total probability of ionization P_{ion}, can be calculated by determining the fraction of total runs that result in ionization and using the expression for the cross section σ:

$$\sigma = \pi b_{max}^2 P_{ion} \tag{6.4}$$

where, b_{max} is the maximum value of the impact parameter that results in ionization. Note that it is convenient to scale the ionization cross section by $\pi(2R_{Ryd})^2$, given that R_{Ryd} is the radius of the Rydberg atom. We define the scaled cross section σ_{scal} as,

$$\sigma_{scal} = \frac{\sigma}{\pi(2R_{Ryd})^2} \tag{6.5}$$

We restrict our discussion to symmetric collisions in which the two colliding Rydberg atoms have the same n value and both electrons have the same orbital angular momentum $\boldsymbol{L}$ and the Laplace-Runge-Lenz vector $\boldsymbol{A}$ [31]. One may refer to Refs. [130, 131] for discussions pertaining to asymmetric collisions. Here, the Laplace-Runge-Lenz vector $\boldsymbol{A}$ is defined as,

$$\boldsymbol{A} = \boldsymbol{p} \times \boldsymbol{L} - \hat{\boldsymbol{r}} \tag{6.6}$$

where $\boldsymbol{p}$ and $\boldsymbol{L}$ indicates the linear momentum and the angular momentum of the electron with respect to the nucleus, respectively. The quantity $\hat{\boldsymbol{r}}$ indicates the unit position vector of the electron measured with the nucleus as the origin. The magnitude of the Laplace-

Runge-Lenz vector is proportional to the eccentricity of the orbit. It should be noted that the magnitude of the Laplace-Runge-Lenz vector of the electron is proportional to the energy in the linear Stark shift and can be accessed by exciting Stark states.

The minor changes required in the procedure to calculate the cross section associated with exchange ionization are discussed in Sec. 6.3.3.

6.2.1 Numerical method

The classical equations of motion [Eqs. (6.2) and (6.3)] are solved numerically using the sixth-order Runge-Kutta (RK6) method with an adaptive step-size [51]. The RK6 method does not conserve the phase space volume. Therefore, the total energy of the system which ideally should be conserved will either increase or decrease with time. For a given time-step, the larger the acceleration of the particle, the larger the error in the velocity and position. At every instance of time, the step size is varied based on the acceleration experienced by the particles, so the error is below an acceptable threshold (see Sec. 6.2.2). For every Monte Carlo run, the aim is to carry out these calculations until an ionization is detected or until the Rydberg atoms pass each other.

The expression in Eq. (6.1) being a purely Coulombic potential can lead to singularities in acceleration during a trajectory. This will cause the adaptive step size algorithm to yield a time-step which can be quite small, thus resulting in runs that may not be feasible computationally. To handle this issue, we override this very small time-step with a threshold value and proceed with the RK6 method directly for the next time-step only. If this process gets repeated, this may lead to a buildup of errors in the total energy with time. If the error in the total energy exceeds 0.1% of the initial total energy, the run is classified as a failed run and not used in the cross section calculations. The number of failed runs is kept well under 3% of the total number of Monte Carlo runs for all the scenarios discussed in this paper, except for the case of $l = 0.2n$ in Fig. 6.6 for which the number of failed runs is closer to 6%. Note that there exists a trade-off between using a purely Coulombic potential and dealing with failed runs or resorting to a softcore Coulombic potential with no failed runs but having to accept less realistic results.

6.2.2 Convergence

Here we briefly discuss the choice of various parameters defined in the preceding section. We find that the probability of ionization P_{ion} depends on the distance of separation between the two atoms L_{sep} for $L_{sep} < 60 \cdot R_{Ryd}$. However, for $L_{sep} > 60 \cdot R_{Ryd}$, the probability of ionization P_{ion} and hence the ionization cross section does not change beyond statistical fluctuations associated with the Monte Carlo approach. Note that this factor of 60 is independent of n and is obtained by numerical experimentation.

We probe the convergence of the cross section with respect to the maximum impact parameter b_{max} by restricting our atoms to be exactly on the circle of radius $0.5 \cdot b_{max}$. Then, we search for a threshold value for the radius b_{max} beyond which strictly no case of ionization occurs from an entire set of runs. Upon varying the radius b_{max}, we find that for $b_{max} > 5 \cdot R_{Ryd}$, no case of ionization is reported for the chosen V_{CM} (refer to Sec. 6.3.2).

For a given successful run, either ionization occurs or it does not. Thus, the Monte Carlo runs form the population of a binomial distribution. For 10,000 runs, the standard deviation in the distribution is under 5% of the mean of the distribution for the case with the lowest cross section.

6.3 Applications

6.3.1 LRL scalar

Before we apply the procedure developed in Sec. 6.2 to study the ionization cross sections, we briefly discuss a quantity which is an approximate constant of motion for large atom separations. For a given set of initial conditions, let the Laplace-Runge-Lenz (LRL) vector for each electron be $\boldsymbol{A_1}$ and $\boldsymbol{A_2}$ respectively.

The Laplace-Runge-Lenz vector is a constant of motion for a central inverse square force [132]. Given the interaction of other charges on a single electron and the motion of the nucleus, the Laplace-Runge-Lenz vector will deviate from its initial value with time. If the atoms are far apart, the Laplace-Runge-Lenz vector precesses with the components of the vector simply oscillating about a mean value. However, as the atoms approach each

other and the interaction strength between the two atoms grows, the components of the Laplace-Runge-Lenz vector will start to deviate from the initial value.

We define a quantity LRL scalar Γ as,

$$\Gamma = \boldsymbol{A}_1 \cdot \boldsymbol{A}_2 - 3(\hat{\boldsymbol{R}} \cdot \boldsymbol{A}_1)(\hat{\boldsymbol{R}} \cdot \boldsymbol{A}_2) \tag{6.7}$$

where, $\hat{\boldsymbol{R}}$ denotes a unit vector from the nucleus of atom 2 to the nucleus of atom 1. An underlying motivation for this definition arises from quantum mechanics. In a quantum mechanical system, this quantity commutes with the Hamiltonian within the n-manifold if the interaction between the two atoms is approximated as a dipole-dipole interaction [133]. Also note that in quantum mechanics, the definition of the Laplace Runge Lenz vector is modified to account for the non-commutation of $\boldsymbol{p}$ and $\boldsymbol{L}$ by using the symmetric form ($\boldsymbol{p} \times \boldsymbol{L}$ - $\boldsymbol{L} \times \boldsymbol{p}$)/2 [134]. The LRL scalar [Eq. (6.7)] is non-zero only for a pair of Rydberg atoms in elliptical orbits since for circular orbits, the Laplace-Runge-Lenz vectors of both atoms vanish.

If two atoms which are at rest are placed relatively close to each other ($L_{sep} = 8 \cdot R_{Ryd}$), we find that the LRL scalar Γ, which resembles the dipole-dipole interaction energy oscillates significantly less than the individual components of the Laplace-Runge-Lenz vector. However, note that this quantity does not remain constant when the atoms are close enough to each other such that the dipole approximation breaks down. The LRL scalar is proportional to the electric dipole-dipole interaction energy between the two Rydberg atoms for a given principal quantum number n as the individual Laplace-Runge-Lenz vectors are proportional to the electric dipole moment of each atom [133]. We examine if the initial LRL scalar of the two atoms when they are far away can be used to effectively characterize their ionization tendencies as they approach each other. We do this (refer to Sec. 6.3.2) by analyzing the correlations between Γ and the ionization cross section of the Rydberg atoms.

It should be noted that Γ changes slightly between Monte Carlo runs. While $\boldsymbol{A_1}$ and $\boldsymbol{A_2}$ remain constant for a given set of runs, the position of each atom and hence $\hat{\boldsymbol{R}}$ changes slightly with every run. This is because the randomization of the initial conditions for the

Monte Carlo approach, involves a change in the impact parameter (not b_{max}) and a small change in the L_{sep} (refer to Sec. 6.2).

6.3.2 Ionization cross section

Here, we investigate how the ionization cross section depends on the magnitude and the direction of the orbital angular momentum of the electron and the direction of the Laplace-Runge-Lenz vector. In our calculations, $V_{CM} = 10^{-4}$ a.u. which corresponds to the rms speed at a temperature of ∼150 K. The chosen V_{CM} is similar to the values observed in the experiment by Fields *et al.* [31]. The results of our calculation are relatively unchanged for a range of velocities between 7 x 10^{-5} to 2 x 10^{-4} a.u which corresponds to the kinetic energies associated with a temperature range of approximately 80-650 K. A more detailed analysis of the dependence of the ionization cross section on the relative velocity of the Rydberg atoms can be found in Ref. [119].

While the trajectories of the particles including the relative motion of the two nuclei are not assumed to be straight lines, the calculations indicate little deviation from the straight-line trajectory for the two nuclei. This is partly because of their large mass. In order for the collision energy of nuclei to become comparable to their interaction energy and their trajectories to deviate from a straight line, the thermal velocities of the atoms should be smaller by about two orders of magnitude from the chosen value ($V_{CM} = 10^{-4}$ a.u.).

Varying the direction of the angular momentum

We explore the effect of varying the direction of the angular momentum of the electrons $\boldsymbol{L_1}$ and $\boldsymbol{L_2}$ on the ionization cross section. Here, we preserve the direction of the Laplace-Runge-Lenz vectors $\boldsymbol{A_1} = \boldsymbol{A_2}$ while we change the direction of the angular momentum vectors, $\boldsymbol{L_1} = \boldsymbol{L_2}$. Based on the discussion in Sec. 6.2, we consider two possible initial orientations, Frisbees (see Fig. 6.1) and Cymbals (see Fig. 6.2).

For the initial orientation of type-Frisbees, the direction of angular momentum can be changed by rotating each atom about their respective Laplace-Runge-Lenz vector and hence

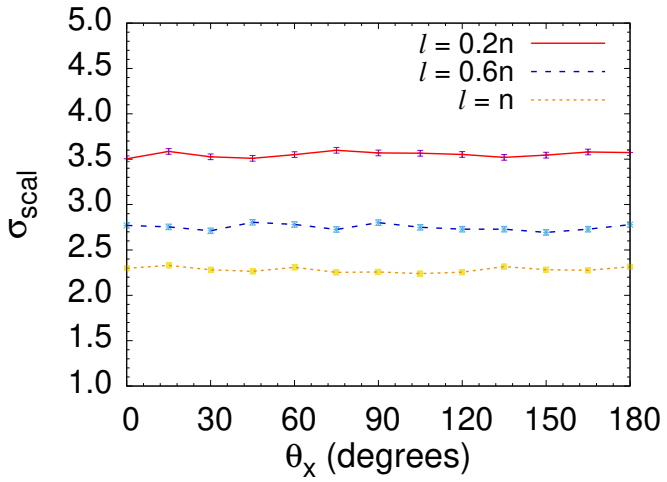

Figure 6.3. Plot of scaled ionization cross section as a function of rotation angle about the x-axis, for the initial orientation of type-Frisbees. Each point is a result of 10,000 Monte Carlo runs. The error bars indicate the standard deviation in the cross section. Here, rotation about the x-axis changes the direction of angular momentum but preserves the direction of the Laplace-Runge-Lenz vectors. The points with the same initial angular momentum l, have been connected to serve as a visual cue. For a given l, the ionization cross section does not change with θ_x. This is expected from rotational symmetry.

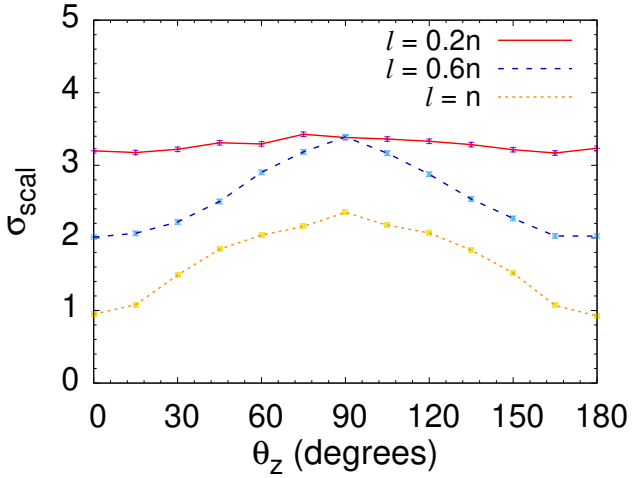

Figure 6.4. Plot of the scaled ionization cross section as a function of rotation angle about the z-axis, for the initial orientation of type-Cymbals. Each point is a result of 10,000 Monte Carlo runs. The error bars indicate the standard deviation in the cross section. Here, rotation about the z-axis changes the direction of angular momentum but preserves the direction of the Laplace-Runge-Lenz vectors. The points with the same initial angular momentum l have been connected to serve as a visual cue.

the x-axis. This ensures that $\boldsymbol{A_1}$ and $\boldsymbol{A_2}$ are invariant. Therefore, the quantity Γ [Eq. (6.7)] remains invariant during this rotation.

For the initial orientation of type-Cymbals, the direction of the angular momentum can be changed by rotation of the atoms about the z-axis. This ensures that $\boldsymbol{A_1}$ and $\boldsymbol{A_2}$ remain the same. Again, Γ remains invariant during the rotation for a given Monte Carlo run but varies slightly between runs for reasons discussed in Sec. 6.3.1.

It should be noted that for type-Frisbees, for the entire range of the rotation angle, the initial orientation of the two atoms remains as type-Frisbees. However, for type-Cymbals, during the rotation about the z-axis, the orientation changes from type-Cymbals to type-Frisbees at an angle of 90°.

For each orientation of the angular momentum, the ionization cross section is calculated using the procedure developed in Sec. 6.2. Given the direction of the Laplace-Runge-Lenz vector, a rotation angle range of 0-180° exhaustively covers all possible relative orientations between the two atoms for the angular momentum. These calculations are performed for different magnitudes of the angular momentum (see Figs. 6.3 and 6.4).

For type-Frisbees (Fig. 6.3), we find that the ionization cross section is independent of the rotation angle about the x-axis for a given angular momentum magnitude, l. This is expected from the rotational symmetry as the angle between the angular momentum vector and $\hat{\boldsymbol{R}}$ remains the same throughout the rotation given the direction of the Laplace Runge Lenz vector (Fig. 6.1). Upon increasing l, we find that the cross section decreases. This indicates that an electron in a circular orbit is more difficult to ionize than an electron in a highly elliptical orbit. This becomes clear if we examine the outer turning point radius r_{out} for elliptical orbits, which is given by [135],

$$\frac{r_{out}}{R_{Ryd}} = 1 + \sqrt{1 - \left(\frac{l}{n}\right)^2}. \tag{6.8}$$

So, for an orbit with $l = 0.2n$ the outer turning point distance from the nucleus is approximately twice as large when compared to a circular orbit ($l = n$) of the same energy (n). Thus making it likely that the electron will venture into regions of stronger field from the other atom.

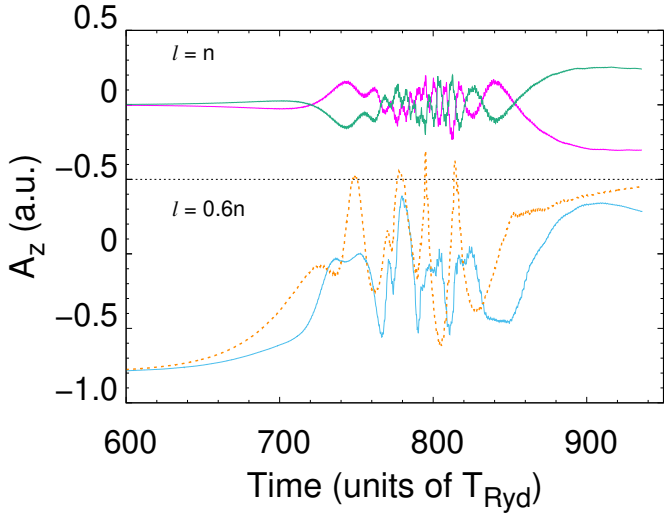

Figure 6.5. Plot of the z-component of the Laplace-Runge-Lenz vector of each electron as a function of time for a typical non-ionizing run, for the initial orientation of type-Cymbals ($\theta_z = 0°$ in Fig. 6.4). The bottom pair of curves is for the case of $l = 0.6n$, with the blue solid and the orange dotted lines representing electron 1 and electron 2 respectively. The top pair of curves is for the case of $l = n$ (circular orbits) with the magenta line (starts at the bottom) and green line (starts at the top) representing electron 1 and electron 2 respectively. Note that, these two lines mirror each other. The black dotted line between the top pair and the bottom pair separates the y-axis of the two plots. From the bottom pair of curves, it is evident that the elliptical case lacks the stabilizing oscillations seen in the circular case.

For type-Cymbals (Fig. 6.4), for small magnitudes of angular momentum we find that the cross section does not appear to change with θ_z. As the l value increases, the cross section peaks at a rotation angle of $\theta_z = 90°$. The physics behind this can be understood in the following manner: Consider the case of two circular ($l = n$) Rydberg atoms of type-Cymbals (Fig. 6.2) approaching each other, the electrons in these atoms tend to push each other to the opposite extremes of their orbits. This results in the atoms becoming more elliptical as they approach each other or in other terms, $\boldsymbol{A_1}$ and $\boldsymbol{A_2}$ start building up from zero in opposite directions. This can help in minimizing the interaction energy, thus lowering the ionization cross section effectively. This is evident from the calculations for a single collisional run (Fig. 6.5) that does not result in an ionization. These calculations show that as the two circular Rydberg atoms of type-Cymbals approach each other their respective Laplace-Runge-Lenz vectors start building up in opposite directions and exhibit oscillatory behavior.

This effect is less likely to occur as you make the orbits elliptical (decrease l). The reason is that if the Laplace-Runge-Lenz vectors were already non-zero and equal to each other in the beginning, as they approach each other it becomes more difficult to get them to orient in opposite directions given the symmetric nature of the two atoms. This is also evident from the calculations for a single collisional run (Fig. 6.5) which shows the difficulty in achieving similar stable oscillatory behavior found in the circular case. The z-component of the Laplace-Runge-Lenz vector has been chosen to illustrate how the non-zero value in the elliptical case hinders this oscillatory behavior. Note that the other components of the Laplace-Runge-Lenz vector exhibit similar behavior for the circular case. In the elliptical case, there is a lack of this type of oscillatory behavior in all three components of the Laplace-Runge-Lenz vector.

For the case of type-Frisbees (Fig. 6.1), this effect will not manifest. The nature of the orientation offers significantly less amount of time for $\boldsymbol{A_1}$ and $\boldsymbol{A_2}$ to gradually buildup in opposite directions. Single collisional run calculations for Rydberg collisions of type-Frisbees consistently show the absence of the anti-parallel oscillatory behavior of $\boldsymbol{A_1}$ and $\boldsymbol{A_2}$ found in the case of type-Cymbals (Fig. 6.5). This effect offers some insight into why ionization

cross section from Fig. 6.4 for type-Cymbals is lower by a factor of $\sim 2-3$ than that for type-Frisbees.

Although a rotation angle of $\theta_z = 90°$ corresponds to a orientation of type-Frisbees, the results from Fig. 6.4 should not be compared to Fig. 6.3. The reason for this is because, in Fig. 6.3, the Laplace-Runge-Lenz vector is chosen to be along the x-axis but the Laplace-Runge-Lenz vector in Fig. 6.4 for $\theta_z = 90°$ is along the negative z-axis. However for the special case of $l = n$, the Laplace-Runge-Lenz vector is zero and a comparison of the two figures at $\theta_z = 90°$ reveals good agreement. In the next section, we discuss cases where the Laplace-Runge-Lenz vector is varied. One may then compare the results of Fig. 6.4 with Fig. 6.6 for the value of $\theta_z = 90°$ in both figures. This comparison shows good agreement.

Varying the LRL scalar

We explore the dependence of the ionization cross section on Γ. We vary Γ by changing the direction of Laplace-Runge-Lenz vectors $\boldsymbol{A_1}$ and $\boldsymbol{A_2}$ but preserving the direction of the angular momentums $\boldsymbol{L_1}$ and $\boldsymbol{L_2}$. We do this by rotating each atom about their respective angular momentum vectors. This is equivalent to rotation about the z-axis and x-axis for the initial orientation of type-Frisbees (Fig. 6.1) and type-Cymbals (Fig. 6.2) respectively. Note that this rotation only changes the LRL scalar for type-Frisbees and not type-Cymbals as the angle between the Laplace-Runge-Lenz vector of each atom and $\hat{\boldsymbol{R}}$ remains relatively unchanged for type-Cymbals.

We calculate the ionization cross section, average initial Γ, and standard deviation in the initial Γ for a given angle of rotation, from a set of Monte Carlo runs. Note that the average Γ and the standard deviation in Γ change with rotation angle and l. Again, we repeat these calculations for different angles of rotation and different magnitudes of the angular momentums $|\boldsymbol{L_1}|$ and $|\boldsymbol{L_2}|$.

Consider the initial configuration of type-Frisbees (see Fig. 6.6), for $l = 0.2n$, the average value of the LRL scalar increases from -1.910 ± 0.005 a.u. at 0° to a maximum value of 0.955 ± 0.005 a.u. at 90°, only to revert to the value of -1.910 ± 0.005 a.u. at 180°. There appears to be a positive correlation between the ionization cross section and the modulus

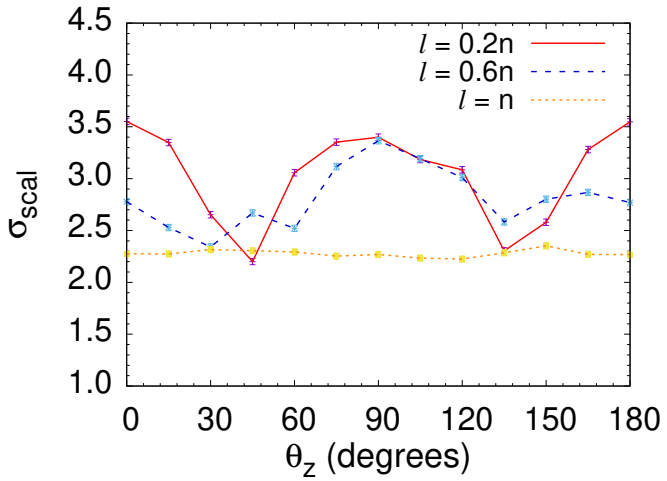

Figure 6.6. Plot of scaled ionization cross section as a function of rotation angle about the z-axis, for the initial orientation of type-Frisbees. Each point is a result of 10,000 Monte Carlo runs. The error bars indicate the standard deviation in the cross section. Here, the rotation about the z-axis changes the direction of Laplace-Runge-Lenz vectors but preserves the direction of angular momentum. This changes the value of the LRL scalar Γ. The points with the same initial angular momentum l, have been connected to serve as a visual cue.

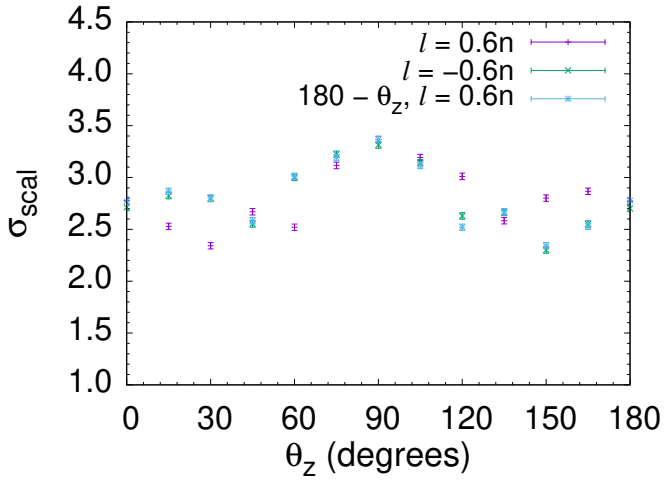

Figure 6.7. Plot of calculation analogous to Fig. 6.6, for the case where the direction of angular momentum has been inverted ($l = -0.6n$). For comparison, the case of $l = 0.6n$ is plotted after reflection about 90°. In simpler terms, for the case of $l = 0.6n$, an angle of 30° in Fig. 6.6 corresponds to an angle of 150° here. A comparison of the two cases $l = -0.6n$ and $180 - \theta_z, l = 0.6n$ reveals very good agreement. This clearly indicates that the direction of angular momentum plays a role in the asymmetry.

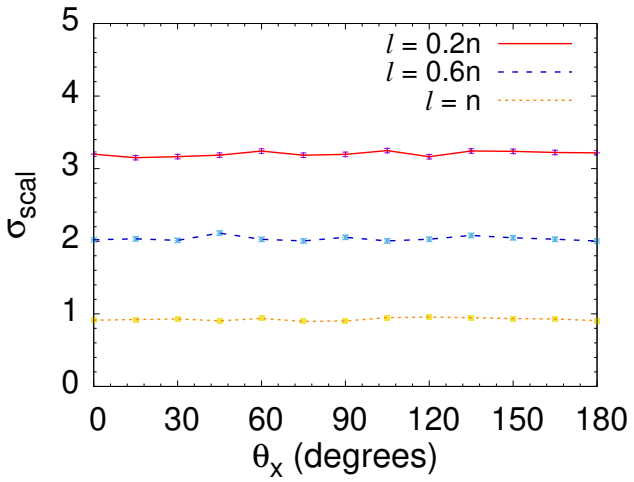

Figure 6.8. Plot of the scaled ionization cross section as a function of rotation angle about the x-axis, for the initial orientation of type-Cymbals. Each point is a result of 10,000 Monte Carlo runs. The error bars indicate the standard deviation in the cross section. Here, the rotation about the x-axis changes the direction of Laplace-Runge-Lenz vectors but preserves the direction of angular momentum. It should be noted that this rotation does not appreciably change the LRL scalar Γ because for this configuration $\hat{\boldsymbol{R}}$ remains largely perpendicular to $\boldsymbol{A_1}$ and $\boldsymbol{A_2}$. The points with the same initial angular momentum l, have been connected to serve as a visual cue.

of the LRL scalar, Γ. The average LRL scalar exhibits similar behavior for other l values, except that the average LRL scalar decreases with an increase in l.

This observed positive correlation should be expected because the quantity LRL scalar Γ is proportional to the electric dipole-dipole interaction energy (refer to Sec. 6.3.1). A large absolute initial value for Γ implies a large interaction energy between the two atoms when they are far apart. If Γ is an adiabatic invariant until the atoms get close to each other (see Sec. 6.3.1), then a large initial interaction energy implies a large interaction energy when they are relatively close and thus consequentially one might expect a large ionization cross section.

An interesting observation from Fig. 6.6 is that there exists an asymmetry about $\theta_z = 90°$ for intermediate values of angular momentum. This is easily noticeable for $l = 0.6n$. Intuitively, one might expect a symmetry because of how the relative orientations of the Laplace-Runge-Lenz vectors between the two atoms remain unchanged for the two rotation angles θ_z and $180 - \theta_z$. A supporting argument for this expectation is the fact that the LRL scalar Γ is found to be symmetric about 90°. However, a careful analysis reveals that this symmetry is broken by the direction of the angular momentum. A calculation identical to the one in Fig. 6.6 for $l = 0.6n$ but with the direction of angular momentum reversed verifies this (see Fig. 6.7). Interestingly, a similar asymmetry was found to exist in ion-Rydberg-atom collisions [136].

For the initial configuration of type-Cymbals, the rotation about the x-axis changes the direction of the Laplace-Runge-Lenz vectors. However, it does not change the value of the LRL scalar Γ. The results from the calculation (see Fig. 6.8) for the ionization cross section indicate that for a given magnitude of angular momentum l, the cross section remains a constant with this rotation. This is expected because of symmetry as the rotation still preserves the relative orientation of the two atoms and is equivalent to merely observing the collision from a different viewing angle. This result is consistent with the earlier observation that the ionization cross section is positively correlated with the modulus of the LRL scalar Γ.

6.3.3 Exchange ionization

Here we focus exclusively on exchange ionization which is distinct from simple ionization. By simple ionization, we refer to those collisions in which the atom that loses the electron finally ends up being ionized after they pass each other. This is different from exchange ionization where, atom 1 (2) initially loses its electron but captures the electron from atom 2 (1) and atom 2 (1) ends up being ionized. Atom 1 (2) however departs with electron 2 (1). Note that the procedure described in Sec. 6.2 counts all possible ionizations including exchange ionizations.

Exchange ionizations can be exclusively counted by running every Monte Carlo run until the Rydberg atoms pass each other and then classifying the ionization that may occur as an exchange ionization if the distance between the nucleus of atom 1 (2) and electron 2 (1) is within $2R_{Ryd}$. This restriction has been chosen by measuring the final distances between the exchanged electron and the nucleus across multiple runs and ensuring that all exchanges are included. We can calculate the exchange ionization cross section from the corresponding probability by using the same equation used to determine the total ionization cross section [Eq. (6.4)].

These calculations reveal the following: for the initial orientation of type-Frisbees with $l = n$, we get a scaled exchange ionization cross section of 1.16 ± 0.02. For reference, the scaled total ionization cross section for the same case is 2.23 ± 0.03. This indicates that exchange ionization contributes to as much as 50% of the total ionizations. The calculations show that the exchange ionization also increases with a decrease in the magnitude of the orbital angular momentum of the electrons analogous to the total ionization cross section. This can be interpreted using the same argument for why circular orbits are more stable (see Sec. 6.3.2). As the orbits become more elliptical their outer turning point distances increase and consequentially they can be more easily captured by the other atom and also are more likely to be the reason for the ionization of the other electron. This is supported by the fact that single collisional run calculations indicate that the capture and the ionization occur relatively at the same time.

While the identical nature of electrons makes it difficult to study exchange ionization experimentally, one way it can be studied is by creating atom 1 with the valence electron in a state of spin-up and atom 2 with the valence electron in a state of spin-down. This way we have effectively labeled the electrons and can in principle track their final states.

6.4 Conclusion and summary

We defined a quantity called the LRL scalar Γ and discussed how the fluctuations in this quantity were much lower than the fluctuations in the individual Laplace-Runge-Lenz vectors $\boldsymbol{A_1}$ and $\boldsymbol{A_2}$ of the electrons. We studied the dependence of the ionization cross section on the direction and the magnitude of the orbital angular momentum of the electron and the direction of the Laplace-Runge-Lenz vectors of the electrons.

These calculations revealed the following: First, the ionization cross sections exhibited positive correlations with the modulus of the LRL scalar [Eq. (6.7)]. The underlying reason is that the electric dipole-dipole interaction energy is proportional to the LRL scalar at large atom separations and therefore the ionization cross section would increase with the interaction. Second, the Rydberg atoms with highly elliptical orbits (small l) had higher ionization cross sections relative to Rydberg atoms with circular orbits ($l = n$) implying that circular orbits were significantly more stable to collisional ionization. Third, as the magnitude of the angular momentum was increased ($l \to n$), the initial configuration of type-Cymbals for the atoms exhibited significantly lower ionization cross sections (lower by a factor of $\sim 2-3$ for $l = n$) than that of type-Frisbees. This was interpreted in terms of the tendency of the Laplace-Runge-Lenz vectors to become anti-parallel as the atoms approach each other.

Finally, exchange ionization was studied and its dependence on the magnitude of angular momentum was found to be similar to that of the total ionization cross section. The calculations indicated that the exchange ionizations contributed to about 50% of the total ionizations.

These results indicate several ways in which the stability of Rydberg atoms against collisional ionization can be significantly improved. The lowest ionization cross section is achieved for the case of circular orbits and when the relative orientation of the two atoms is of type-Cymbals.

7. SUMMARY

This dissertation discussed the investigations into non-relativistic x-ray scattering (Chapters 3, 4 and 5) and Rydberg-Rydberg scattering(Chapter 6).

Chapter 3 described a method to model x-ray scattering from bound electrons. The method was benchmarked by comparing it with the analytical expressions for differential cross section for Compton scattering and nonlinear Compton scattering from a free electron. The investigations using this approach ruled out the bound nature of the electrons being the cause of the anomalous shift in the experiment by Fuchs *et al.* [18]. Three other possible causes for the shift were explored and ruled out to be the cause of this shift. This work was published in Ref. [66].

Chapter 4 analyzed the interference between Compton scattering and nonlinear Compton scattering from a two-color x-ray field. The effect of polarization of the two fields on the interference was also investigated. The intrinsic phase difference between the Compton scattered wave function and nonlinear Compton scattered wave function was found to be 0 or π when interference occurred. This work was published in Ref. [97].

Chapter 5 examined the problem with imaging an electronic wave packet using x-ray scattering. It was shown that if the final state after x-ray scattering from an electron can be determined, then the differential scattering probability is proportional to the modulus square of the weighted Fourier transform of the instantaneous electronic spatial wave function. This work was published in Ref. [137].

Chapter 6 dealt with the collisional ionization of Rydberg atoms. The effect of orientation of Rydberg atoms on their collisional ionization cross section was studied classically. A difference in the ionization cross section of a factor of $\sim$ 2-3 was found between the orientations with the highest and the lowest cross sections. This work was published in Ref. [138].

The approach developed in this work to describe non-relativistic x-ray scattering is fairly general in its scope. It does not assume the electron is free or resides in an atom, molecule, or crystal lattice. The formalism fully captures beyond-dipole effects in the scattering and is non-perturbative in the incident field. The method is also suitable for describing pulse-envelope effects such as strong-field displacement ionization which are sometimes neglected in

theoretical x-ray scattering methods. This approach can be used to describe x-ray scattering with strong laser fields with intensities as high as 10^{22} W/cm^2. In conclusion, the approach described in this work is well suited for ultrafast x-ray scattering in a wide-range of systems using XFELs currently in use.

REFERENCES

[1] W. H. Bragg and W. L. Bragg, "The reflection of x-rays by crystals," *Proceedings of the Royal Society of London. Series A, Containing Papers of a Mathematical and Physical Character*, vol. 88, no. 605, pp. 428–438, 1913.

[2] A. H. Compton, "A quantum theory of the scattering of X-rays by light elements," *Phys. Rev.*, vol. 21, pp. 483–502, 5 May 1923. DOI: 10.1103/PhysRev.21.483. [Online]. Available: https://link.aps.org/doi/10.1103/PhysRev.21.483.

[3] O. Klein and Y. Nishina, "The scattering of light by free electrons according to Dirac's new relativistic dynamics," *Nature*, vol. 122, no. 3072, pp. 398–399, 1928, ISSN: 1476-4687. DOI: 10.1038/122398b0. [Online]. Available: https://doi.org/10.1038/122398b0.

[4] M. Peskin, *An introduction to quantum field theory*. CRC press, 2018.

[5] B. I. Lundqvist and C. Lydén, "Calculated momentum distributions and Compton profiles of interacting conduction electrons in lithium and sodium," *Phys. Rev. B*, vol. 4, pp. 3360–3370, 10 Nov. 1971. DOI: 10.1103/PhysRevB.4.3360. [Online]. Available: https://link.aps.org/doi/10.1103/PhysRevB.4.3360.

[6] P. Eisenberger and P. M. Platzman, "Compton scattering of X rays from bound electrons," *Phys. Rev. A*, vol. 2, pp. 415–423, 2 Aug. 1970. DOI: 10.1103/PhysRevA.2.415. [Online]. Available: https://link.aps.org/doi/10.1103/PhysRevA.2.415.

[7] P. Emma *et al.*, "First lasing and operation of an ångstrom-wavelength free-electron laser," *Nat. Photon.*, vol. 4, no. 9, p. 641, 2010.

[8] T. Ishikawa *et al.*, "A compact X-ray free-electron laser emitting in the sub-ångström region," *Nat. Photon.*, vol. 6, no. 8, p. 540, 2012.

[9] K. Tamasaku *et al.*, "X-ray two-photon absorption competing against single and sequential multiphoton processes," *Nat. Photon.*, vol. 8, no. 4, p. 313, 2014.

[10] G. Doumy *et al.*, "Nonlinear atomic response to intense ultrashort x rays," *Phys. Rev. Lett.*, vol. 106, p. 083 002, 8 Feb. 2011. DOI: 10.1103/PhysRevLett.106.083002. [Online]. Available: https://link.aps.org/doi/10.1103/PhysRevLett.106.083002.

[11] J. G. Eden, "High-order harmonic generation and other intense optical field–matter interactions: Review of recent experimental and theoretical advances," *Progress in Quantum Electronics*, vol. 28, no. 3-4, pp. 197–246, 2004.

[12] K. Motomura *et al.*, "Sequential multiphoton multiple ionization of atomic argon and xenon irradiated by x-ray free-electron laser pulses from SACLA," *J. Phys. B*, vol. 46, no. 16, p. 164 024, Aug. 2013. DOI: 10.1088/0953-4075/46/16/164024. [Online]. Available: https://doi.org/10.1088%5C%2F0953-4075%5C%2F46%5C%2F16%5C%2F164024.

[13] T. G. Blackburn and M. Marklund, "Nonlinear Breit-Wheeler pair creation with bremsstrahlung γ rays," *Plasma Physics and Controlled Fusion*, vol. 60, no. 5, p. 054 009, Mar. 2018. DOI: 10.1088/1361-6587/aab3b4. [Online]. Available: https://doi.org/10.1088%5C%2F1361-6587%5C%2Faab3b4.

[14] C. Harvey, T. Heinzl, and A. Ilderton, "Signatures of high-intensity Compton scattering," *Phys. Rev. A*, vol. 79, p. 063 407, 6 Jun. 2009. DOI: 10.1103/PhysRevA.79.063407. [Online]. Available: https://link.aps.org/doi/10.1103/PhysRevA.79.063407.

[15] V. Dinu and G. Torgrimsson, "Single and double nonlinear Compton scattering," *Phys. Rev. D*, vol. 99, p. 096 018, 9 May 2019. DOI: 10.1103/PhysRevD.99.096018. [Online]. Available: https://link.aps.org/doi/10.1103/PhysRevD.99.096018.

[16] L. S. Brown and T. W. B. Kibble, "Interaction of intense laser beams with electrons," *Phys. Rev.*, vol. 133, A705–A719, 3A Feb. 1964. DOI: 10.1103/PhysRev.133.A705. [Online]. Available: https://link.aps.org/doi/10.1103/PhysRev.133.A705.

[17] C. Bula *et al.*, "Observation of nonlinear effects in Compton scattering," *Phys. Rev. Lett.*, vol. 76, no. 17, p. 3116, Apr. 1996. DOI: 10.1103/PhysRevLett.76.3116. [Online]. Available: https://link.aps.org/doi/10.1103/PhysRevLett.76.3116.

[18] M. Fuchs *et al.*, "Anomalous nonlinear X-ray Compton scattering," *Nat. Phys.*, vol. 11, no. 11, p. 964, 2015. [Online]. Available: https://doi.org/10.1038/nphys3452.

[19] J. Itatani *et al.*, "Tomographic imaging of molecular orbitals," *Nature*, vol. 432, no. 7019, pp. 867–871, 2004.

[20] T. Bredtmann, M. Ivanov, and G. Dixit, "X-ray imaging of chemically active valence electrons during a pericyclic reaction," *Nature communications*, vol. 5, no. 1, pp. 1–7, 2014.

[21] A. Bhattacherjee and S. R. Leone, "Ultrafast x-ray transient absorption spectroscopy of gas-phase photochemical reactions: A new universal probe of photoinduced molecular dynamics," *Accounts of chemical research*, vol. 51, no. 12, pp. 3203–3211, 2018.

[22] K. Bennett, M. Kowalewski, J. R. Rouxel, and S. Mukamel, "Monitoring molecular nonadiabatic dynamics with femtosecond x-ray diffraction," *Proceedings of the National Academy of Sciences*, vol. 115, no. 26, pp. 6538–6547, 2018.

[23] G. Hermann, V. Pohl, G. Dixit, and J. C. Tremblay, "Probing electronic fluxes via time-resolved x-ray scattering," *Physical review letters*, vol. 124, no. 1, p. 013 002, 2020.

[24] G. Dixit, O. Vendrell, and R. Santra, "Imaging electronic quantum motion with light," *Proceedings of the National Academy of Sciences*, vol. 109, no. 29, pp. 11 636–11 640, 2012, ISSN: 0027-8424. DOI: 10.1073/pnas.1202226109. eprint: https://www.pnas.org/content/109/29/11636.full.pdf. [Online]. Available: https://www.pnas.org/content/109/29/11636.

[25] M. P. A. Jones, L. G. Marcassa, and J. P. Shaffer, "Special issue on Rydberg atom physics," *J. Phys. B*, vol. 50, no. 6, p. 060 202, Feb. 2017. DOI: 10.1088/1361-6455/aa5d06. [Online]. Available: https://iopscience.iop.org/article/10.1088/1361-6455/aa5d06.

[26] T. F. Gallagher, *Rydberg Atoms* (Cambridge Monographs on Atomic, Molecular and Chemical Physics). Cambridge University Press, 1994. DOI: 10.1017/CBO9780511524530.

[27] M. Saffman, "Quantum computing with atomic qubits and Rydberg interactions: Progress and challenges," *J. Phys. B*, vol. 49, no. 20, p. 202 001, 2016.

[28] I. Beterov, D. Tretyakov, I. Ryabtsev, V. Entin, A. Ekers, and N. Bezuglov, "Ionization of Rydberg atoms by blackbody radiation," *New J. Phys.*, vol. 11, no. 1, p. 013 052, 2009.

[29] F. Robicheaux, "Ionization due to the interaction between two Rydberg atoms," *J. Phys. B*, vol. 38, no. 2, S333, 2005.

[30] Z. Feng *et al.*, "Analysis of collisional cross sections of Rydberg ns and nd states of ultracold caesium atoms," *Journal of the Physical Society of Japan*, vol. 85, no. 5, p. 054 301, 2016.

[31] G. Fields, F. B. Dunning, S. Yoshida, and J. Burgdörfer, "Destruction of high-n ($n \sim 300$) Rydberg atoms in Rydberg-Rydberg collisions," *Phys. Rev. A*, vol. 99, p. 022 710, 2 Feb. 2019. DOI: 10.1103/PhysRevA.99.022710. [Online]. Available: https://link.aps.org/doi/10.1103/PhysRevA.99.022710.

[32] K. Berkner, W. Graham, R. Pyle, A. Schlachter, J. Stearns, and R. Olson, "Electron-capture and impact-ionisation cross sections for partially stripped iron ions colliding with atomic and molecular hydrogen," *J. Phys. B*, vol. 11, no. 5, p. 875, 1978.

[33] A. Perumal and D. Tripathi, "Unexplained features of capture and ionization for ion–aligned-Rydberg-atom collisions," *Phys. Rev. A*, vol. 64, no. 4, p. 042 709, 2001.

[34] T. Amthor, M. Reetz-Lamour, C. Giese, and M. Weidemüller, "Modeling many-particle mechanical effects of an interacting Rydberg gas," *Phys. Rev. A*, vol. 76, no. 5, p. 054 702, 2007.

[35] A. Venkatesh and F. Robicheaux, "Simulation of nonlinear compton scattering from bound electrons," *Phys. Rev. A*, vol. 101, p. 013 409, 1 Jan. 2020. DOI: 10.1103/PhysRevA.101.013409. [Online]. Available: https://link.aps.org/doi/10.1103/PhysRevA.101.013409.

[36] R. Loudon, *The Quantum Theory of Light*. Oxford University Press, New York, 1983.

[37] C. Cohen-Tannoudji, B. Diu, and L. Franck, *Quantum mechanics. (Mécanique quantique). Vol. 2. (2., rev., enl. ed.)* - Paris Wiley - Hermann XV p, 1978.

[38] J. W. Gibbs, "Fourier's Series," *Nature*, vol. 59, p. 200, 1522 Dec. 1898. DOI: 10.1038/059200b0. [Online]. Available: https://doi.org/10.1038/059200b0.

[39] W. G. Cross and N. F. Ramsey, "The conservation of energy and momentum in Compton scattering," *Phys. Rev.*, vol. 80, pp. 929–936, 6 Dec. 1950. DOI: 10.1103/PhysRev.80.929. [Online]. Available: https://link.aps.org/doi/10.1103/PhysRev.80.929.

[40] Z. Bay, V. P. Henri, and F. McLernon, "Simultaneity in the Compton effect," *Phys. Rev.*, vol. 97, pp. 1710–1712, 6 Mar. 1955. DOI: 10.1103/PhysRev.97.1710. [Online]. Available: https://link.aps.org/doi/10.1103/PhysRev.97.1710.

[41] M. J. Cooper *et al.*, *X-ray Compton scattering*. Oxford University Press on Demand, 2004.

[42] L. Ball and J. Kirk, "Probing pulsar winds using inverse Compton scattering," *Astroparticle Physics*, vol. 12, no. 4, pp. 335–349, 2000. DOI: 10.1016/S0927-6505(99)00112-7. [Online]. Available: https://www.sciencedirect.com/science/article/pii/S0927650599001127.

[43] Vachaspati, "Harmonics in the scattering of light by free electrons," *Phys. Rev.*, vol. 128, pp. 664–666, 2 Oct. 1962. DOI: 10.1103/PhysRev.128.664. [Online]. Available: https://link.aps.org/doi/10.1103/PhysRev.128.664.

[44] D. Krebs, D. A. Reis, and R. Santra, "Time-dependent QED approach to x-ray nonlinear Compton scattering," *Phys. Rev. A*, vol. 99, p. 022 120, 2 Feb. 2019. DOI: 10.1103/PhysRevA.99.022120. [Online]. Available: https://link.aps.org/doi/10.1103/PhysRevA.99.022120.

[45] J. M. Guilarte and M. Mayado, "Qed_2+ 1: The Compton effect," *arXiv preprint hep-th/0009003*, 2000.

[46] Y. Pan and A. Gover, "Spontaneous and stimulated emissions of a preformed quantum free-electron wave function," *Phys. Rev. A*, vol. 99, p. 052 107, 5 May 2019. DOI: 10.1103/PhysRevA.99.052107. [Online]. Available: https://link.aps.org/doi/10.1103/PhysRevA.99.052107.

[47] T. K. Lindblom, M. Førre, E. Lindroth, and S. Selstø, "Semirelativistic Schrödinger equation for relativistic laser-matter interactions," *Phys. Rev. Lett.*, vol. 121, p. 253 202, 25 Dec. 2018. DOI: 10.1103/PhysRevLett.121.253202. [Online]. Available: https://link.aps.org/doi/10.1103/PhysRevLett.121.253202.

[48] M. Førre, "Breakdown of the nonrelativistic approximation in superintense laser-matter interactions," *Phys. Rev. A*, vol. 99, p. 053 410, 5 May 2019. DOI: 10.1103/PhysRevA.99.053410. [Online]. Available: https://link.aps.org/doi/10.1103/PhysRevA.99.053410.

[49] D. J. Bamford, L. E. Jusinski, and W. K. Bischel, "Absolute two-photon absorption and three-photon ionization cross sections for atomic oxygen," *Phys. Rev. A*, vol. 34, pp. 185–198, 1 Jul. 1986. DOI: 10.1103/PhysRevA.34.185. [Online]. Available: https://link.aps.org/doi/10.1103/PhysRevA.34.185.

[50] F. H. Faisal, *Theory of multiphoton processes*. Springer Science & Business Media, 2013.

[51] W. H. Press, S. A. Teukolsky, and W. T. Vetterling, *Numerical Recipes in C: The Art of Scientific Computing, Second Edition*. Cambridge University Press, 1992.

[52] K. LaGattuta, "Laser effects in photoionization: Numerical solution of coupled equations for a three-dimensional Coulomb potential," *JOSA B*, vol. 7, no. 4, pp. 639–646, 1990. DOI: 10.1364/JOSAB.7.000639. [Online]. Available: http://josab.osa.org/abstract.cfm?URI=josab-7-4-639.

[53] S. X. Hu and L. A. Collins, "Intense laser-induced recombination: The inverse above-threshold ionization process," *Phys. Rev. A*, vol. 70, p. 013 407, 1 Jul. 2004. DOI: 10.1103/PhysRevA.70.013407. [Online]. Available: https://link.aps.org/doi/10.1103/PhysRevA.70.013407.

[54] A. Koakowska, M. S. Pindzola, F. Robicheaux, D. R. Schultz, and J. C. Wells, "Excitation and charge transfer in proton-hydrogen collisions," *Phys. Rev. A*, vol. 58, pp. 2872–2880, 4 Oct. 1998. DOI: 10.1103/PhysRevA.58.2872. [Online]. Available: https://link.aps.org/doi/10.1103/PhysRevA.58.2872.

[55] A. Gordon, C. Jirauschek, and F. X. Kärtner, "Numerical solver of the time-dependent Schrödinger equation with Coulomb singularities," *Phys. Rev. A*, vol. 73, p. 042 505, 4 Apr. 2006. DOI: 10.1103/PhysRevA.73.042505. [Online]. Available: https://link.aps.org/doi/10.1103/PhysRevA.73.042505.

[56] P. J. Bergstrom, "Compton scattering of photons from electrons bound in light elements," *Report No. ANL/PHY*, vol. 94, p. 1, Argonne National Laboratory, 1994. [Online]. Available: https://inis.iaea.org/search/search.aspx?orig_q=RN:25053955.

[57] F. Bloch, "Contribution to the theory of the Compton-line," *Phys. Rev.*, vol. 46, pp. 674–687, 8 Oct. 1934. DOI: 10.1103/PhysRev.46.674. [Online]. Available: https://link.aps.org/doi/10.1103/PhysRev.46.674.

[58] P. B. Corkum, "Plasma perspective on strong field multiphoton ionization," *Phys. Rev. Lett.*, vol. 71, pp. 1994–1997, 13 Sep. 1993. DOI: 10.1103/PhysRevLett.71.1994. [Online]. Available: https://link.aps.org/doi/10.1103/PhysRevLett.71.1994.

[59] J. L. Krause, K. J. Schafer, and K. C. Kulander, "High-order harmonic generation from atoms and ions in the high intensity regime," *Phys. Rev. Lett.*, vol. 68, pp. 3535–3538, 24 Jun. 1992. DOI: 10.1103/PhysRevLett.68.3535. [Online]. Available: https://link.aps.org/doi/10.1103/PhysRevLett.68.3535.

[60] A. L'Huillier, K. J. Schafer, and K. C. Kulander, "Theoretical aspects of intense field harmonic generation," *J. Phys. B*, vol. 24, no. 15, pp. 3315–3341, Aug. 1991. DOI: 10.1088/0953-4075/24/15/004. [Online]. Available: https://doi.org/10.1088%5C%2F0953-4075%5C%2F24%5C%2F15%5C%2F004.

[61] M. V. Frolov *et al.*, "Atomic photoionization experiment by harmonic-generation spectroscopy," *Phys. Rev. A*, vol. 93, 031403(R), 3 Mar. 2016. DOI: 10.1103/PhysRevA.93.031403. [Online]. Available: https://link.aps.org/doi/10.1103/PhysRevA.93.031403.

[62] J. Rossbach, J. R. Schneider, and W. Wurth, "10 years of pioneering X-ray science at the free-electron laser FLASH at DESY," *Physics reports*, vol. 808, pp. 1–74, 2019.

[63] L. F. DiMauro, J. Arthur, N. Berrah, J. Bozek, J. N. Galayda, and J. Hastings, "Progress report on the LCLS XFEL at SLAC," *Journal of Physics: Conference Series*, vol. 88, p. 012 058, Nov. 2007. DOI: 10.1088/1742-6596/88/1/012058. [Online]. Available: https://doi.org/10.1088%5C%2F1742-6596%5C%2F88%5C%2F1%5C%2F012058.

[64] C. Bula, K. T. McDonald, E. J. Prebys, C. Bamber, and B. et.al, "Observation of nonlinear effects in Compton scattering," *Phys. Rev. Lett.*, vol. 76, pp. 3116–3119, 17 Apr. 1996. DOI: 10.1103/PhysRevLett.76.3116. [Online]. Available: https://link.aps.org/doi/10.1103/PhysRevLett.76.3116.

[65] D. Krebs, D. A. Reis, and R. Santra, "Time-dependent QED approach to x-ray nonlinear Compton scattering," *Phys. Rev. A*, vol. 99, p. 022 120, 2 Feb. 2019. DOI: 10.1103/PhysRevA.99.022120. [Online]. Available: https://link.aps.org/doi/10.1103/PhysRevA.99.022120.

[66] A. Venkatesh and F. Robicheaux, "Simulation of nonlinear compton scattering from bound electrons," *Phys. Rev. A*, vol. 101, p. 013 409, 1 Jan. 2020. DOI: 10.1103/PhysRevA.101.013409. [Online]. Available: https://link.aps.org/doi/10.1103/PhysRevA.101.013409.

[67] Z. Huang and K.-J. Kim, "Review of x-ray free-electron laser theory," *Phys. Rev. ST Accel. Beams*, vol. 10, p. 034 801, 3 Mar. 2007. DOI: 10.1103/PhysRevSTAB.10.034801. [Online]. Available: https://link.aps.org/doi/10.1103/PhysRevSTAB.10.034801.

[68] A. Tremaine *et al.*, "Experimental characterization of nonlinear harmonic radiation from a visible self-amplified spontaneous emission free-electron laser at saturation," *Phys. Rev. Lett.*, vol. 88, p. 204 801, 20 May 2002. DOI: 10.1103/PhysRevLett.88.204801. [Online]. Available: https://link.aps.org/doi/10.1103/PhysRevLett.88.204801.

[69] Y.-Y. Yin, C. Chen, D. S. Elliott, and A. V. Smith, "Asymmetric photoelectron angular distributions from interfering photoionization processes," *Phys. Rev. Lett.*, vol. 69, pp. 2353–2356, 16 Oct. 1992. DOI: 10.1103/PhysRevLett.69.2353. [Online]. Available: https://link.aps.org/doi/10.1103/PhysRevLett.69.2353.

[70] C. Chen, Y.-Y. Yin, and D. S. Elliott, "Interference between optical transitions," *Phys. Rev. Lett.*, vol. 64, pp. 507–510, 5 Jan. 1990. DOI: 10.1103/PhysRevLett.64.507. [Online]. Available: https://link.aps.org/doi/10.1103/PhysRevLett.64.507.

[71] N. L. Manakov, V. D. Ovsiannikov, and A. F. Starace, "Dc field-induced, phase and polarization control of interference between one- and two-photon ionization amplitudes," *Phys. Rev. Lett.*, vol. 82, pp. 4791–4794, 24 Jun. 1999. DOI: 10.1103/PhysRevLett.82.4791. [Online]. Available: https://link.aps.org/doi/10.1103/PhysRevLett.82.4791.

[72] A. Ilderton, B. King, and S. Tang, "Toward the observation of interference effects in nonlinear Compton scattering," *Phys. Lett. B*, vol. 804, p. 135 410, 2020.

[73] T. N. Wistisen, "Interference effect in nonlinear Compton scattering," *Phys. Rev. D*, vol. 90, no. 12, p. 125 008, 2014.

[74] J. C. Levin *et al.*, "Measurement of the ratio of double-to-single photoionization of helium at 2.8 kev using synchrotron radiation," *Phys. Rev. Lett.*, vol. 67, pp. 968–971, 8 Aug. 1991. DOI: 10.1103/PhysRevLett.67.968. [Online]. Available: https://link.aps.org/doi/10.1103/PhysRevLett.67.968.

[75] J. A. R. Samson, C. H. Greene, and R. J. Bartlett, "Comment on "measurement of the ratio of double-to-single photoionization of helium at 2.8 kev using synchrotron radiation"," *Phys. Rev. Lett.*, vol. 71, pp. 201–201, 1 Jul. 1993. DOI: 10.1103/PhysRevLett.71.201. [Online]. Available: https://link.aps.org/doi/10.1103/PhysRevLett.71.201.

[76] L. J. P. Ament, M. van Veenendaal, T. P. Devereaux, J. P. Hill, and J. van den Brink, "Resonant inelastic x-ray scattering studies of elementary excitations," *Rev. Mod. Phys.*, vol. 83, pp. 705–767, 2 Jun. 2011. DOI: 10.1103/RevModPhys.83.705. [Online]. Available: https://link.aps.org/doi/10.1103/RevModPhys.83.705.

[77] P. Thibault and V. Elser, "X-ray diffraction microscopy," *Annual Review of Condensed Matter Physics*, vol. 1, no. 1, pp. 237–255, 2010. DOI: 10.1146/annurev-conmatphys-070909-104034. eprint: https://doi.org/10.1146/annurev-conmatphys-070909-104034. [Online]. Available: https://doi.org/10.1146/annurev-conmatphys-070909-104034.

[78] C. Bressler and M. Chergui, "Ultrafast x-ray absorption spectroscopy," *Chemical Reviews*, vol. 104, no. 4, pp. 1781–1812, 2004, PMID: 15080712. DOI: 10.1021/cr0206667. eprint: https://doi.org/10.1021/cr0206667. [Online]. Available: https://doi.org/10.1021/cr0206667.

[79] K. A. Nugent, "Coherent methods in the x-ray sciences," *Advances in Physics*, vol. 59, no. 1, pp. 1–99, 2010.

[80] G. Loupias and J. Chomilier, "Electron momentum density and Compton profiles: An accurate check of overlap models," *Zeitschrift für Physik D Atoms, Molecules and Clusters*, vol. 2, no. 4, pp. 297–308, 1986.

[81] B. G. Williams, "The experimental determination of electron momentum densities," *Physica scripta*, vol. 15, no. 2, p. 92, 1977.

[82] C. Bostedt *et al.*, "Linac coherent light source: The first five years," *Rev. Mod. Phys.*, vol. 88, p. 015 007, 1 Mar. 2016. DOI: 10.1103/RevModPhys.88.015007. [Online]. Available: https://link.aps.org/doi/10.1103/RevModPhys.88.015007.

[83] T. Ishikawa *et al.*, "A compact X-ray free-electron laser emitting in the sub-ångström region," *Nat. Photon.*, vol. 6, no. 8, p. 540, 2012.

[84] M. Yabashi, "Status and perspective on the SACLA facility (Conference Presentation)," in *Optics Damage and Materials Processing by EUV/X-ray Radiation VII*, L. Juha, S. Bajt, and S. Guizard, Eds., International Society for Optics and Photonics, vol. 11035, SPIE, 2019. DOI: 10.1117/12.2523624. [Online]. Available: https://doi.org/10.1117/12.2523624.

[85] M. Altarelli, "The european x-ray free-electron laser facility in hamburg," *Nuclear Instruments and Methods in Physics Research Section B: Beam Interactions with Materials and Atoms*, vol. 269, no. 24, pp. 2845–2849, 2011, Proceedings of the 10th European Conference on Accelerators in Applied Research and Technology (ECAART10), ISSN: 0168-583X. DOI: https://doi.org/10.1016/j.nimb.2011.04.034. [Online]. Available: http://www.sciencedirect.com/science/article/pii/S0168583X11003855.

[86] J. Feldhaus *et al.*, "AMO science at the FLASH and european XFEL free-electron laser facilities," *Journal of Physics B: Atomic, Molecular and Optical Physics*, vol. 46, no. 16, p. 164 002, Aug. 2013. DOI: 10.1088/0953-4075/46/16/164002. [Online]. Available: https://doi.org/10.1088%5C%2F0953-4075%5C%2F46%5C%2F16%5C%2F164002.

[87] S. Serkez *et al.*, "Overview of options for generating high-brightness attosecond x-ray pulses at free-electron lasers and applications at the european XFEL," *Journal of Optics*, vol. 20, no. 2, p. 024 005, Jan. 2018. DOI: 10.1088/2040-8986/aa9f4f. [Online]. Available: https://doi.org/10.1088%5C%2F2040-8986%5C%2Faa9f4f.

[88] E. Goulielmakis *et al.*, "Real-time observation of valence electron motion," *Nature*, vol. 466, no. 7307, pp. 739–743, 2010.

[89] G. Sansone *et al.*, "Electron localization following attosecond molecular photoionization," *Nature*, vol. 465, no. 7299, pp. 763–766, 2010.

[90] K. T. Kim *et al.*, "Amplitude and phase reconstruction of electron wave packets for probing ultrafast photoionization dynamics," *Physical review letters*, vol. 108, no. 9, p. 093 001, 2012.

[91] G. Dixit, J. M. Slowik, and R. Santra, "Proposed imaging of the ultrafast electronic motion in samples using x-ray phase contrast," *Phys. Rev. Lett.*, vol. 110, p. 137 403, 13 Mar. 2013. DOI: 10.1103/PhysRevLett.110.137403. [Online]. Available: https://link.aps.org/doi/10.1103/PhysRevLett.110.137403.

[92] G. Dixit, J. M. Slowik, and R. Santra, "Theory of time-resolved nonresonant x-ray scattering for imaging ultrafast coherent electron motion," *Phys. Rev. A*, vol. 89, p. 043 409, 4 Apr. 2014. DOI: 10.1103/PhysRevA.89.043409. [Online]. Available: https://link.aps.org/doi/10.1103/PhysRevA.89.043409.

[93] M. Grosser, J. M. Slowik, and R. Santra, "Attosecond x-ray scattering from a particle-hole wave packet," *Phys. Rev. A*, vol. 95, p. 062 107, 6 Jun. 2017. DOI: 10.1103/PhysRevA.95.062107. [Online]. Available: https://link.aps.org/doi/10.1103/PhysRevA.95.062107.

[94] N. E. Henriksen and K. B. Møller, "On the theory of time-resolved x-ray diffraction," *The Journal of Physical Chemistry B*, vol. 112, no. 2, pp. 558–567, 2008.

[95] M. Simmermacher, A. Moreno Carrascosa, N. E. Henriksen, K. B. Møller, and A. Kirrander, "Theory of ultrafast x-ray scattering by molecules in the gas phase," *J. Chem. Phys.*, vol. 151, no. 17, p. 174 302, 2019.

[96] M. Simmermacher, N. E. Henriksen, and K. B. Møller, "Time-resolved x-ray scattering by electronic wave packets: Analytic solutions to the hydrogen atom," *Phys. Chem. Chem. Phys.*, vol. 19, no. 30, pp. 19 740–19 749, 2017.

[97] A. Venkatesh and F. Robicheaux, "Interference in nonlinear Compton scattering using a Schrödinger-equation approach," *Phys. Rev. A*, vol. 103, p. 013 111, 1 Jan. 2021. DOI: 10.1103/PhysRevA.103.013111. [Online]. Available: https://link.aps.org/doi/10.1103/PhysRevA.103.013111.

[98] M. W. Haverkort, A. Tanaka, L. H. Tjeng, and G. A. Sawatzky, "Nonresonant inelastic x-ray scattering involving excitonic excitations: The examples of nio and coo," *Phys. Rev. Lett.*, vol. 99, p. 257 401, 25 Dec. 2007. DOI: 10.1103/PhysRevLett.99.257401. [Online]. Available: https://link.aps.org/doi/10.1103/PhysRevLett.99.257401.

[99] T. E. Moe and M. Førre, "Ionization of atomic hydrogen by an intense x-ray laser pulse: An ab initio study of the breakdown of the dipole approximation," *Phys. Rev. A*, vol. 97, p. 013 415, 1 Jan. 2018. DOI: 10.1103/PhysRevA.97.013415. [Online]. Available: https://link.aps.org/doi/10.1103/PhysRevA.97.013415.

[100] J. R. Rouxel, M. Kowalewski, K. Bennett, and S. Mukamel, "X-ray sum frequency diffraction for direct imaging of ultrafast electron dynamics," *Phys. Rev. Lett.*, vol. 120, p. 243 902, 24 Jun. 2018. DOI: 10.1103/PhysRevLett.120.243902. [Online]. Available: https://link.aps.org/doi/10.1103/PhysRevLett.120.243902.

[101] M. Kowalewski, K. Bennett, and S. Mukamel, "Monitoring nonadiabatic avoided crossing dynamics in molecules by ultrafast x-ray diffraction," *Structural Dynamics*, vol. 4, no. 5, p. 054 101, 2017.

[102] K. Bennett, J. D. Biggs, Y. Zhang, K. E. Dorfman, and S. Mukamel, "Time-, frequency-, and wavevector-resolved x-ray diffraction from single molecules," *The Journal of chemical physics*, vol. 140, no. 20, p. 204 311, 2014.

[103] D. Cho and S. Mukamel, "Stimulated x-ray raman imaging of conical intersections," *The Journal of Physical Chemistry Letters*, vol. 11, no. 1, pp. 33–39, 2019.

[104] T. C. Weinacht, J. Ahn, and P. H. Bucksbaum, "Measurement of the amplitude and phase of a sculpted Rydberg wave packet," *Phys. Rev. Lett.*, vol. 80, pp. 5508–5511, 25 Jun. 1998. DOI: 10.1103/PhysRevLett.80.5508. [Online]. Available: https://link.aps.org/doi/10.1103/PhysRevLett.80.5508.

[105] T. Weinacht, J. Ahn, and P. H. Bucksbaum, "Controlling the shape of a quantum wavefunction," *Nature*, vol. 397, no. 6716, pp. 233–235, 1999.

[106] I. t. Waller and D. R. Hartree, "On the intensity of total scattering of x-rays," *Proceedings of the Royal Society of London. Series A, Containing Papers of a Mathematical and Physical Character*, vol. 124, no. 793, pp. 119–142, 1929.

[107] *Projected Run 20 LCLS FEL parameters*, https://lcls.slac.stanford.edu/sites/lcls.slac.stanford.edu/files/LCLS-Parameters-Run-20.pdf, Accessed: 2021-12-16. [Online]. Available: https://lcls.slac.stanford.edu/sites/lcls.slac.stanford.edu/files/LCLS-Parameters-Run-20.pdf.

[108] M. Yabashi, H. Tanaka, and T. Ishikawa, "Overview of the SACLA facility," *Journal of Synchrotron Radiation*, vol. 22, no. 3, pp. 477–484, May 2015. DOI: 10.1107/S1600577515004658. [Online]. Available: https://doi.org/10.1107/S1600577515004658.

[109] K. Tono, T. Hara, M. Yabashi, and H. Tanaka, "Multiple-beamline operation of SACLA," *Journal of Synchrotron Radiation*, vol. 26, no. 2, pp. 595–602, Mar. 2019. DOI: 10.1107/S1600577519001607. [Online]. Available: https://doi.org/10.1107/S1600577519001607.

[110] D. Khakhulin *et al.*, "Ultrafast x-ray photochemistry at european xfel: Capabilities of the femtosecond x-ray experiments (fxe) instrument," *Applied Sciences*, vol. 10, no. 3, p. 995, Feb. 2020, ISSN: 2076-3417. DOI: 10.3390/app10030995. [Online]. Available: http://dx.doi.org/10.3390/app10030995.

[111] P. Pillet *et al.*, "Controllable interactions between Rydberg atoms and ultracold plasmas," *J. Phys. Conf. Ser.*, vol. 194, no. 1, p. 012 066, Nov. 2009. DOI: 10.1088/1742-6596/194/1/012066. [Online]. Available: https://doi.org/10.1088%5C%2F1742-6596%5C%2F194%5C%2F1%5C%2F012066.

[112] J. Cabral *et al.*, "Effects of electric fields on ultracold Rydberg atom interactions," *J. Phys. B*, vol. 44, no. 18, p. 184 007, 2011.

[113] T. Pohl, H. R. Sadeghpour, and P. Schmelcher, "Cold and ultracold Rydberg atoms in strong magnetic fields," *Phys. Rep.*, vol. 484, no. 6, pp. 181–229, 2009.

[114] D. Tong *et al.*, "Local blockade of Rydberg excitation in an ultracold gas," *Phys. Rev. Lett.*, vol. 93, p. 063 001, 6 Aug. 2004. DOI: 10.1103/PhysRevLett.93.063001. [Online]. Available: https://link.aps.org/doi/10.1103/PhysRevLett.93.063001.

[115] E. Urban *et al.*, "Observation of Rydberg blockade between two atoms," *Nat. Phys.*, vol. 5, no. 2, p. 110, 2009.

[116] M. P. Robinson, B. L. Tolra, M. W. Noel, T. F. Gallagher, and P. Pillet, "Spontaneous evolution of Rydberg atoms into an ultracold plasma," *Phys. Rev. Lett.*, vol. 85, pp. 4466–4469, 21 Nov. 2000. DOI: 10.1103/PhysRevLett.85.4466. [Online]. Available: https://link.aps.org/doi/10.1103/PhysRevLett.85.4466.

[117] T. F. Gallagher, P. Pillet, M. P. Robinson, B. Laburthe-Tolra, and M. W. Noel, "Back and forth between Rydberg atoms and ultracold plasmas," *J. Opt. Soc. Am. B*, vol. 20, no. 5, pp. 1091–1097, May 2003. DOI: 10.1364/JOSAB.20.001091. [Online]. Available: http://josab.osa.org/abstract.cfm?URI=josab-20-5-1091.

[118] M. Mizoguchi *et al.*, "Ultrafast creation of overlapping Rydberg electrons in an atomic BEC and Mott-Insulator lattice," *Phys. Rev. Lett.*, vol. 124, p. 253 201, 25 Jun. 2020. DOI: 10.1103/PhysRevLett.124.253201. [Online]. Available: https://link.aps.org/doi/10.1103/PhysRevLett.124.253201.

[119] R. E. Olson, "Ionization cross sections for Rydberg-atom-Rydberg-atom collisions," *Phys. Rev. Lett.*, vol. 43, pp. 126–129, 2 Jul. 1979. DOI: 10.1103/PhysRevLett.43.126. [Online]. Available: https://link.aps.org/doi/10.1103/PhysRevLett.43.126.

[120] D. Richards, "On the production of Rydberg atoms with large orbital angular momentum," *J. Phys. B*, vol. 17, no. 7, p. 1221, 1984.

[121] P. M. Koch and D. R. Mariani, "Double-resonance Stark spectroscopy as a probe of hydrogen substate production in fast atomic collisions," *J. Phys. B*, vol. 13, no. 22, pp. L645–L650, Nov. 1980. DOI: 10.1088/0022-3700/13/22/001. [Online]. Available: https://doi.org/10.1088%5C%2F0022-3700%5C%2F13%5C%2F22%5C%2F001.

[122] R. G. Hulet and D. Kleppner, "Rydberg atoms in "circular" states," *Phys. Rev. Lett.*, vol. 51, pp. 1430–1433, 16 Oct. 1983. DOI: 10.1103/PhysRevLett.51.1430. [Online]. Available: https://link.aps.org/doi/10.1103/PhysRevLett.51.1430.

[123] R. Brecha, G. Raithel, C. Wagner, and H. Walther, "Circular Rydberg states with very large n," *Optics communications*, vol. 102, no. 3-4, pp. 257–264, 1993.

[124] D. Delande and J. C. Gay, "A new method for producing circular Rydberg states," *Europhysics Letters (EPL)*, vol. 5, no. 4, pp. 303–308, Feb. 1988. DOI: 10.1209/0295-5075/5/4/004. [Online]. Available: https://doi.org/10.1209%5C%2F0295-5075%5C%2F5%5C%2F4%5C%2F004.

[125] J. Hare, M. Gross, and P. Goy, "Circular atoms prepared by a new method of crossed electric and magnetic fields," *Phys. Rev. Lett.*, vol. 61, pp. 1938–1941, 17 Oct. 1988. DOI: 10.1103/PhysRevLett.61.1938. [Online]. Available: https://link.aps.org/doi/10.1103/PhysRevLett.61.1938.

[126] S. Patsch, D. M. Reich, J.-M. Raimond, M. Brune, S. Gleyzes, and C. P. Koch, "Fast and accurate circularization of a Rydberg atom," *Phys. Rev. A*, vol. 97, p. 053 418, 5 May 2018. DOI: 10.1103/PhysRevA.97.053418. [Online]. Available: https://link.aps.org/doi/10.1103/PhysRevA.97.053418.

[127] R. Cardman and G. Raithel, "Circularizing Rydberg atoms with time-dependent optical traps," *Phys. Rev. A*, vol. 101, p. 013 434, 1 Jan. 2020. DOI: 10.1103/PhysRevA.101.013434. [Online]. Available: https://link.aps.org/doi/10.1103/PhysRevA.101.013434.

[128] I. Percival and D. Richards, "Classical adiabatic pertubation theory of atomic excitation," *Proc. Phys. Soc.*, vol. 92, no. 2, p. 311, 1967.

[129] R. Abrines and I. Percival, "Classical theory of charge transfer and ionization of hydrogen atoms by protons," *Proceedings of the Physical Society*, vol. 88, no. 4, p. 861, 1966.

[130] D. Efimov, K. Miculis, N. Bezuglov, and A. Ekers, "Strong enhancement of Penning ionization for asymmetric atom pairs in cold Rydberg gases: The Tom and Jerry effect," *J. Phys. B*, vol. 49, no. 12, p. 125 302, 2016.

[131] A. Mazalam, K. Michulis, I. Beterov, N. Bezuglov, A. Klyucharev, and A. Ekers, "The optimal pair of Rydberg alkali-metal atoms in the nonsymmetric Penning ionization processes," *Optics and Spectroscopy*, vol. 127, no. 3, pp. 375–384, 2019.

[132] H. Goldstein, C. P. Poole, and J. L. Safko, *Classical mechanics*. Pearson, 2011.

[133] F. Robicheaux, J. V. Hernández, T. Top çu, and L. D. Noordam, "Simulation of coherent interactions between Rydberg atoms," *Phys. Rev. A*, vol. 70, p. 042 703, 4 Oct. 2004. DOI: 10.1103/PhysRevA.70.042703. [Online]. Available: https://link.aps.org/doi/10.1103/PhysRevA.70.042703.

[134] E. Merzbacher, "Quantum mechanics john wiley & sons," *Inc., New York*, 1998.

[135] S. C. Anco, T. Meadows, and V. Pascuzzi, "Some new aspects of first integrals and symmetries for central force dynamics," *Journal of Mathematical Physics*, vol. 57, no. 6, p. 062 901, 2016. DOI: 10.1063/1.4952643. [Online]. Available: https://doi.org/10.1063/1.4952643.

[136] T. Ehrenreich, J. Day, S. Hansen, E. Horsdal-Pedersen, K. MacAdam, and K. Mogensen, "Electron capture from oriented elliptic Rydberg atoms," *J. Phys. B*, vol. 27, no. 14, p. L383, 1994. DOI: 10.1088/0953-4075/27/14/013. [Online]. Available: https://doi.org/10.1088%5C%2F0953-4075%5C%2F27%5C%2F14%5C%2F013.

[137] A. Venkatesh and F. Robicheaux, "Simulations for x-ray imaging of wave-packet dynamics," *Phys. Rev. A*, vol. 106, p. 033 125, 3 Sep. 2022. DOI: 10.1103/PhysRevA.106.033125. [Online]. Available: https://link.aps.org/doi/10.1103/PhysRevA.106.033125.

[138] A. Venkatesh and F. Robicheaux, "Effect of the orientation of rydberg atoms on their collisional ionization cross section," *Phys. Rev. A*, vol. 102, p. 032 819, 3 Sep. 2020. DOI: 10.1103/PhysRevA.102.032819. [Online]. Available: https://link.aps.org/doi/10.1103/PhysRevA.102.032819.

VITA

Akilesh Venkatesh

Education

Purdue University, Ph.D, physics (2017 - 2022)

National Institute of Technology Rourkela, Integrated M.Sc. Physics (2012 - 2017)

Publications

Venkatesh, Akilesh, and Francis Robicheaux. "Simulations for x-ray imaging of wave packet dynamics." Physical Review A 106.3 (2022): 033125.

Venkatesh, Akilesh, and Francis Robicheaux. "Interference in nonlinear Compton scattering using a Schrödinger-equation approach." Physical Review A 103.1 (2021): 013111.

Venkatesh, Akilesh, and Francis Robicheaux. "Effect of the orientation of Rydberg atoms on their collisional ionization cross section." Physical Review A 102.3 (2020): 032819.

Venkatesh, Akilesh, and Francis Robicheaux. "Simulation of nonlinear Compton scattering from bound electrons." Physical Review A 101.1 (2020): 013409.